Optimizing the encapsulation of SN-38 in PCL-b-PEG polymer nanoparticles for cancer therapy

By

Lisa K Silverman

B.Sc., Massachusetts Institute of Technology, 2004
M.Sc., Hebrew University Jerusalem Israel, 2018

A Dissertation Submitted in Partial Fulfillment of the
Requirements for the Degree of

DOCTOR OF PHILOSOPHY

in the Department of Chemistry

Supervisory Committee

Optimizing the encapsulation of SN-38 in PCL-b-PEG
polymer nanoparticles for cancer therapy

By

Lisa K Silverman

B.Sc., Massachusetts Institute of Technology, 2004
M.Sc., Hebrew University Jerusalem Israel, 2018

Supervisory Committee Members:

Prof. Jeremy Wulff (Department of Chemistry)
Thesis Committee Member

Prof. Mohsen Akbari (Department of Mechanical Engineering)
Thesis Committee Member

Prof. Katherine Elvira (Department of Chemistry)
Thesis Committee Member

Prof. Matthew G Moffitt (Department of Chemistry)
Supervisor

Abstract

Background: In this study, we address challenges encapsulating the anticancer agent, SN-38, in polymer nanoparticles (PNPs) for improved cancer treatment. SN-38 is particularly difficult to encapsulate due to its poor solubility in water and many solvents.

Methods: PNPs were synthesized using both bulk and microfluidic nanoprecipitation, and characterized for physico-chemical properties, release kinetics, and cytotoxicity and tumor penetration in 2D cell culture and tumor spheroids. Different formulations of PNPs, including different ratios of SN-38 and curcumin (CUR), and block co-polymers with different PEG terminal endgroups were compared to find the optimal formulation for encapsulating SN-38.

Results: By co-encapsulating CUR with SN-38, we can achieve increased SN-38 encapsulation efficiencies in co-loaded SN-38/CUR-PNPs by up to ten-fold as compared to PNPs encapsulating SN-38 alone. Moreover, a two-phase microfluidic reactor demonstrates similar trends regarding SN-38 content with CUR co-encapsulation, compared to bulk nanoprecipitation methods. Our findings also reveal a decrease in PNP polydispersity from 0.34 to 0.07 as the initial CUR-to-polymer initial ratio increases from 0 to 10.

Our first cytotoxicity studies show adding CUR does not significantly affect SN-38 potency. However, we observed significant differences in the potencies of SN-38/CUR-PNP formulations depending on formulation. An optimized formulation exhibited sub-nanomolar cytotoxicity against A204 cells, surpassing the potency of free SN-38 or PNPs containing only SN-38.

We find that incorporating a thiol terminal end group onto the PEG in the PNP resulted in a doubling of SN-38 encapsulation efficiency from 10% in the reference SN-38/CUR-PNP-OCH_3 to 21% in SN-38/CUR-PNP-SH, but that this increase is only seen when the SN-38/CUR drug mixture is used, and not when the drugs are encapsulated individually.

Confocal microscopy shows encouraging results regarding PNP penetration throughout tumor spheroids, but EC_{50} cytotoxicity results in both 2D and 3D culture models show limited efficacy in cell killing of our formulations in 3D models, and although the SH-PNP formulation shows the best results in 2D models, the reference OCH_3 formulation shows better performance in the 3D models.

Conclusions: Our study presents a co-encapsulation strategy that significantly enhances SN-38 encapsulation efficiency within PNPs for improved cancer treatment strategies. These findings contribute to overcoming challenges associated with poor solubility of SN-38 and paves the way for the use of SN-38 in the clinic.

Table of Contents

List of Tables

List of Figures

Table of Acronyms

Name	Acronym
coronavirus disease of 2019	COVID-19
deoxyribose nucleic acid	DNA
ribose nucleic acid	RNA
polyethylene glycol	PEG
poly(ε-caprolactone)	PCL
single-phase staggered herringbone SHB	SHB
polycaprolactone-block-poly(ethylene oxide)	PCL-b-PEO
7-ethyl-10-hydroxycamptothecin	SN-38
curcumin	CUR
US Food and Drug Administration	FDA
Efficacy Coefficient	EC_{50}
two dimensional	2D
in-vitro in-vivo correlation	IVIVC
three dimensional	3D
polymer nanoparticles	PNP
dynamic light scattering	DLS
high performance liquid chromatography	HPLC
transmission electron microscopy	TEM
the 3-(4,5-dimethylthiazol-2-yl)-2,5-diphenyltetrazolium bromide	MTT
nicotinamide adenine dinucleotide phosphate hydrogen	NADPH
nicotinamide adenine dinucleotide (NAD) + hydrogen (H)	NADH
Irinotecan	CPT-11
camptothecin	CPT
antibody-drug conjugates	ADC
enhanced permeability and retention	EPR
N,*N*-dimethylformamide	DMF
poly(γ-benzyl-ε- caprolactone)-*b*-poly(ethylene glycol)	PBCL-*b*-PEG
phosphate-buffered saline	PBS
poly-(dimethylsiloxane)	PDMS
Argon	Ar
critical water content	cwc
kilodalton	kDa
molecular weight cut off	MWCO
weight %	wt %
hours	h
diode array detector	DAD
Encapsulation efficiency	EE
drug loading	DL
Dulbecco's modified Eagle's medium	DMEM
fetal bovine serum	FBS
degrees of freedom	DOF
polydispersity index	PDI

flow rate	Q
dispersion efficiencies	DE
reticuloendothelial system	RES
1,2-distearoyl-sn-glycero-3-phosphoethanolamine-polyethylene glycol	DSPE-PEG
polyethyleneimine	PEI
poly(lactic-co-glycolic acid)	PLGA
sequence arginine-glycine-asparagine	RGD
self-filling microwell arrays	SFMA
glioblastoma multiforme	GBM
hepatocellular carcinoma	HCC

Dedication

This thesis was written and completed in the days following October 7, 2023. It is dedicated to the victims of the atrocities committed on that day in Israel, and to the soldiers who fell that day and continue to fall in the efforts to prevent such a tragedy from ever occurring again.

Acknowledgments

I would like to acknowledge with great thanks all the many people who helped make this dissertation a reality. All of my committee members for their help and advice, as well as my colleagues in lab, who kept my spirits up and helped out with various experiments. I'd like to thank the undergraduates who worked with me over the years, completing many experiments late into the evening. Additionally, I'd like to thank Carter Castor for his invaluable help with curve fitting and data analysis, seen in Chapter 4.

A special thanks to my family, without whom I could not have accomplished any of this. Mom and Dad for all the different kinds of support you provided over the years, and a special thank you to Mom for help with formatting.

Most importantly, I'd like to thank my wife, Kestrel, who not only supported, protected, and advised me throughout the years of this process, but also safeguarded my sanity when I was unable to take care of it myself.

Thank you all.

1. Chapter 1: Introduction

1.1 Background and Motivation

Medications have been used for thousands of years without encapsulating the drugs. Encapsulating drugs is a time, resource, and energy intensive process, and is not suitable for all drugs, many of which work perfectly well without encapsulation. However, there are four primary situations in which encapsulation of a drug may be appropriate.

The first is to protect a patient from the drug being administered. A primary example of this is chemotherapy. The chemotherapeutic agents used to fight cancer are highly toxic, and when administered systemically, make the patient extremely sick. By encapsulating the drug, and especially by targeting the encapsulated drug, the therapeutic dose can be lowered and the patient can be exposed to less drug, leading to fewer side effects and safety issues.

The second situation is to protect the drug from the patient. The best recent example of this is the COVID-19 vaccines by BioNTech/Pfizer and Moderna but would apply to any DNA or RNA based medication. Genetic material cannot be injected "naked" into the body. If it were, it would be destroyed within minutes, as our immune systems have evolved for millennia to protect us from foreign genetic material from pathogenic organisms. Only by protecting the genetic material in some sort of vector or capsule can it be protected long enough to reach our cells and achieve therapeutic efficacy.

The third situation is that a drug has physical properties that are unsuitable for clinical use. The drug could be hydrophobic, not soluble in aqueous solutions such as blood, or inactive at physiological pH. If the bloodstream is not a suitable environment for a drug, encapsulation can take a drug unfit for clinical use and make it a viable option for patients.

The fourth reason is to change the pharmacokinetics, pharmacodynamics, or biodistribution of the drug. Nanoparticle encapsulation offers potential improvements in pharmacokinetics, pharmacodynamics, and biodistribution, but these attributes are mediated by a number of factors. Nanoparticle composition and physicochemical properties play a crucial role in determining their interactions with biological systems.[1] Factors such as size, shape, surface charge, surface chemistry (e.g., PEGylation, ligand conjugation), and composition affect pharmacokinetics, biodistribution, intratumoral penetration, and tumor bioavailability.[2] Additionally, tumor biology and patient characteristics also impact drug delivery by nanoparticles.[3]

Encapsulation of drugs in nanoparticles enhances their ability to enter cells and release their cargo intracellularly,[4] thus influencing the pharmacodynamics of the encapsulated drug. This improves drug stability, solubility, transport across membranes, and circulation times, leading to a reduction in dose and drug frequencies for patients, and decreasing toxic side effects.[3] However, challenges remain in increasing drug loading capacity, stability, and control of drug release profiles.

The biodistribution of drugs encapsulated in nanoparticles is influenced by their physicochemical properties, such as size, surface charge, and morphology.[3] Functionalizing nanoparticles with specific ligands can actively drive drugs to site-specific locations in active targeting, efficiently reaching therapeutic intracellular levels.[5] Moreover, nanoparticles offer versatility in controlling drug release profiles, which can be tuned for immediate or sustained delivery of drugs in a localized area.[6,7]

Nanoparticles offer several advantages in drug delivery, including improved stability and solubility of encapsulated cargos,[8,9] transport across membranes,[9] prolonged circulation times,[10] and increased safety and efficacy.[7] They can also be utilized for more complex systems, such as

nanocarrier-mediated combination therapies,[11–13], to target specific phases of the cell cycle,[14–16] or overcome mechanisms of drug resistance.[17–20]

Encapsulation of drugs can be a particularly good option for chemotherapy drugs. Chemotherapy drugs are highly toxic and cause severe side effects.[21] The side effects are dose dependent[22] so if it was possible to lower the therapeutic threshold of a cancer drug, the side effects to the patient could be reduced. Encapsulation in a nanoparticle can be a way to achieve this. Using either active or passive targeting, chemotherapy drugs in nanoparticles can reach the tumor more efficiently, decreasing the overall dose needed to achieve a therapeutic effect.[3] This can be a huge boon to patients suffering the side effects of chemotherapeutic drugs.

Despite the potential benefits of nanoparticle-based drug delivery systems, there are several challenges and drawbacks that must be addressed. These include issues related to overcoming biological barriers,[23] design and optimization of nanoparticles for specific applications,[24] scale-up and manufacturing of nanoparticles,[25] and nanoparticle safety profiles.[26] Continued research and development in this field will be essential to address these challenges and unlock the full potential of nanomedicine.

1.2 Polymers, block copolymers, and self assembly

A polymer is a large molecule composed of repeating subunits called monomers. Polymers are characterized by their high molecular weight and long chain-like structure . The chains of polymers can be linear, branched, or cross-linked, and they can be made up of a variety of different monomers. The interactions between the polymer chains, such as van der Waals forces and covalent bonds, contribute to the unique properties of polymers. Polymers can be found in various forms, including plastics, rubber, fibers, and coatings, and they have a wide range of applications

in industries including healthcare and drug delivery. The synthesis, characterization, and properties of polymers are extensively studied in the field of polymer science and engineering, which aims to understand and manipulate the structure and behavior of polymers for specific applications.[27]

Block copolymers are a specific type of copolymer composed of two or more chemically distinct polymer blocks connected together. These blocks can have different properties, such as different solubilities or chain conformations, which result in unique self-assembly behavior and morphologies. The self-assembly of block copolymers is driven by the segregation of the different blocks into distinct regions, leading to the formation of various nanostructures. The morphology of block copolymers can range from spherical micelles to cylindrical or lamellar structures, depending on the composition and molecular weight of the blocks.[28] The ability to control the self-assembly of block copolymers has attracted significant attention in materials science and nanotechnology due to their potential applications in areas such as lithography, drug delivery, and nanofabrication.[29] The unique properties and self-assembly behavior of block copolymers make them versatile materials for the design and fabrication of complex nanostructures with precise control over size, shape, and functionality.[30] The study of block copolymers has contributed to a deeper understanding of polymer physics and has opened up new avenues for the development of advanced materials with tailored properties.[31]

The self-assembly of amphiphilic block copolymers is driven by thermodynamics. Thermodynamically, the self-assembly process is governed by the balance between the enthalpic and entropic contributions. The hydrophobic and hydrophilic blocks of the copolymer tend to segregate due to the unfavorable interactions between the hydrophobic segments and the surrounding solvent. This segregation leads to the formation of distinct domains or aggregates, such as micelles, vesicles, or lamellar structures. The thermodynamic driving force for self-

assembly is the reduction of the system's free energy by minimizing the unfavorable interactions and maximizing the favorable interactions between the polymer blocks and the solvent.[32]

Kinetics also play a crucial role in the self-assembly process of block copolymers. The kinetics determine the rate at which the copolymer chains organize themselves into the desired structures. The kinetics depends on factors such as the concentration of the copolymer, temperature, solvent quality, and the presence of additives. The kinetics can influence the final morphology and size of the self-assembled structures, as well as the stability of the aggregates.[32]

The thermodynamics and kinetics of block copolymer self-assembly are influenced by various factors. The composition and molecular weight of the copolymer blocks, as well as the solvent conditions, can affect the thermodynamic stability and the range of accessible morphologies.[32]

The block ratio between the hydrophilic and hydrophobic blocks can determine the type of self-assembled aggregates formed.[33] Additionally, the presence of crystalline regions within the copolymer blocks can further influence the self-assembly behavior.[33] The kinetics of self-assembly can be controlled by adjusting parameters such as temperature, concentration, and the addition of external stimuli.[32]

Understanding the thermodynamics and kinetics of block copolymer self-assembly is crucial for the design and fabrication of functional materials with tailored properties. By manipulating the composition, molecular weight, and solvent conditions, it is possible to achieve precise control over the morphology and size of the self-assembled structures. This control opens up opportunities for various applications, including drug delivery systems, nanofabrication, and materials with specific optical or mechanical properties.[32]

The specific polymer we use in these studies is polycaprolactone-block-poly(ethylene oxide) (PCL(12k)-b-PEO(5k)), see Figure 1. PCL-b-PEO is an amphiphilic block copolymer as discussed

above. PCL was chosen as the hydrophobic block because it is already FDA approved, biodegradable, biocompatible, and commercially available.[34] PEG was chosen as the hydrophilic block also because it is FDA approved, and also helps nanoparticles evade the immune system.[10] These properties of PEG will be discussed further in chapter 3.

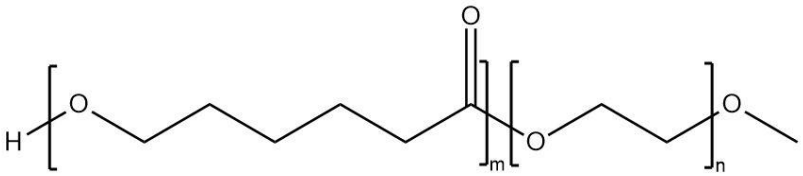

Figure 1: Molecular structure of PCL-b-PEG

1.3 Microfluidic nanoprecipiation for synthesis of polymer nanoparticles

Microfluidics is a field that focuses on the manipulation and control of fluids at the microscale level. It has emerged as a multidisciplinary field that combines principles from physics, chemistry, engineering, and biology to study the behavior of fluids in microchannels and develop devices for precise fluid handling.[35]

The background of microfluidics can be traced back to the development of microfabrication techniques in the 1980s, which enabled the fabrication of microscale structures and channels. This breakthrough allowed researchers to explore the unique properties and phenomena that occur at the microscale, such as laminar flow, surface tension, and capillary action.[35]

The theory of microfluidics is based on the principles of fluid mechanics, which describe the behavior of fluids under different flow conditions. At the microscale, the dominant flow regime is laminar flow, where the fluid flows in parallel layers without significant mixing. This is due to the low Reynolds number, which is a dimensionless parameter that characterizes the ratio of inertial

forces to viscous forces in a fluid flow. The low Reynolds number in microfluidic systems allows for precise control and manipulation of fluids, as well as efficient heat and mass transfer.[35]

Microfluidic devices are typically fabricated using techniques such as photolithography, soft lithography, or 3D printing. These devices consist of microchannels, chambers, valves, and pumps that enable the precise control of fluid flow, mixing, and separation. The behavior of fluids in microchannels is influenced by various factors such as channel geometry, surface properties, and flow rates. Understanding these factors is crucial for designing and optimizing microfluidic devices.[35]

There are different methods of microfluidic nanoparticle synthesis. One common approach is the droplet microfluidics method, which involves the generation and manipulation of droplets containing the precursor materials for nanoparticle synthesis.[36] This method allows for the precise control of droplet size and composition, leading to the production of nanoparticles with uniform size and properties.[37] The droplets can be further processed to form solid nanoparticles through techniques such as nanoprecipitation[38] or by using reducing agents to induce the formation of nanoparticles within the droplets.[39]

Another method is the flow focusing technique, which involves the controlled mixing of two or more streams of fluids to induce nanoparticle formation.[40] This technique allows for the precise control of the mixing process, leading to the production of nanoparticles with desired properties.[41] Additionally, the use of microreactors in microfluidic systems has been explored for the synthesis of nanoparticles, offering improved control, reproducibility, and automation compared to conventional batch synthesis methods.[42] This flow focusing technique using a microfluidic reactor is the method of microfluidic synthesis used in this study.

The microfluidic device used in the studies throughout this dissertation is a two-phase microreactor. Previous research in our lab compared singe and two-phase microfluidic reactors. The flow control and multiscale structure of polymeric nanoparticles synthesized using two different microfluidic reactors was compared: the single-phase staggered herringbone (SHB) mixer and the two-phase gas-liquid segmented mixer.[43] The study focused on the manufacturing of polycaprolactone-block-poly(ethylene oxide) (PCL-b-PEO) nanoparticles, which is the same copolymer used in the studies in this dissertation.

Microfluidics has emerged as a promising tool for the development and optimization of polymeric nanoparticles, particularly in the field of nanomedicine.[44] The microfluidic technique offers advantages such as enhanced mixing, precise fluidic modulation, and the ability to control the flow-mediated production of nanoparticles.[45] It enables the synthesis of nanoparticles with improved controllability and reproducibility compared to bulk synthesis methods.[46]

It also provides a platform for the controlled manufacturing of hierarchical polymeric nanoparticles, allowing for the simultaneous control of multiple levels of organization through a single control variable.[47]

The comparison between the SHB mixer and the two-phase segmented mixer in the synthesis of PCL-b-PEO nanoparticles reveals differences in flow control and multiscale structure. The SHB mixer, with its single-phase flow, offers enhanced mixing and precise control over the flow field, resulting in the formation of nanoparticles with a more uniform size distribution and improved monodispersity. On the other hand, the two-phase segmented mixer allows for the formation of nanoparticles with a higher encapsulation efficiency and a narrower size distribution.[43] It is for these reasons that we proceeded with a two phase microfluidic reactor for our nanoparticles.

One very common commercially available microfluidic nanoparticle synthesis system is the NanoAssmblr®, by Precision Nanosystems. The Precision Nanosystems NanoAssemblr microfluidic nanoparticle synthesis system is an automated mixing platform used for the high-throughput manufacturing of nanoparticles.[48] It is a microfluidics-based system that enables the precise control of mixing and fluidic modulation inside microchannels, allowing for the flow-mediated production of nanoparticles in a controllable manner.[45] The NanoAssemblr is a single phase herringbone system, which shows significant promise, but has the kinds of advantages and disadvantages in comparison to our system described above.

1.4 SN-38

7-ethyl-10-hydroxycamptothecin (SN-38) is the active form of the prodrug irinotecan.[49] Irinotecan is indicated for the clinical treatment of gastrointestinal cancers, specifically colorectal cancer and pancreatic cancer.[50–52] Irinotecan is converted to SN-38 in the body at a rate of about 2-8%.[49] SN-38 has been shown in-vitro to be 10-1000x more potent than irinotecan as an anticancer agent,[53,54] but it is not well suited for clinical use because of its hydrophobicity and inactivity above pH 6.[53,54] This makes SN-38 an excellent candidate for encapsulation in a nanoparticle for clinical use, and there are efforts to encapsulate SN-38 in a polymer nanoparticle for cancer therapy.[55–57] However, nanoparticle encapsulation has also proven difficult, due to a variety of factors.[58]

1.5 Curcumin

Curcumin (CUR) is a natural product from the turmeric plant, which has been touted for its many health benefits, particularly as an anti-inflammatory agent.[59] As a derivative of a food product, it is generally safe and well tolerated.[60] Research in our own lab has shown that when used in block co-polymer nanoparticles, it can act as a plasticizer, decreasing the crystallinity of the

nanoparticles, and allowing for higher drug loading.[61] CUR also contains carbonyl groups, allowing for the possibility of acting as a hydrogen acceptor for hydrogen bonding with SN-38, which may allow the SN-38 to become slightly less hydrophobic and remain dispersed in solution slightly longer.[62]

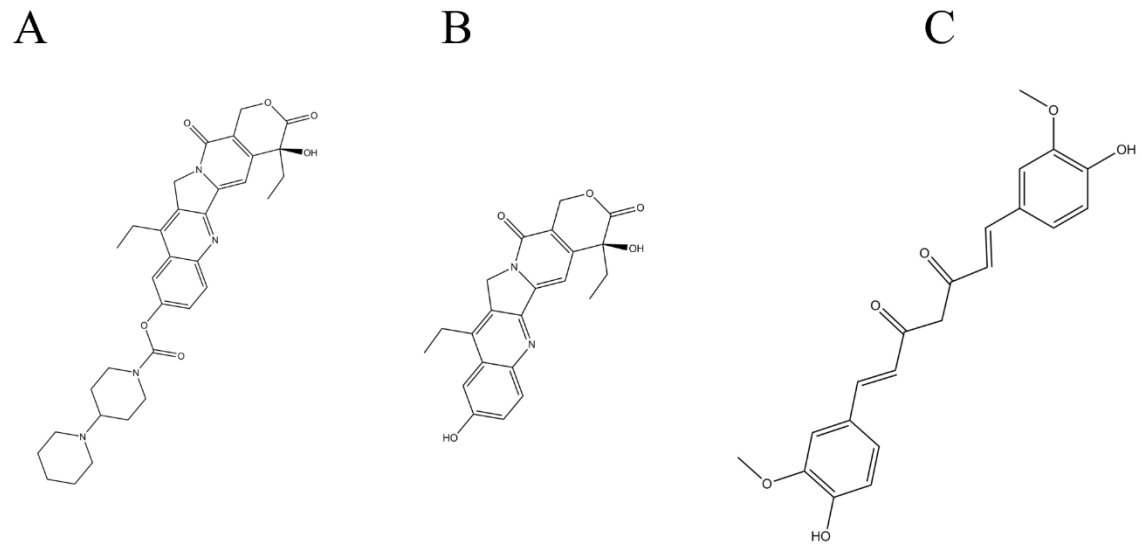

Figure 2: Molecular structure of (A) irintotecan (B) SN-38 (C) curcumin

1.6 Combination Therapy

Co-encapsulation of two compounds can improve the loading efficiencies of one or both compounds.[62] In addition to our own research showing this, other groups have combined doxorubicin and resveratrol and found that loading efficiencies of doxorubicin increased.[63] In another study, quercetin and doxorubicin co-encapsulation increased the loading efficiencies of both drugs. [64] This is different from syngergistic combination therapy, pioneered by Chao and Talalay, who developed a method for quantifying the degree of synergy between two drugs in combination therapy.[65] In this concept, both compounds have therapeutic effects against the disease being targeted, and work better together than either does separately, or than the additive effect of simply using two drugs.[66] It should be emphasized that in this study, curcumin is treated

as more of an excipient than a drug substance in the nanoparticle. It acts as a plasticizer for the nanoparticle and potential hydrogen bond acceptor for SN-38, making it a crucial part of the formulation for encapsulating SN-38, but it does not appreciably affect cancer levels by itself.[62]

1.7 Release Kinetics

Release kinetics are an important aspect of nanoparticle formulations, and can be affected by many of the physico-chemical characteristics of nanoparticles.[67,68] Release kinetics are also a characterization requirement for nanoparticle formulations submitted for the US Food and Drug Administration (FDA) approval.[25] Work in our own lab has shown the effect of different release conditions on release kinetics, and the effects of different flow rates in microfluidic nano-prepitation of polymer nanoparticles on release kinetics.[69] Proper release kinetics for a nanoparticle formulation are critical to nanoparticle efficacy in vivo. Because it takes time for a systemically administered nanoparticle to arrive at the intended destination, burst release, or release that is too fast, will negate the advantages of using nanoparticles for drug delivery. By the time the nanoparticle reaches the tissue of interest, there will be no drug in the nanoparticle to delivery, and the free drug in the bloodstream will have all the adverse effects that drug always has when administered as free drug. On the other hand, release that is too slow lowers efficacy because drug is not released at the target. This can be illustrated in the case of Stealth™ cisplatin, which failed in clinical trials due to a lack of efficacy caused by a lack of release of the cisplatin from the particle.[70,71] However, release kinetics can be challenging to tune for a given nanoparticle formulation.[72]

In the case of release from polymer nanoparticles that is too fast, one method for slowing down the release is crosslinking. Work in the Wooley lab pioneered this particular method, showing that

crosslinking of polymers can change not only release kinetics, but cytotoxicity and other characteristics of the nanoparticle.[73–76]

1.8 Three Dimensional Cell Culture Models

Cell viability studies of cells subjected to exposure to drugs or other toxic compounds, or Efficacy Coefficient (EC_{50}) studies are the traditional gold standard for in-vitro testing of the potency of new drugs.[77–79] However, while two dimensional (2D) cell culture still holds an important place in the workflow of drug discovery and testing potential new drugs and formulations, it has many drawbacks. Our body is not 2D and is not composed of one single kind of cell. Not even individual organs or tissues are two-dimensional or contain only one single kind of cell. Furthermore, when drugs are administered to patients, drugs are not evenly applied across a tissue with equal access of the drug to all cells. It is partially because of these inconsistencies with reality that in-vitro in-vivo correlation (IVIVC) is such a difficult concept to achieve.[80]

Complex "organs-on-a-chip" provide elements such as tumor microenvironments, mixed cell types, and microfluidics to provide pressure and flow elements to mimic living tissue.[81,82] However, even more basic three dimensional (3D) cell models provide important information about cell penetration in tumors and highlight the increased drug dosages required to be effective against 3D cell structures rather than 2D monolayers.[77,83] This can help prepare for future in-vivo work in small model organisms or even humans.[84]

1.9 Methods

1.9.1 Particle Synthesis

There are many ways of creating micelles or nanoparticles from block copolymers.[85] These methods include solvent-evaporation,[86] emulsion,[87] and nanoprecipitation.[43,62,69,88] Block

copolymers can spontaneously self-assemble in select solvents, and their morphology can be changed by adjusting the salt concentrations of these solvents.[89,90] Our lab synthesizes our nanoparticles using nanoprecipitation. This method is low energy, since it does not require high energy methods such as homogenization, is relatively simple, and results in particles typically below 300nm,[85] which is ideal for clinical nanomedicine.[91]

While nanoprecipitation has many advantages, there are also drawbacks to this method. One drawback is the difficulty in tuning physico-chemical properties of the nanoparticles resulting from nanoprecipitation.[92] However, nanoprecipitation can be further modified by the addition of microfluidics, allowing for tuning of phyisco-chemical characteristics of particles.[62,69,92–94] In traditional nanoprecipitation, tuning of particles has to be done "bottom up",[92] by changing the materials or concentration used for making the nanoparticles[95] or the properties of the solvents that the particles are made in.[89,90] In contrast to this, our microfluidic approach to tuning the properties of the nanoparticles is "top down", by using shear forces exerted on the particles during synthesis in the microfluidic chip.[92]

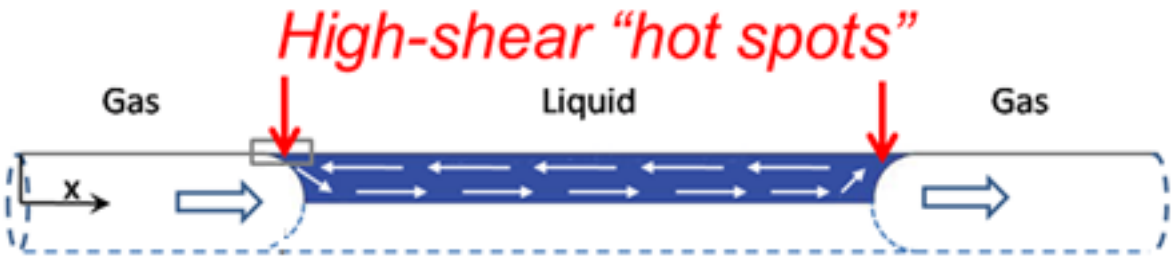

Figure 3. Schematic of the shear forces exerted by the microfluidic chip

Used with permission from Prof. Moffitt's presentations.

In our research, a two phase gas-liquid microfluidic reactor is used to produce shear forces on the particles after formation, causing coalescence or breakup of the particles. The strength of the shear forces on the polymer nanoparticles (PNPs) will change based on the flow rate of both the liquid and gas through the chip, and the strength of these shear forces will change the characteristics of the resulting particle.[94] The shear forces are created by vortices that are formed at the corner of the liquid-gas interface and the wall of the chip. It is at these "hot spots", that shear forces are highest, and which cause the changes in morphology and other characteristics of the PNPs.[96]

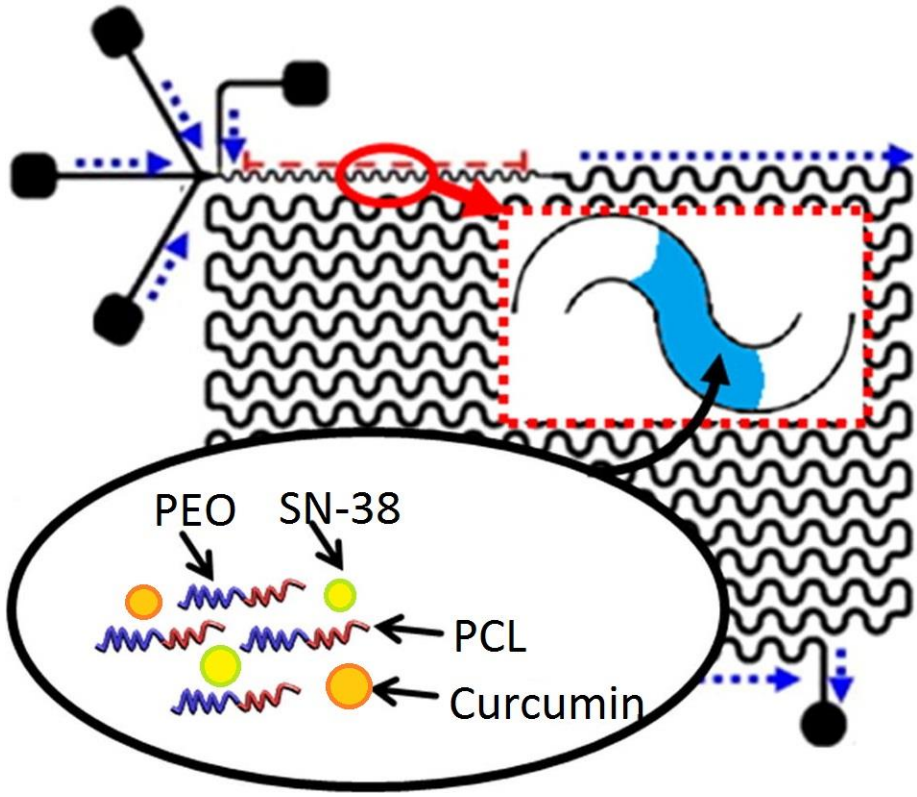

Figure 4. Schematic representation of the microfluidic chip.

Adapted with permission from Aman Bains, Matthew G. Moffitt, Effects of chemical and processing variables on paclitaxel-loaded polymer nanoparticles prepared using microfluidics,

Journal of Colloid and Interface Science,,Volume 508,2017,Pages 203-213,ISSN 0021-9797,

https://doi.org/10.1016/j.jcis.2017.08.053.

1.9.2 PNP characterization

Throughout this work, PNPs were characterized after synthesis, primarily by dynamic light scattering (DLS) for hydrodynamic diameter and polydispersity, and by high performance liquid chromatography (HPLC) for drug content. Transmission electron microscopy (TEM) was also used to visualize particles in 2D.

1.9.2.1 High Performance Liquid Chromatography

HPLC is an analytical technique for the separation, identification, and quantification of compounds that is widely used in various fields, including pharmaceuticals, environmental analysis, forensics, and clinical research. HPLC uses two 'phases' for analysis, a liquid mobile phase and a stationary phase. The stationary phase is generally packed in a column. By flowing the mobile phase, including the sample, across the stationary phase, analytes can be separated based on their interactions with the stationary phase.[97]

The basic principle of HPLC relies on the differential partitioning of analytes between the mobile phase and the stationary phase. The sample is injected into the HPLC system, and a pump delivers the mobile phase at high pressure, allowing it to flow through the column. The analytes in the sample interact with the components of the stationary phase. These interactions are based on factors such as polarity, size, charge, and affinity. Based on these interactions, different analytes travel through the column at different speeds and arrive at the detector at different times. This allows for the separation of analytes.[98]

Several parameters need to be optimized for efficient HPLC analysis, including the choice of stationary phase, mobile phase composition, flow rate, column temperature, and detection wavelength. These parameters are adjusted to achieve the desired separation, sensitivity, and

resolution.[97] In our case, this was particularly challenging, as we were analyzing two different compounds at the same time, SN-38 and also CUR. It was important that the peaks not overlap. HPLC instruments consist of various components, including pumps, injectors, columns, detectors, and data analysis software. Different types of detectors, such as UV-Vis, fluorescence, or mass spectrometry, can be used to detect and quantify the separated analytes based on their specific properties.[99] HPLC offers several advantages, including rapid analysis, high specificity, accuracy, precision, and ease of automation. It allows for the analysis of a wide range of compounds, from small molecules to large biomolecules, due to its versatility and compatibility with different detection methods.[97]

HJPLC is a widely used technique in pharmaceutical research due to its versatility and effectiveness in analyzing various compounds. HPLC has found applications in different areas of pharmaceutical research, including enantiopurity analysis, quantification of drug compounds in pharmaceutical formulations, stability indicating methods, and bioequivalence studies.[100–102]

1.9.2.2 Dynamic Light Scattering

Dynamic light scattering (DLS) is a powerful technique for the characterization of nanoparticles and colloidal systems. It is based on the analysis of the intensity fluctuations of scattered light caused by the Brownian motion of particles in solution.[103]

Due to the random thermal motion of the particles, the scattered light intensity, and therefore the speckle pattern, fluctuates over time. These fluctuations can be analyzed to extract information about the size, size distribution, and dynamics of the particles.[103] In addition to the size distribution, DLS can also provide information about the diffusion coefficient of the particles. The diffusion coefficient is related to the Brownian motion of the particles and can be obtained from the decay

rate of the autocorrelation function.[104] It is important to note that DLS assumes that the particles are in thermal equilibrium and that their motion is random. Deviations from these assumptions can affect the accuracy of the measurements. Therefore, careful consideration of the experimental conditions and sample preparation is necessary to ensure reliable results.[103] In particular, the solution must be sufficiently dilute that particles do not interact with each other, and move solely through Brownian motion.

Typically DLS experiments involve measuring the scattered light at one or more angles to obtain information about the size and dynamics of particles in a sample. The choice of detector angles depends on the specific application and the information of interest. Three commonly used detector angles in DLS are forward scattering, backscattering, and side scattering. For our studies, side scattering was of most interest, and the detector was used an angle of 90°.

Once the speckle pattern is obtained and the autocorrelation function is created, the analysis of that autocorrelation function involves fitting it to a suitable model. The cumulant expansion and the non-negative least squares method are commonly used models that take into account factors such as polydispersity, multiple scattering, and instrumental effects to accurately determine the particle size distribution.[105] In our study, cumulant and CONTIN analysis were used.

Another consideration when using DLS measurements is that they are generally, and specifically in our studies, intensity weighted. This means that large particles are given more weight in an average distribution than small particles. The presence of even a few large aggregates can significantly affect the DLS data of a sample.[106] One way to avoid this is to use number weighted averages instead of intensity weighted averages, but traditionally in the literature, unless otherwise noted, data is given as intensity weighted averages. In our studies, we for the most part did not have an issue with large aggregates, and so intensity weighted averages were used without issue.

1.9.2.3 Transmission Electron Microscopy

Transmission electron microscopy (TEM) is a powerful technique used to study the structure and properties of materials at the atomic scale. It involves passing a beam of electrons through a thin specimen, which interacts with the specimen and produces an image.[107] The resolution of TEM is much higher than that of light microscopy, allowing for the visualization of individual atoms.[108]

In TEM, a beam of electrons is generated by an electron gun and accelerated towards the specimen. The electrons pass through a series of electromagnetic lenses that focus the beam onto the specimen. As the electrons interact with the atoms in the specimen, they scatter and are deflected from their original path. The scattered electrons are then collected by a detector, which generates an image based on the intensity of the scattered electrons.[107]

One of the key advantages of TEM is its high spatial resolution, which allows for the visualization of atomic-scale details. This is achieved by using a high-energy electron beam with a short wavelength.[108] The resolution of TEM can reach sub-angstrom levels, enabling the observation of individual atoms and atomic defects.[109]

TEM can also be used to study the morphology and composition of materials. By adjusting the imaging conditions, researchers can obtain high-resolution images that reveal the surface topography and internal structure of the specimen. This is particularly useful for studying nanomaterials, where the size and shape of nanoparticles can greatly influence their properties.[110]

In the case of polymer nanoparticles, the material being examined is not very electron dense. This is a problem for TEM and requires an extra step in order to visualize the nanoparticles. To overcome this problem, we used negative staining for our TEM. Negative staining is a widely used technique in TEM that allows for the visualization of biological samples and macromolecules. It

involves the application of a heavy metal stain, such as uranyl acetate or phosphotungstic acid, to the sample, which creates a contrast between the sample and the background.[111] In our case, we used uranyl acetate for our negative staining. Negative staining is particularly useful for visualizing samples that are difficult to image using other techniques, such as viruses, exosomes, liposomes, and protein complexes.[112–114]

The process of negative staining begins with the preparation of the sample. The sample is typically applied to a carbon-coated grid, which acts as a support for the specimen. The excess liquid is then blotted away, leaving a thin layer of the sample on the grid. The grid is then exposed to the negative staining solution, which contains the heavy metal stain. The stain is absorbed by the sample, creating a contrast between the stained sample and the unstained background.[111]

Negative staining provides several advantages in TEM imaging. Firstly, it is a relatively quick and simple technique that can be performed with minimal sample preparation. It allows for the visualization of samples in their native state, without the need for extensive fixation or embedding procedures. Additionally, negative staining provides good contrast and resolution, allowing for the observation of fine structural details.[111]

1.9.3 Cell Assays

1.9.3.1 Effective Concentration Studies

Inhibitory concentration, or effective concentration, cytotoxicity cell studies are an important aspect of drug discovery and development. These studies involve evaluating the cytotoxic effects of various compounds on cells, typically using cell culture systems. The goal is to determine the concentration of a compound that inhibits cell growth or induces cell death, known as the effective concentration (EC). This information is crucial for assessing the potential toxicity of a compound

and determining its therapeutic index and allows for a comparison of the efficacy of different cytotoxic agents, or different formulations of a cytotoxic agent. Cell viability was traditionally measured using the 3-(4,5-dimethylthiazol-2-yl)-2,5-diphenyltetrazolium bromide (MTT) assay,[115] but currently there are a plethora of options for evaluating cell viability in culture. In these studies, two different commercially available formulas were used, Cell Titer Blue and Presto Blue. Both of these formulas use the same active reagent, reazurin.

Resazurin is a commonly used compound in cell viability studies. It is a redox indicator that reflects the metabolic activity and viability of cells. In living cells, resazurin is reduced to a highly fluorescent compound called resorufin, which can be quantified using various methods such as spectrophotometry or fluorescence measurements.[116]

The use of resazurin in cell viability studies has been compared to other cytotoxicity assays such as Alamar Blue, Neutral Red, and MTT assays.[117] These studies have shown that resazurin-based assays provide reliable and accurate results for assessing cellular proliferation, viability, and metabolic activity. The assay is sensitive and can detect changes in cell viability even at low concentrations of compounds.[117]

Resazurin-based assays have been used in various research areas, including cancer research, tissue engineering, and drug delivery. For example, researchers have used resazurin assays to evaluate the effects of natural compounds, plant extracts, and drugs on cell viability and apoptosis in cancer cells.[118,119] The assays have also been used to evaluate the cytotoxicity of nanoparticles and other materials, including extensively in our own lab.[62,88,120–122]

The mechanism of action of resazurin in cell viability studies involves its conversion to resorufin, a highly fluorescent compound, by living cells. In viable cells, resazurin is reduced by mitochondrial metabolic activity, resulting in the production of resorufin. The reduction of

resazurin to resorufin is mediated by nicotinamide adenine dinucleotide phosphate hydrogen (NADPH) or NADH, and the reaction can be quantified using various methods such as spectrophotometry or fluorescence measurements.[123]

The use of resazurin in cell viability studies has been applied in various research areas, including cancer research, tissue engineering, and drug delivery. It has been used to evaluate the effects of natural compounds, plant extracts, drugs, and nanoparticles on cell viability and apoptosis.[123]

Resazurin-based assays provide a reliable and sensitive method for assessing cell viability and metabolic activity. They have been widely used in various research areas and have contributed to our understanding of cellular processes and the effects of different compounds on cell viability. These assays are valuable tools in drug discovery, toxicology studies, and tissue engineering research.

1.9.4 Confocal Microscopy

Confocal microscopy is a powerful imaging technique that allows for the visualization of cellular structures with high resolution and contrast. It is a non-invasive method that uses a laser to scan a specimen and create detailed images at different depths.[124] The principle of confocal microscopy is based on the illumination of a small volume of the specimen and the elimination of out-of-focus light by the use of pinholes.[125] This technique has been widely used in various fields, including medicine, biology, and materials science.

In the field of biology, confocal microscopy has been used to study cellular structures and processes. It has been employed in the examination of nerve fibers, goblet cells, and epithelial cells.[124] Confocal microscopy has also been used to investigate bacterial adhesion and microbial viability in food research.[125] In addition, it has been utilized in the study of gold nanoparticles, metal nanoparticles, and schizosaccharomyces.[126] Confocal microscopy has been used to explore

the interactions between colloids and to measure colloidal interactions.[127] It has also been used in the study of cellular structures in the alveolar respiratory system.[128]

Confocal microscopy has also found applications in materials science. It has been used to study microtubules in drosophila larvae and to investigate the stability of carbon dioxide in pH-controlled bubble coalescence.[129,130] Confocal microscopy has been utilized in the characterization of oil droplets and the determination of absolute separations and forces in nanofilms.[131,132] It has also been used in the study of deformable drops and bubbles and the measurement of dynamic interactions between microbubbles.[133]

Confocal microscopy is a versatile imaging technique that has been widely used in various fields. It allows for the visualization of cellular structures with high resolution and contrast, making it a valuable tool for research and clinical applications. It is particularly useful for this research because the natural fluorescence of curcumin allows for the imaging on the PNPs in 2 and 3D cell cultures, without modifying the nanoparticles or adding any probes. Especially in 3D cell cultures, confocal microscopy allows a z-stack of images of all the depths of the tumor spheroid, removing the need for microtoming or slicing of the spheroids prior to imaging.

1.10 Conclusion

SN-38 is a powerful anticancer agent that has yet to reach its full potential because of difficulties using it in the clinic. By co-encapsulating SN-38 with curcumin in polymer nanoparticles, we can perhaps overcome some of these challenges and enable the use of SN-38 in the clinic. Experiments were carried out using both bulk and microfluidic nanoprecipitation of polymer nanoparticles, and the resulting nanoparticles were

characterized using a broad spectrum of techniques. Further chapters will discuss the findings of these experiments.

2. Chapter 2: Improvements in Drug-Delivery Properties by Co-Encapsulating Curcumin in SN-38-Loaded Anticancer Polymeric Nanoparticles

2.1 Contributions

In this peer reviewed article, Improvements in Drug-Delivery Properties by Co-Encapsulating Curcumin in SN-38-Loaded Anticancer Polymeric Nanoparticles, Lisa Silverman, Gitika Bhatti, Jeremy E. Wulff, and Matthew G. Moffitt, Molecular Pharmaceutics **2022** *19* (6), 1866-1881, DOI: 10.1021/acs.molpharmaceut.2c00005, with the assistance of undergraduate Gitika Bhatti, I performed all experiments. I performed all data analysis. TEM images were captured by Talide de Francesco of the Moffitt group. The writing of the article and the creation of the figures was done cooperatively by me and my advisor, Prof. Matt Moffitt. Prof. Jeremy Wulff provided guidance and troubleshooting on the cell assay section of the experimental work. This work was reproduced in its entirety here, including all figures, with permission from the publisher.

2.2 Introduction

Irinotecan (CPT-11) is a synthetic analog of camptothecin (CPT), which has been used as an anticancer drug in humans.[49] In the body, about 2-8% of administered CPT-11 is converted to the active compound SN-38.[49] While SN-38 is found to be 100-1000× more potent than CPT-11 in *in vitro* trials, its direct clinical use is limited due to its low water solubility, low bioavailability, and a ring-opening pathway above pH 6 that renders the molecule inactive.[53,54] In addition, the

moderate potency and low specificity of SN-38 leads to a narrow therapeutic index which introduces further challenges to its clinical application. Although antibody-drug conjugates (ADCs) have been explored for increasing the therapeutic index of SN-38, conventional applications of ADCs require ultracytotoxic drugs with subnanomolar potencies, compared to the nanomolar potencies determined for SN-38 in a range of cell lines.[134] Encapsulating SN-38 in the hydrophobic cores of polymer nanoparticles (PNPs), including polymeric micelles of block copolymers, is a promising route to improving its dispersability, bioavailability, stability, and therapeutic index for cancer therapy applications.[57] However, SN-38 is a challenging drug to encapsulate due to a combination of molecular properties,[135] including poor solubility in both lipids[136] and many polar organic solvents used for encapsulation,[137] along with a strong tendency to undergo crystallization.[138]

In order to overcome the challenges described above, a number of different encapsulation methods have been applied for producing SN-38-loaded PNPs. For example, several studies have demonstrated SN-38 encapsulation using the solvent emulsion method, in which SN-38 is dissolved in an emulsified organic solvent, followed by solvent removal to form PNP dispersions.[58,139–144] This method yields high drug encapsulation efficiencies, but is energy-intensive (requiring a high shear homogenizer) and tends to form relatively large PNPs (>200 nm) in the upper size limit of biological barriers for drug delivery, including those associated with the enhanced permeability and retention (EPR) effect.[145,146] Chemical synthetic strategies for SN-38 encapsulation, including the production of SN-38 prodrugs with improved solubilities in PNP cores,[147] or the conjugation of SN-38 to polymer carriers,[135,137,148–150] have also been employed. Additional methods for enhancing the encapsulation of SN-38 (and other hydrophobic drugs)

include the use of drug-binding ligands[56,151] and the formulation of excipient-free nanodispersions using two drugs.[152–154]

Compared to other encapsulation methods, nanoprecipitation offers relative simplicity, low energy input, and high reproducibility, and is therefore one of the most widely applied methods for the preparation of drug-loaded PNPs.[155] In addition, nanoprecipitation tends to form small, low polydispersity PNPs in a size regime (< 200 nm) well suited to drug delivery.[146,155] Moreover, the possibility of combining nanoprecipitation with microfluidic mixing introduces routes to additional experimental handles on PNP structure and properties via microfluidic reactor design and flow parameters.[44,47,69,92,94,156–165] In previous work from our group, we used the nanoprecipitation method to form SN-38-loaded PNPs within a two-phase, gas-liquid segmented microfluidic reactor by fast mixing of water with *N*,*N*-dimethylformamide (DMF) solutions containing drug and poly(methyl caprolactone-*co*-caprolactone)-*block*-poly(ethylene glycol).[47] By varying the microfluidic flow rate, we achieved shear processing control of PNP properties, including size, drug release rate, and cytotoxicity.[47] However, all of the investigated formulations yielded low SN-38 encapsulation efficiencies,[47] likely due to the deleterious molecular factors described above. Other groups have achieved enhancements in SN-38 encapsulation by nanoprecipitation using a combination of lower-polarity solvents (including tetrahydrofuran and chloroform),[141,166,167] elevated temperatures,[166] and specialty excipients including polymer blends[168] and amino acid-based copolymers[169]— strategies that require high energy input, significant changes in formulation chemistry, or use solvents that are not compatible with many microfluidic reactors. We were therefore motivated to find a simple and generally applicable approach for improving the nanoprecipitation method for SN-38 encapsulation using commercially available copolymers.

A demonstrated strategy for improving the encapsulation efficiencies of various drugs is the addition of compounds that become co-encapsulated with the principal drug. For example, co-encapsulation of doxorubicin and resveratrol was shown to increase doxorubicin encapsulation efficiencies in poly(ε-caprolactone)-*b*-poly(ethylene glycol) (PCL-*b*-PEG) and poly(γ-benzyl-ε-caprolactone)-*b*-poly(ethylene glycol) (PBCL-*b*-PEG) nanoparticles.[63] In another study, co-encapsulation of quercetin and doxorubicin increased encapsulation of both drugs relative to PNPs containing only one compound.[64] The co-encapsulation strategy has also been applied to PNP formulations containing cisplatin and paclitaxel, with overall drug contents increasing as the initial cisplatin amount was increased.[170]

CUR is a natural compound derived from turmeric that has been shown to have a number of potential therapeutic benefits, including anti-inflammatory properties[51] and a tendency to combat multi-drug resistance by cancer cells.[59,171–173] Co-encapsulation of CUR within PNP formulations has been shown to slow release kinetics and increase the anticancer activity of doxorubicin.[12,174] Moreover, CUR possesses hydroxyl groups available for hydrogen bonding with other molecules,[175] including SN-38, which can promote their dispersion in polar organic solvents and increase their encapsulation in PNP cores.[176–179] Given the large difference in cytotoxicities of SN-38 (nanomolar)[120] and CUR (micromolar),[88] the latter should act as an essentially inert excipient for cancer treatment, and yet one that has been FDA approved for human use.[180] For these reasons, the co-encapsulation of SN-38 with CUR appears to be a potential route to improving SN-38 encapsulation in addition to other potential therapeutic benefits.

In this study, we use the nanoprecipitation method to prepare SN-38/CUR-PNPs containing co-encapsulated SN-38 and CUR from the amphiphilic block copolymer PCL-*b*-PEG. Our approach involves co-dissolving the copolymer and the two drugs in DMF, then fast mixing with water above the critical water content, followed by dialysis to remove DMF (Figure 5). Variables in our formulations include the initial drug-to-polymer ratios (w/w) of SN-38 and CUR ($r_{SN\text{-}38}$ and r_{CUR}) and the mixing method, which includes both bulk mixing and flow-variable, microfluidic mixing in a two-phase, gas-liquid reactor. We show that CUR addition dramatically increases SN-38 encapsulation efficiencies (up to a factor of 10). Moreover, we demonstrate a surprising effect of CUR on the size dispersity of the resulting PNPs, with polydispersities dropping significantly as the initial CUR-to-polymer ratio is increased. Both SN-38 encapsulation and polydispersity trends are similar using bulk and microfluidic mixing methods, demonstrating the generality and accessibility of the strategy. Cytotoxicity studies of selected formulations on both U87 (glioblastoma) and A204 (rhabdomyosarcoma) cell lines reveal significant differences in the potencies of selected PNP formulations depending on $r_{SN\text{-}38}$ and r_{CUR} values, with the most potent SN-38/CUR-PNP formulation showing sub-nanomolar cytotoxicity against A204 cells—significantly more potent than either free SN-38 or SN-38-PNPs containing SN-38 alone. Co-encapsulation with CUR using nanoprecipitation appears to offer an efficient and accessible route for forming SN-38-loaded PNPs with improved properties for cancer treatment.

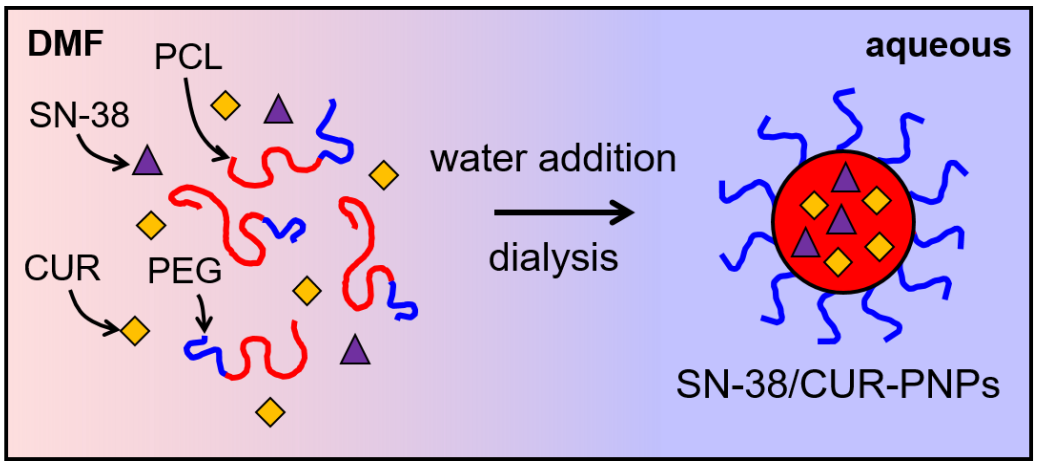

Figure 5. Schematic showing nanoprecipitation self-assembly route to forming PCL-b-PEG PNPs containing co-encapsulated CUR and SN-38. Reproduced with permission.

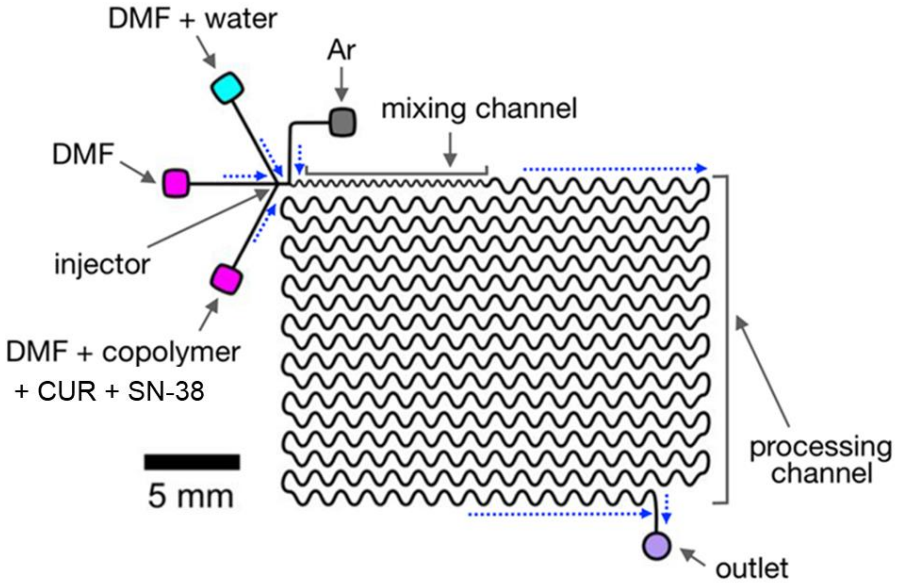

Figure 6. Schematic showing the two-phase gas– liquid microfluidic reactor used in this study. Reproduced with permission.

2.3 Methods

2.3.1 Experimental Materials.

The PCL-*b*-PEG block copolymer used in this study (Advanced Polymer Materials) possessed PCL and PEG blocks with number-average molecular weights of M_n = 12k g/mol and 5k g/mol, respectively, and overall dispersity of $Đ$ = 1.20. SN-38 (≥ 98.0 %) was purchased from Cedarlane

labs and CUR (for synthesis) was purchased from MilliporeSigma. NaCl (Bio Basic Canada, 99.9%), KCl (Caledon, 99.0%), Na_2HPO_4 (BioBasic Canada, 98.0%), and KH_2PO_4 (Caledon, 99.0%) were used to prepare phosphate-buffered saline (PBS, pH = 7.4). *N*,*N*-dimethylformamide (DMF, Caledon, 99.8%) and acetonitrile (Caledon, HPLC grade) were used as received.

2.3.2 Microfluidic Reactor Fabrication.

Negative masters were fabricated on silicon wafers (Silicon Materials) using the negative photoresist SU-8 100 (Kayaku). A 150 μm-thick SU-8 film was spin-coated at 2000 rpm onto the silicon wafer and heated at 65 °C for 12 min and then at 95 °C for 50 min. After the wafer was cooled, a photomask was placed directly above, and the wafer was exposed to UV light for 100 s. Then, the UV-treated film was heated at 65 °C for 1 min and then 95°C for 20 min. Finally, the silicon wafer was submerged in SU-8 developer (Kayaku) and rinsed with isopropanol until all unexposed photoresist was removed.

Microfluidic chips were fabricated from poly-(dimethylsiloxane) (PDMS) using a SYLGARD 184 silicon elastomer kit (Dow Corning). For fabrication of all PDMS chips, the elastomer and curing agent were mixed at a 7:1 ratio and degassed under vacuum. The resulting mixture was poured over a clean negative master chip in a Petri dish and further degassed until all remaining air bubbles were removed. The PDMS was heated at 85 °C until cured (∼20 min) and then peeled from the negative master; holes were punched through the reservoirs of the resulting PDMS chip to allow for the insertion of tubing. A thin PDMS film (substrate layer) was also made on a glass slide by spin-coating a 20:1 elastomer/curing agent mixture followed by curing. The substrate layer was then permanently bonded to the base of the microfluidic reactor (channel layer) after both

components were exposed to oxygen plasma for 90 s. The resulting reactor (Figure 6) has a set channel depth of 150 μm and consists of a sinusoidal mixing channel 100 μm wide and a sinusoidal processing channel 200 μm wide, identical to the reactor described in previous publications from our group.[88,93,94,120,121]

2.3.3 Flow Delivery and Control.

Pressure-driven flow of liquids to the reactor inlet was provided using 1 mL gastight syringes (Hamilton, Reno, NV) mounted on syringe pumps (Harvard Apparatus, Holliston, MA). The microfluidic chip was connected to the liquid syringes via 1/16th- inch (OD) Teflon tubing (Scientific Products and Equipment, ON). Argon (Ar) gas flow was introduced to the chip via an Ar tank regulator and a downstream regulator (Johnston Controls) for fine adjustments. The chip was connected to the downstream regulator through a 1/16th-inch (OD)/100-μm (ID) Teflon tube (Upchurch Scientific, Oak Harbor, WA). The liquid flow rate (Q_{liq}) was programmed via the syringe pumps, and the gas flow rate (Q_{gas}) was fine-tuned via the downstream pressure regulator in order to set the nominal total flow rates (Q) of 50, 100, 200, and 400 μL/min described in the main text. Due to the compressible nature of the gas and the high gas/liquid interfacial tension, discrepancies arise between the nominal (programmed) and actual values of Q_{gas}, Q_{gas}/Q_{liq}, and the total flow rate (Q_{total}). Therefore, actual values of Q_{gas}, Q_{gas}/Q_{liq}, and $Q_{total} = Q_{gas} + Q_{liq}$ for each microfluidic experiment (Appendix 1) were calculated from the frequency of bubble formation and the average volume of gas bubbles, determined from image analysis of the mean lengths of liquid and gas plugs, L_{liq} and L_{gas}, respectively, under a given set of flow conditions. With the exception of data in Figure 12, visualization and actual flow rate calculations were done using a modified version of Matlab software originally developed by Eugenia Kumacheva's lab at the University of Toronto and generously shared with our lab. For all experiments, $Q_{gas}/Q_{liq} \sim 1$; actual Q_{total} values are within

10% of nominal Q values reported in the main text, with the exception of experiments described in Figure 9. For Figure 12 experiments, visualization and actual flow rate calculations were done manually and actual Q_{total} values are within 22% of nominal Q values (with the majority of actual Q_{total} values being within 15% of nominal Q values). Images of the microchannels were captured using a Genie Nano-C1280 camera (1stVision) equipped with an On-Semi Python1300 sensor and a C-Mount Manual Iris Varifocal lens (1/1.8″, 4–13 mm, *f*/1.5) (Tamron).

2.3.4 Microfluidic Preparation of SN-38/CUR-Loaded Polymer Nanoparticles (SN-38/CUR-PNPs).

PNPs containing various quantities of SN-38 and CUR were prepared using a microfluidic nanoprecipitation method. For microfluidic preparation of SN-38/CUR-PNPs, the following three fluid streams were combined to form gas-segmented liquid plugs within the reactor (Figure 19): (1) 1.0 wt % PCL-*b*-PEG in DMF containing variable amounts of co-dissolved SN-38 and CUR, described by the initial drug-to-polymer ratios (w/w) $r_{SN\text{-}38}$ and r_{CUR}, respectively, with $r_{SN\text{-}38}$ varied between 0.1 to 0.75 and r_{CUR} varied between 0 to 10; (2) pure DMF; and (3) DMF/deionized water. The flow rates of the three liquid streams were equal for all runs such that the steady state on-chip copolymer concentration was 0.33 wt %. The water content of the DMF/water stream was selected to yield a steady state on-chip water concentration of 15.6 wt %. The critical water content (cwc) of 0.33 wt % PCL-*b*-PEG in DMF was determined to be 5.6 wt % (Appendix 1,Figure 41) such that the water content for all microfluidic SN-38/CUR-PNP preparations was cwc + 10 wt %. For each SN-38/CUR-PNP preparation, the sample was collected from the chip into vials containing 10× excess by volume of deionized water. In order to remove residual DMF, the resulting samples were then dialyzed (6−8 kilodalton (kDa) molecular weight cut off (MWCO) dialysis membrane,

Spectrum Laboratories) against deionized water for 18 h, with changing of water every hour for the first 4 h. Precipitated drug in the aqueous samples was removed by centrifugation at 16,000 × g for 10 min; the resulting dispersions were designated SN-38/CUR-PNPs.

2.3.5 Bulk Preparation of SN-38/CUR-Loaded Polymer Nanoparticles (SN-38/CUR-PNPs).

Selected PNP formulations were also prepared using a bulk nanoprecipitation approach. Specifically, ∼3 g quantities of 0.33 weight % (wt %) copolymer in DMF containing variable amounts of co-dissolved SN-38 and CUR, with $r_{SN\text{-}38}$ = 0.1 and r_{CUR} varied between 0 to 10, were prepared. The various solutions were stirred overnight, then each solution was added dropwise at a rate of 120 μL/min using a syringe pump into 10× excess volume of deionized water with continuous high- speed stirring. In order to remove residual DMF, the resulting samples were then dialyzed (6−8 kDa MWCO dialysis membrane, Spectrum Laboratories) against deionized water for 18 h, with changing of water every hour for the first 4 h. Precipitated drug in the aqueous samples was removed by centrifugation at 16,000 × g for 10 min; the resulting dispersions were designated SN-38/CUR-PNPs.

2.3.6 Nanoprecipitation of SN-38/CUR Blends without Copolymer.

Nanoprecipitation experiments similar to bulk PNP preparations but without copolymer were carried out to assess the effect of CUR on the dispersion of SN-38 within the solvent environment of PNP formation. For these experiments, varying concentrations of SN-38 and CUR were dissolved in DMF and vortexed until completely dissolved. Each solution was added dropwise at a rate of 120 μL/min using a syringe pump into 10× excess volume of deionized water with continuous high-speed stirring. The resulting samples were not dialyzed. Instead, they were

immediately centrifuged at 16,000 × g for 10 min to remove precipitated drug, then the supernatant was analyzed for SN-38 and CUR contents within 3 hours (h) of nanoprecipitation.

2.3.7 Transmission Electron Microscopy.

Negatively stained samples for TEM imaging were prepared by depositing a drop of SN-38/CUR-PNP sample on a Formvar/carbon-coated 300-mesh copper TEM grid followed by a drop of 1 wt % uranyl acetate aqueous solution as a negative staining agent. Excess liquid was removed after 30 seconds using filter paper, followed by drying of the remaining liquid under ambient conditions. Imaging was performed on a JEOL JEM1400 transmission electron microscope, operating at an accelerating voltage of 65 kV, and equipped with a Gatan Orius SC1000 CCD camera.

2.3.8 Dynamic Light Scattering.

DLS measurements were carried out for determination of hydrodynamic sizes and polydispersities of SN-38/CUR-PNPs. DLS experiments were performed on a Brookhaven Instruments photocorrelation spectrometer equipped with a BI-200SM goniometer, a BI-9000AT digital autocorrelator, and a BI-Mini-L30 30 mW red (636 nm) compact diode laser, at a scattering angle of 90° and a temperature of 23 °C. PNP concentrations for all DLS measurements were ∼0.03 mg/mL. To prepare samples for DLS measurements, ~0.5 mL aliquots of SN-38/CUR-PNPs were transferred to a clean scintillation vial containing ∼5 mL of deionized water that had been pre-filtered through 2 × 0.20 μm Nylon syringe filters (National Scientific) in series. The resulting dispersions were allowed to equilibrate for 15 minutes before a DLS measurement. For each PNP dispersion, mean effective hydrodynamic sizes and polydispersities were determined from three measurements of the autocorrelation function using cumulant analysis. Reported mean effective

hydrodynamic sizes and polydispersities for each condition were determined by averaging values from triplicate preparations. Standard errors (σ) on hydrodynamic sizes and polydispersities were calculated from the standard deviation (s) of triplicate values: $\sigma = \frac{s}{\sqrt{3}}$

2.3.9 Determination of SN-38 and Curcumin Encapsulation Efficiencies and Drug Loadings.

A high-performance liquid chromatograph (HPLC) (Agilent 1100) equipped with a Agilent Eclipse C18, 4.6 mm × 150 mm (5 µm) column and a diode array detector (DAD) set at 265 nm and 425 nm was used to quantify SN-38 and curcumin concentrations, respectively. The mobile phase consisting of acetonitrile and water (65:35, v/v) with 0.3 vol % acetic acid was run at 1 mL/min. The column temperature was kept at 25 °C during all measurements. To prepare samples for HPLC, water was removed from ~1 g of a gravimetrically determined quantity of SN-38/CUR-PNPs by rotary evaporation for 15 min at 25 °C, followed by addition of a known gravimetrically determined quantity of acetonitrile (~0.5 g) and overnight sonication to ensure complete dissolution of all solids. 10 µL of the drug/copolymer/acetonitrile solution was injected into the HPLC instrument by an autosampler for analysis of SN-38 and curcumin concentrations. An SN-38 calibration curve was generated using 5 standards of known concentrations of SN-38 in acetonitrile (1, 3, 5, 10, 25 ppm). A CUR calibration curve was generated using 8 standards of known concentrations of CUR in acetonitrile (1, 3, 5, 10, 25, 50, 100 and 200 ppm).

Encapsulation efficiencies (EE) and drug loadings (DL) of SN-38 and curcumin ($EE_{SN\text{-}38}$, EE_{CUR}, $DL_{SN\text{-}38}$, and DL_{CUR}) for each sample were calculated using the following equations:

$$\text{EE}\,(\%) = \frac{mass\ encapsulated\ drug}{total\ mass\ drug} \text{ x } 100$$

$$r = \frac{total\ mass\ drug}{total\ mass\ copolymer}$$

$$DL = \frac{mass\ encapsulated\ drug}{total\ mass\ copolymer}$$

$$DL = (EE/100)\ x\ r$$

Reported $EE_{SN\text{-}38}$, EE_{CUR}, $DL_{SN\text{-}38}$, and DL_{CUR} values were determined by averaging values from triplicate PNP preparations under the same conditions. Standard errors (σ) on encapsulation efficiencies and drug loadings were calculated from the standard deviation (s) of triplicate values: $\sigma = \frac{s}{\sqrt{3}}$

2.3.10 *In Vitro* Release Kinetics of SN-38/CUR-PNPs.

Near perfect sink conditions were established for *in vitro* release experiments, meaning that the volume of the PBS (pH = 7.4, ~4 L) release medium was sufficiently greater (~200×) than the sample volume (~20 mL) so as to approximate the large dilution of drug delivery particles in the human body. These sink conditions ensured that a large concentration gradient was maintained between the particles and the surrounding medium, driving continuous diffusion-controlled drug release. HPLC was used to monitor the SN-38 and CUR release kinetics of SN-38/CUR-PNPs. In a typical experiment, a known mass (~20 g) of SN-38/CUR-PNP sample was put into two 10 mL Float-A-Lyzer tubes (SpectrumLabs, MWCO 100 kDa). These tubes were then placed in a 5-L beaker of the release medium, consisting of ~4 L of PBS; throughout the release experiments, the release medium was constantly stirred using magnetic stirring and maintained at physiological temperature (37 ± 0.2 °C). Then, at each predetermined time (t = 0, 0.5, 1, 2, 4, 8, and 24 h), a gravimetrically determined aliquot (~2 g) of the larger sample was transferred from the Float-A-Lyzer tube to a vial and dried by rotary evaporation at 25 °C. A gravimetrically determined quantity

of acetonitrile (~1 g) was then added to the dried aliquot followed by overnight sonication to ensure complete dissolution of all solids. The concentrations of SN-38 and CUR were then determined by HPLC as described in the previous section; percentages of SN-38 and CUR released were calculated relative to the t = 0 h release time. Reported release percentages at each time point were determined by averaging values from triplicate PNP preparations under the same conditions. Standard errors ( ) on release percentages were calculated from the standard deviation (s) of triplicate values: $\sigma = \frac{s}{\sqrt{3}}$

The release profiles were fit using the Levenburg Marquardt algorithm within XLFit, an add-in for Microsoft Excel. Mean release half times were extrapolated from the fits using OriginLab; experimental errors on half time vales were determined based on the quality of the fits. The following fitting model was used for all conditions:

$$y = \left(\frac{1}{2B}\right)[(x + A + B - ((x + A + B)^2 - 4xB)^{0.5}]$$

2.3.11 Cell-Culture and Antiproliferation Assays.

U87 cells were grown to ~80% confluence in Dulbecco's Modified Eagle's Medium (DMEM) supplemented with 10% fetal bovine serum (FBS) and 1% penicillin/streptomycin in a 75 cm^2 tissue culture flask and maintained at 37 °C with 5% CO_2 in a tissue culture incubator. A204 cells were grown to ~80% confluence in McCoy's modified medium supplemented with 10% FBS and 1% penicillin/streptomycin in a 75 cm^2 tissue culture flask and maintained at 37 °C with 5% CO_2 in a tissue culture incubator. Cells were then trypsinized, collected, and pelleted by centrifugation at 4 °C and 1200 rpm for 5 min. The cell pellet was then resuspended in appropriate media (DMEM for U87 cells and McCoy's media for A204 cells, each with 10% fetal bovine serum and 1% penicillin/streptomycin), and the cell concentration was determined using a Countess cell counter

(Invitrogen). After the initial cell concentration was determined, the suspension was diluted to 1.0 × 10_5 cells/mL. Next, a multichannel pipet was used to fill a 96-well plate with 100 μL/well of the diluted cell suspension. The cell-loaded plates were then incubated for 24 h at 37 °C under an atmosphere of 5% CO_2 in order to allow the cells to completely adhere to the surface of the wells.

After 24 h cell incubation, 222 μL and 444 μL of stock SN-38/CUR-PNP and stock SN-38-only PNP dispersions, respectively, were diluted to a total volume of 1 mL in the appropriate media for each cell type described above. For free drug mixtures, stock solutions of 0.5 wt % SN-38 in DMSO and 2.5 wt % of CUR in DMSO were prepared. SN-38 and CUR stock solutions were then combined in various ratios and each of the mixtures was diluted in the appropriate media for each cell type described above to a concentration of 20 μM SN-38. Serial dilutions were carried out, and then 100 μL of each diluted stock was added to the appropriate well of the 96-well plate (containing ∼1.0 × 10_4 cells in 100 μL of appropriate media, as described above), in order to generate a range of different concentrations for analysis. The treated cells were incubated for 72 or 96 h at 37 °C under a 5% CO_2 atmosphere. In order to determine cell viability, 40 μL of CellTiter-Blue was added to each well after the predetermined incubation time was complete. After the addition of the CellTiter-Blue, the 96-well plates were incubated for 3 h (5% CO_2, 37 °C), and then fluorescence (λ_{ex} = 560 nm; λ_{em} = 590 nm) readings were recorded on a 96-well plate reader. Cell death was calculated for each well based upon the following formula:

$$\% \text{ Dead} = [1-\frac{(S-B_0)}{(B_t-B_0)}]\ x\ 100$$

where S is the sample reading (cells + drug + media), B_t is the average reading for the untreated population of cells (cells + media), and B_0 is the average reading of wells containing media only.

% Death vs. SN-38 concentration data sets which combined data from three separate SN-38/CUR-PNP preparations for each condition, were fit using OriginLab. Each data point in the curve (and its error bars) is derived from four separate technical replicates of the same PNP preparation and concentration. Curves were normalized to 0% cell death at the lowest drug concentrations, and fits were forced through 0 as the bottom asymptote. EC_{50} values were then determined by calculating the SN-38 concentration required to elicit a 50% reduction in cell viability, based on the fitted curves. Experimental errors on these values were determined on the basis of the quality of the fits.

2.3.11 Statistics and Data Handling.

For comparison of cytotoxicity data, dose−response curves were first established as described in the section on Cell-Culture and Antiproliferation Assays. Serial dilutions provided samples of seven different concentrations for testing. Triplicate samples were exact replicates (such that the same seven concentrations were tested in multiple wells). The OriginLab software was used to provide a best-fit curve of the combined data of the percentage cell death vs concentration, together with EC_{50} results and standard errors derived from the goodness of fit. To compare any two results, the combined standard error SE_c was calculated from the square root of the sum of the squares of the standard errors from the individual curve fits:

$$SE_C = \sqrt{SE_1^2 + SE_2^2}$$

Similarly, the combined degrees of freedom *DOF* were calculated based upon the number of concentration values (*N*) in each data set:

$$\mathrm{DOF} = [(N_1 - 1) + (N_2 - 1)]$$

N varied between 8 and 26 for each experiment; *DOF* was therefore equal to between 14 and 50 for each pairwise comparison. The difference between measured results (*t*) was then expressed in terms of units of combined standard error:

$$t = \frac{EC_1 - EC_2}{SE_c}$$

Finally, a *p* value was calculated using a two-tailed test. This was carried out with the TDIST function in Excel for all pairwise comparisons, using the equation:

$$p = \text{TDIST}(t, \text{DOF}, 2)$$

A similar methodology was used to compare half time data from *in vitro* release curves, except based on the number of values in each release series, $N = 6$ and DOF = 10 for pairwise comparisons.

For statistical comparisons where standard error could not be taken directly from a fitted curve, multiple measurements were carried out (at least three independent measurements per data point), and standard error was calculated as standard deviation across the measurements, divided by the square root of the number of samples:

$$SE = \frac{SD}{\sqrt{N}}$$

Two-tailed *p*-values were then calculated as above. In all cases, differences were assumed to be statistically significant when $p < 0.05$.

2.4 Results and Discussion

2.4.1 Effect of r_{CUR} on the Size and Polydispersity of SN-38/CUR-PNPs

In order to investigate the effect of added CUR on the size and polydispersity of SN-38/CUR-PNPs, we prepared a series of samples with constant initial SN-38-to-polymer ratio (w/w), $r_{SN\text{-}38}$ = 0.1, and various initial CUR-to-polymer ratios (w/w), r_{CUR} = 0, 0.1, 0.5, 0.75, 1.0, and 10. All samples in this series of experiments were prepared in the two-phase, gas-liquid microfluidic reactor (Figure 6) at a constant flow rate of Q = 200 μL/min. In previous work, we have shown that high-shear "hot spots" within this reactor lead to unique, flow-variable processing control of PNP sizes, drug loading, drug release rates, and cytotoxicity, providing an excellent platform for optimization of drug delivery formulations.[29-38] In the present case, we selected the constant flow rate based on preliminary optimization experiments; the effect of microfluidic flow rate on SN-38/CUR-PNPs will be described later in the dissertation.

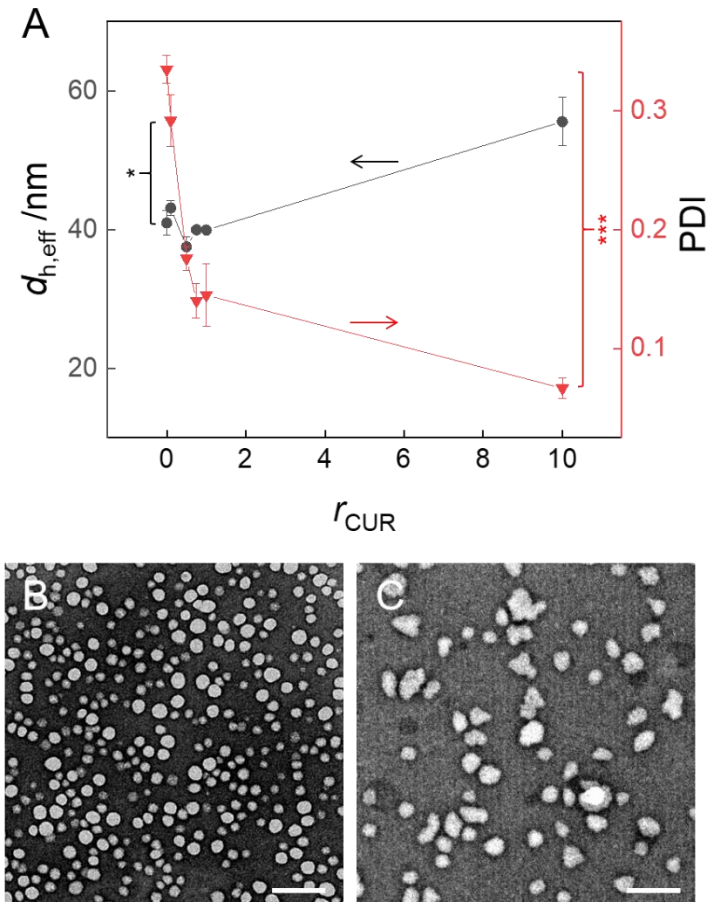

Figure 7. Effect of initial CUR-to-polymer ratio (w/w), r_{CUR}, on the size and polydispersity of SN-38/CUR-PNPs. Reproduced with permission.

(A) Plots of effective hydrodynamic diameter (dh,eff, black data points) and polydispersity index (PDI, red symbols) from DLS measurements vs. r_{CUR}. Statistical comparisons between r_{CUR} = 0 and r_{CUR} = 10 conditions indicate a significant difference (; $p < 0.05$) between dh,eff values and an extremely significant difference (***; $p < 0.001$) between PDI values. All samples were prepared with constant initial SN-38-to-polymer ratio, r_{SN-38} = 0.1, in the microfluidic reactor at a constant flow rate of Q = 200 µL/min. Selected TEM images of the SN-38/CUR-PNPs prepared with (B) r_{CUR} = 0.5 and (C) r_{CUR} = 10. Scale bars are 200 nm.*

Figure 7, A shows plots of effective hydrodynamic diameters ($d_{h,eff}$, black data points) and polydispersity indices (PDI, red symbols)— both determined from cumulant analysis of DLS data— vs. r_{CUR} for the resulting SN-38/CUR-PNPs. In both plots, the first data point (r_{CUR} = 0) describes PNPs containing only SN-38 (no CUR), with $d_{h,eff}$ = 41 nm and PDI = 0.33. For moderate CUR-to-polymer ratios (r_{CUR} = 0.1–1), we find no clear effect of CUR addition on mean PNP sizes, with all SN-38/CUR-PNPs showing $d_{h,eff}$ values close to that of PNPs containing only SN-

38, in the range of 38–43 nm. Only at a markedly higher CUR-to-polymer ratio does the effective hydrodynamic diameter increases significantly, from $d_{h,eff}$ = 40 nm at r_{CUR} = 1 to $d_{h,eff}$ = 56 nm at r_{CUR} = 10. On the other hand, we find that polydispersity values of SN-38/CUR-PNPs decrease significantly and monotonically with even moderate amounts of added CUR, dropping from PDI = 0.33 for r_{CUR} = 0 (SN-38 only) to PDI = 0.14 for r_{CUR} = 1. This is followed by a further decrease in polydispersity to PDI = 0.07 as r_{CUR} increases to 10, indicating that the SN-38/CUR-PNPs become essentially monodispersed at the highest CUR amount investigated. Considering the importance of low-polydispersity nanocarriers for drug delivery applications[44,146,159,177] this unexpected effect of CUR co-encapsulation indicates an added benefit of this approach for SN-38 nanomedicines.

Previous results from our group suggest a plasticizing effect of CUR which lowers the core crystallinity of PCL-*b*-PEG PNPs as the added CUR amount is increased.[88] This same effect may explain the observed decrease in PDI with increasing CUR-to-polymer ratios; less crystallinity within the PCL cores will increase the mobility of constituent copolymer chains, facilitating global equilibration and reducing kinetically trapped states that contribute to broadening of the PNP population. Indirect evidence of differences in core crystallinities with added CUR amounts comes from the TEM images in Figure 7, B and C. The TEM image of the r_{CUR} = 0.1 sample reveals mainly spherical PNPs on the grid (Figure 7 B), with white regions attributed to PCL cores in the reverse-contrast image. On the other hand, the TEM image of the r_{CUR} = 10 sample shows highly irregular particles with a broad range of sizes and shapes (Figure 7 C), despite the much lower PDI value (PDI = 0.07) of the corresponding aqueous dispersion compared to the r_{CUR} = 0.1 sample (PDI = 0.29). Therefore, the irregular appearance of particles in C (r_{CUR} = 10) appears to

be a drying artifact caused by the disruption of spherical cores on the TEM grid (Figure 7) as water is removed. This suggests a high degree of chain mobility due to low core crystallinity at the higher CUR content, in contrast to the r_{CUR} = 0.1 sample where the more crystalline (and therefore more robust) PNP cores retain their spherical shape upon removal of water (Figure 7 B).

2.4.2 Effect of r_{CUR} on SN-38 and CUR Encapsulation.

The same series of samples described in the previous section (r_{SN-38} = 0.1; Q = 200 µL/min; variable r_{CUR}) was also investigated by HPLC to determine SN-38 and CUR contents of the various SN-38/CUR-PNPs. From these measurements, encapsulation efficiencies of both drugs (EE_{SN-38} and EE_{CUR}) and the corresponding drug loadings (DL_{SN-38} and DL_{CUR}) were determined. Figure 22 shows the resulting plots of EE_{SN-38} (blue symbols) and EE_{CUR} (red symbols) vs. r_{CUR}; Figure 9 shows the corresponding plots of DL_{SN-38} (blue symbols) and DL_{CUR} (red symbols) vs. r_{CUR}.

The clear effect described by Figure 9 is a sharp and significant increase in SN-38 encapsulation as the initial relative CUR content in the formulation is increased. In Figure 9, we see the EE of SN-38 (blue symbols) increase from EE_{SN-38} = ~5% with no CUR added to the formulation (r_{CUR} = 0) to EE_{SN-38} = ~7% with the smallest amount of added CUR (r_{CUR} = 0.1). This is followed by a further jump in the SN-38 encapsulation, to EE_{SN-38} = ~12%, when the amount of added CUR is increased to r_{CUR} = 0.5. Further increases in the CUR-to-polymer ratio do not appear to have a significant effect on SN-38 encapsulation under the current conditions, and EE_{SN-38} remains

relatively constant even when the initial CUR amount is increased to 100× the initial SN-38 amount (r_{CUR} = 10).

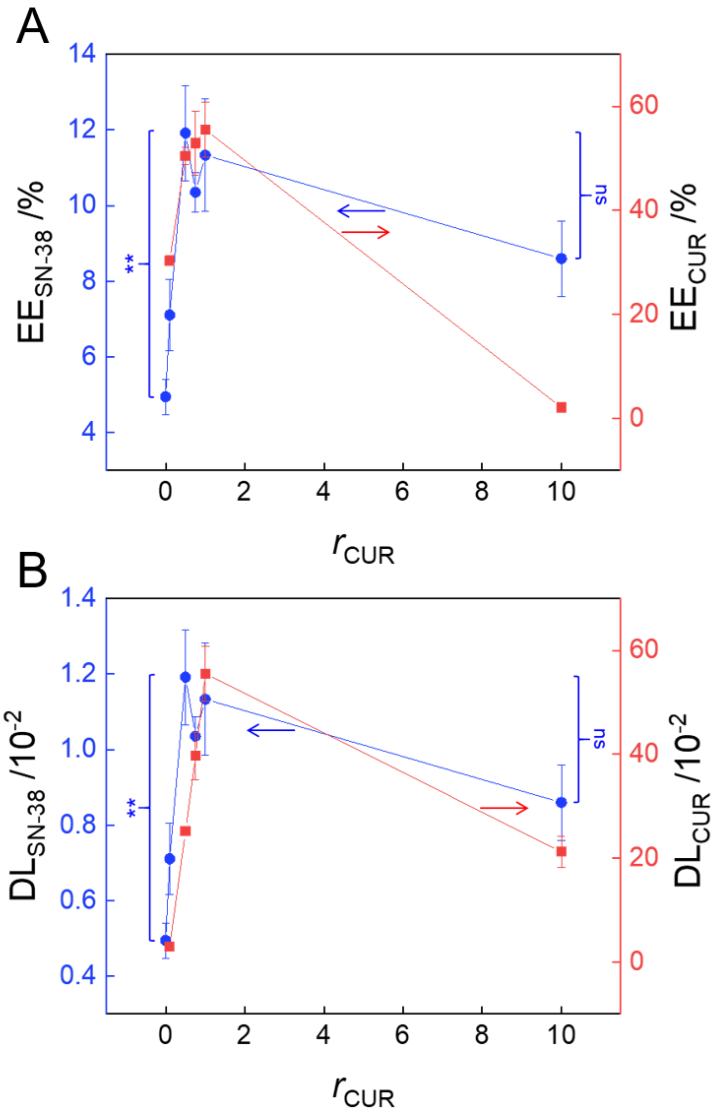

Figure 8. Effect of initial CUR-to-polymer ratio (w/w), rCUR, on the encapsulation efficiency (EE) and drug loading (DL) of SN-38 and CUR in SN-38/CUR-PNPs. Reproduced with permission.

*(A) Plots of EE_{SN-38} (blue symbols) and EE_{CUR} (red symbols) vs. r_{CUR}. (B) Plots of DL_{SN-38} (blue symbols) and DL_{CUR} (red symbols) vs. r_{CUR}. Statistical comparisons between r_{CUR} = 0 and r_{CUR} = 0.5 conditions indicate highly significant differences (**; p < 0.01) between both EE_{SN-38} (A) and DL_{SN-38} (B) values, confirming enhancement of SN-38 encapsulation with CUR co-encapsulation; statistical comparisons between r_{CUR} = 0.5 and r_{CUR} = 10 conditions indicate no significant differences (ns; p > 0.05) between either EE_{SN-38} (A) or DL_{SN-38} (B) values. All samples were prepared with constant initial SN-38-to-polymer ratio, r_{SN-38} = 0.1, in the microfluidic reactor at a constant flow rate of Q = 200 µL/min.*

The DL values plotted in Figure 9 describe the amounts of encapsulated SN-38 or CUR relative to the constant polymer mass, and so provide a more direct comparison of the relative amounts of both drugs in the PNP cores than the corresponding EE values Figure 9. Comparing plots of DL_{SN-38} (Figure 9, blue symbols) and DL_{CUR} (Figure 9, red symbols), we find that for the smallest amounts of added CUR (r_{CUR} = 0 to r_{CUR} = 0.5), increases in SN-38 encapsulation track with increases in CUR encapsulation, suggesting correlation between increased SN-38 encapsulation and the movement of CUR into the PNP cores. However, as initial CUR-to-polymer ratio further increases from r_{CUR} = 0.5 to r_{CUR} = 1, the amount of encapsulated CUR (DL_{CUR}, red symbols) continues to rise, while Figure 9, the amount of encapsulated SN-38 (DL_{SN-38}, blue symbols) remains relatively constant. This indicates a saturation point to the observed effect under the current conditions at r_{CUR} = 0.5; at this saturation point, we achieve a 2.4× enhancement in SN-38 encapsulation with an amount of added CUR equal to half the amount of excipient copolymer.

2.4.3 Comparing Effects of CUR Addition for Bulk and Microfluidic Methods.

We were interested in determining if the same advantages of added CUR described above (decreased PDIs and increased SN-38 encapsulation) could be realized in SN-38/CUR-PNPs prepared using simple bulk nanoprecipitation. We therefore prepared formulations under identical chemical conditions to those described in the previous sections (r_{SN-38} = 0.1; variable r_{CUR}) but using bulk rather than microfluidic nanoprecipitation. The effects of CUR addition on PNP size, polydipsersity, and SN38 encapsulation for bulk and microfluidic (Q = 200 µL/min) formulations were then compared head-to-head.

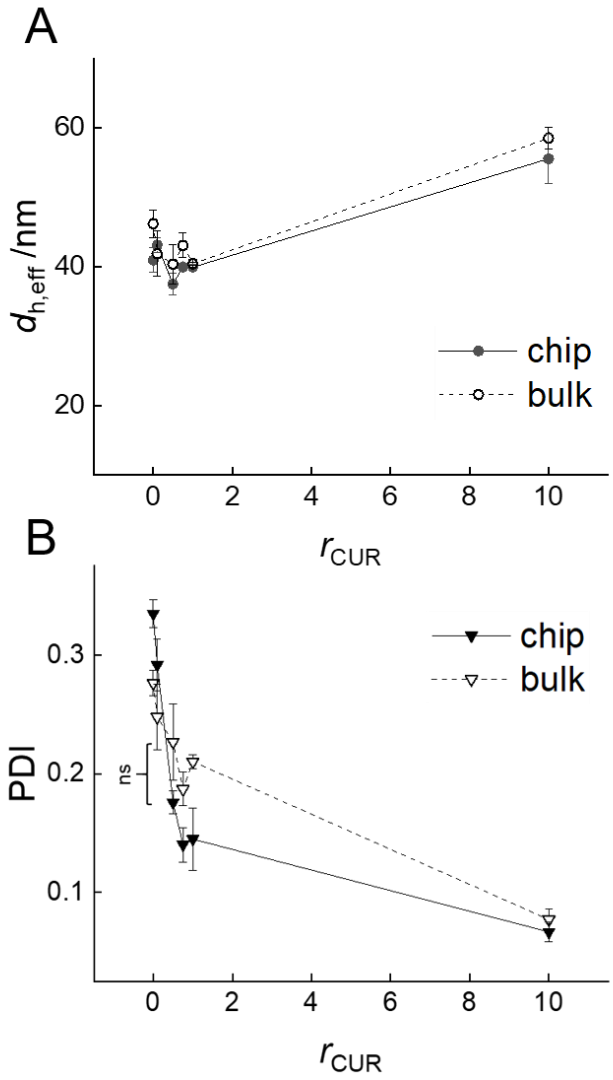

Figure 9. Comparison of bulk and microlfuidic methods on the size and polydispersity of SN-38/CUR-PNPs. Reproduced with permission.

(A) Plots of effective hydrodynamic diameter ($d_{h,eff}$) vs. r_{CUR} for bulk (open symbols) and microfluidic (closed symbols) formulations. (B) Plots of polydispersity index (PDI) vs. r_{CUR} for bulk (open symbols) and microfluidic (closed symbols) formulations. Statistical comparison between bulk and microfluidic methods at r_{CUR} = 0.5 indicate no significant difference (ns; $p > 0.05$) between PDI values. All samples were prepared with constant initial SN-38-to-polymer ratio, r_{SN-38} = 0.1; microfluidic preparations were carried out at a constant flow rate of Q = 200 µL/min.

Figure 10 compares plots of $d_{h,eff}$ (Figure 9A) and PDI (Figure 9B) vs. r_{CUR} for bulk (open symbols) and microfluidic (closed symbols) preparations. In Figure 9A, bulk and microfluidic plots show excellent overlap, indicating that the effect of mixing method on the sizes of SN-

38/CUR-PNPs over the investigated range of r_{CUR} values is negligible. In Figure 9B, we see that the same general trend of decreasing PDIs with increasing r_{CUR} described previously for microfluidic preparations at Q = 200 µL/min (closed symbols) is also found using simple bulk nanoprecipitation (open symbols). The microfluidic preparations appear to show a steeper initial drop in PDI values with increasing r_{CUR} than the bulk preparations. However, selective comparison of PDI values at r_{CUR} = 0.5 suggests that the difference between the plots is statistically insignificant when accounting for associated standard errors.

Bulk nanoprecipitation also yields similar trends in SN-38 and CUR encapsulation with increasing r_{CUR} to those described previously for microfluidic preparations, including marked enhancements in EE_{SN-38} values (Figure 10A). However, despite similarities in the overall trends, the method of preparation does appear to affect the amounts of SN-38 and CUR encapsulated in certain formulations, with the general observation that differences between bulk and microfluidic methods become less significant as r_{CUR} increases. For example, Figure 10A shows that, with no CUR addition (r_{CUR} = 0), EE_{SN-38} is significantly lower for the bulk method (~1%) compared to the microfluidic method (~5%). However, both methods lead to increasing EE_{SN-38} as r_{CUR} is increased, before reaching a common plateau of ~11 % at r_{CUR} = ~1. The lower SN-38 encapsulation at r_{CUR} = 0 means that the bulk method benefits from a larger maximum enhancement of SN-38 encapsulation as CUR is added (10×), compared to an enhancement of 2.4× using the microfluidic method. As well, Figure 10B shows similar trends for bulk and microfluidic methods of EE_{CUR} increasing to a maximum and then decreasing as r_{CUR} is increased.

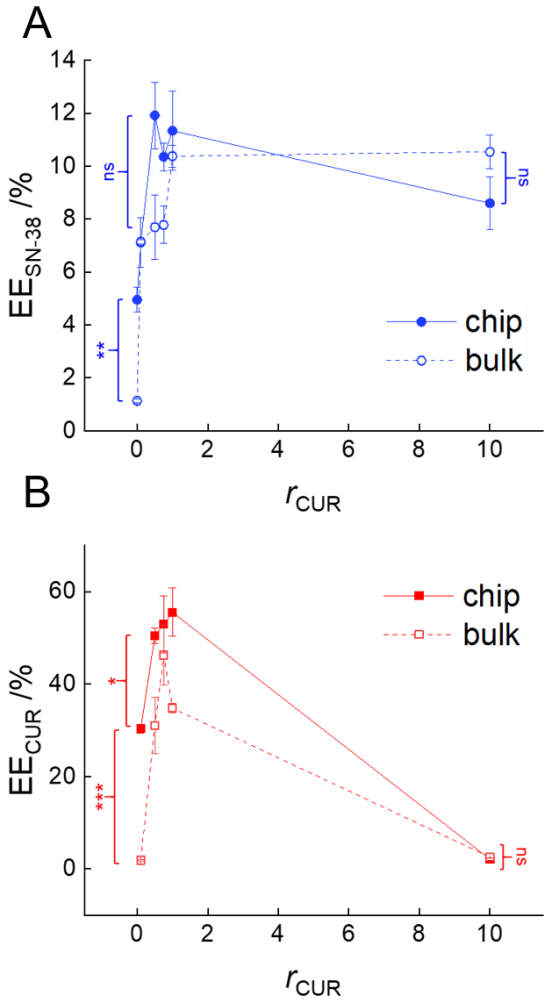

Figure 10. Comparison of bulk and microfuidic methods on SN-38 and CUR encapsulation in SN-38/CUR-PNPs. Reproduced with permission.

*(A) Plots of EE_{SN-38} vs. r_{CUR} for bulk (open symbols) and microfluidic (closed symbols) formulations. (B) Plots of EE_{CUR} vs. r_{CUR} for bulk (open symbols) and microfluidic (closed symbols) formulations. Statistical comparisons between bulk and microfluidic methods at r_{CUR} = 0 and r_{CUR} = 0.1 indicate a highly significant difference (**; $p < 0.01$) between EE_{SN-38} values (A) and an extremely significant difference (***; $p < 0.001$) between EE_{CUR} (B) values, respectively; statistical comparisons between bulk and microfluidic methods at r_{CUR} = 0.5 indicate no significant difference (ns; $p > 0.05$) between EE_{SN-38} values (A) and a significant difference (*; $p < 0.05$) between EE_{CUR} values (B); statistical comparisons between bulk and microfluidic methods at r_{CUR} = 10 indicates no significant differences (np; $p > 0.05$) between either EE_{SN-38} (A) and EE_{CUR} (B) values. All samples were prepared with constant initial SN-38-to-polymer ratio, rSN-38 = 0.1; microfluidic preparations were carried out at a constant flow rate of Q = 200 µL/min. These trends can be understood in terms of the maximum CUR capacity of the SN-38/CUR-PNP cores at rSN-38 = 0.1, with the drop in EE_{CUR} indicating more precipitated, unencapsulated CUR as the loading capacity is surpassed. As with EE_{SN-38} values, bulk EE_{CUR} values are generally lower than microfluidic values, with the differences between the methods decreasing and then becoming insignificant as r_{CUR} increases.*

These results show that the positive effects of CUR addition, including PDI lowering and EE_{SN-38} enhancement, are not specific to microfluidic mixing and can be realized using the commonly applied bulk nanoprecipitation method. In the present system, microfluidic effects at Q = 200 μL / min (including fast mixing and high shear) do not appear to significantly affect SN-38/CUR-PNP sizes and polydispersities. The current microfluidic environment does appear to promote higher encapsulation of both drugs at low r_{CUR} values, although interestingly this microfluidic advantage is erased by encapsulation enhancement as the amount of added CUR is increased. Since shear effects in two-phase gas-liquid microfluidic reactors are strongly flow rate-dependent[47,88,92,94,120,121] we will investigate more specifically the effects of different flow rates, Q, on a selected formulation in a later section.

2.4.4 Effect of r_{SN-38} on SN-38 and CUR Encapsulation.

We next investigated the effect of increasing the initial SN-38 amount on SN-38 and CUR encapsulation. For these experiments, we prepared a series of samples with constant initial CUR-to-polymer ratio (w/w), r_{CUR} = 0.5, and various initial SN-38-to-polymer ratios (w/w), r_{SN-38} = 0.1, 0.25, 0.50, and 0.75. All samples in this series of experiments were prepared in the microfluidic reactor at a constant flow rate of Q = 200 μL/min. We note that the r_{SN-38} = 0.1 case in this series is the same formulation that showed maximum SN-38 encapsulation in the series of different initial CUR amounts discussed previously.

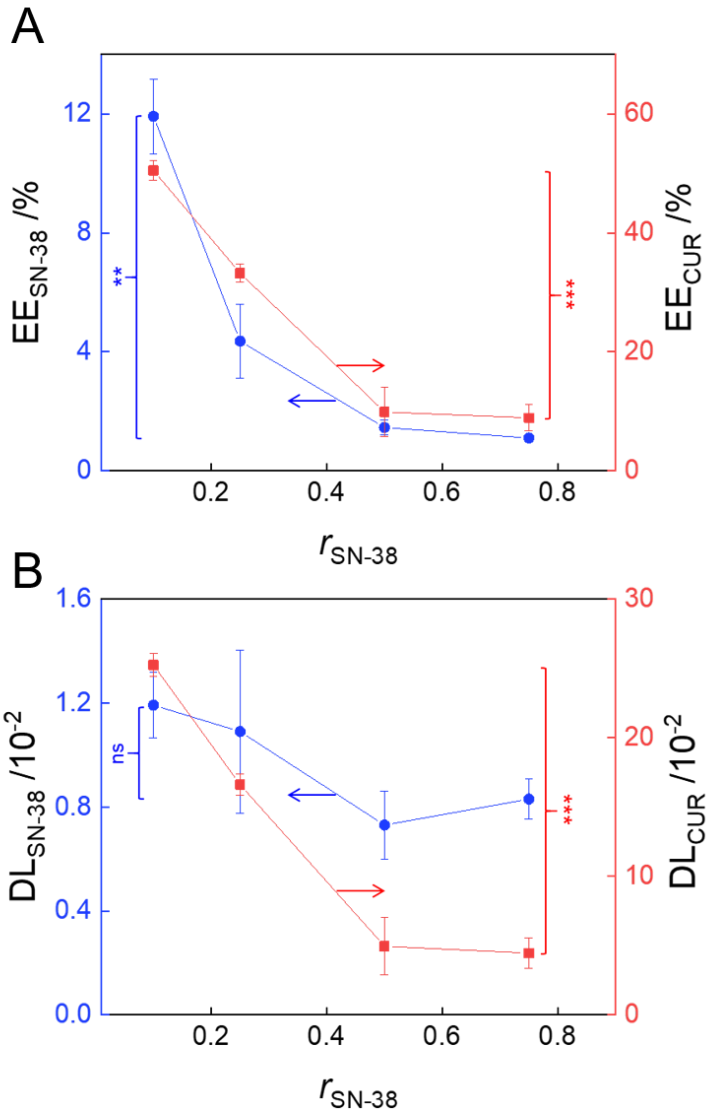

Figure 11. Effect of initial SN-38-to-polymer ratio (w/w), rSN-38, on the encapsulation efficiency (EE) and drug loading (DL) of SN-38 and CUR in SN-38/CUR-PNPs. Reproduced with permission.

*(A) Plots of $EE_{SN\text{-}38}$ (blue symbols) and EE_{CUR} (red symbols) vs. $r_{SN\text{-}38}$. (B) Plots of $DL_{SN\text{-}38}$ (blue symbols) and DL_{CUR} (red symbols) vs. $r_{SN\text{-}38}$. Statistical comparisons between $r_{SN\text{-}38}$ = 0.1 and $r_{SN\text{-}38}$ = 0.75 conditions indicate a highly significant difference (**; $p < 0.01$) and no significant difference (ns; $p > 0.05$) between EESN-38 (A) and DLSN-38 (B) values, respectively; statistical comparisons between $r_{SN\text{-}38}$ = 0.1 and $r_{SN\text{-}38}$ = 0.75 conditions indicate extremely significant differences (***; $p < 0.001$) between both EE_{CUR} (A) and DL_{CUR} (B) values. All samples were prepared with constant initial CUR-to-polymer ratio, r_{CUR} = 0.5, in the microfluidic reactor at a constant flow rate of Q = 200 µL/min.*

Figure 12 shows that $EE_{SN\text{-}38}$ (blue symbols) decreases sharply as the initial amount of SN-38 is increased. This indicates that the maximum capacity of the SN-38/CUR-PNP cores has been reached at $r_{SN\text{-}38}$ = 0.1 for the initial CUR amount of r_{CUR} = 0.5; increasing $r_{SN\text{-}38}$ therefore leads to

an increasing percentage of SN-38 precipitating from the formulation rather than becoming encapsulated, thus decreasing $EE_{SN\text{-}38}$. More interesting is the observation that EE_{CUR} (red symbols) also decreases with increasing $r_{SN\text{-}38}$, tracking closely with the trend in $EE_{SN\text{-}38}$. In Figure 11B, we see that as $r_{SN\text{-}38}$ increases from 0.1 to 0.75, the relative amount of SN-38 in the core ($DL_{SN\text{-}38}$, blue symbols) appears to drop by ~30% compared to its initial value (although the statistical significant of the decrease cannot be confirmed due to associated experimental error). Such a decrease can be explained by a faster rate of SN-38 precipitation outside the cores at higher initial concentrations, which would draw encapsulated SN-38 from the cores based on Le Chatelier's principle. Interestingly, as encapsulated SN-38 appears to decrease slightly, encapsulated CUR (DL_{CUR}) decreases sharply by ~80% compared to its initial value. An explanation for this trend will be discussed in a later section in connection with possible mechanisms of CUR enhancement of SN-38 encapsulation.

2.4.5 Effect of Microfluidic Flow Rate on SN-38/CUR-PNPs.

In order to investigate the effect of microfluidic flow rate on SN-38/CUR-PNPs, we prepared a series of samples with the same chemical composition, described by an initial SN-38-to-polymer ratio (w/w), $r_{SN\text{-}38} = 0.1$ and an initial CUR-to-polymer ratio (w/w), $r_{CUR} = 0.5$ and various flow rates Q = 0, 50, 100, 200, and 400 μL/min, where 0 μL/min represents the bulk method. We note that the Q = 200 μL/min and Q = 0 μL/min conditions in this series represent the same microfluidic and bulk formulations, respectively, discussed in previous sections.

Considering first the sizes and polydispersities of SN-38/CUR-PNPs at various flow rates (Figure 12A), we find only small differences in $d_{h,eff}$ (black symbols) between Q = 0 μL/min and

Q = 400 μL/min, with all sizes falling in the range of 37-47 nm. The observed trend of $d_{h,eff}$ increasing through a maximum and then decreasing as Q increases is consistent with an on-chip competition between shear-induced breakup and shear-induced coalescence, as described previously by our group.[69,94] In general, PDI (red symbols) tracks well with $d_{h,eff}$, with the exception of the transition from Q = 200 μL/min to Q = 400 μL/min, which gives rise to a spike in PDI (from 0.18 to 0.27) despite a corresponding small decrease in $d_{h,eff}$ (from 38 to 37 nm).

In Figure 13, we find a steady increase in EE_{CUR} (red symbols) with increasing Q, as we have found previously for CUR encapsulation using an identical microfluidic reactor in the absence of SN-38.[88] In that paper, this trend was attributed to increasing Q facilitating better contact between CUR and the PCL blocks, leading to greater plasticization of PCL crystallites and a greater amorphous core volume for CUR encapsulation.[88] On the other hand, our past study of SN-38 encapsulation in the same reactor without CUR showed no effect of Q on EE_{SN-38}.[120] However, Figure 12B shows a general trend of EE_{SN-38} (blue symbols) increasing with Q (despite an anomalous decrease at Q = 400 μL/min), providing further evidence for the correlation between SN-38 and CUR encapsulation within this system.

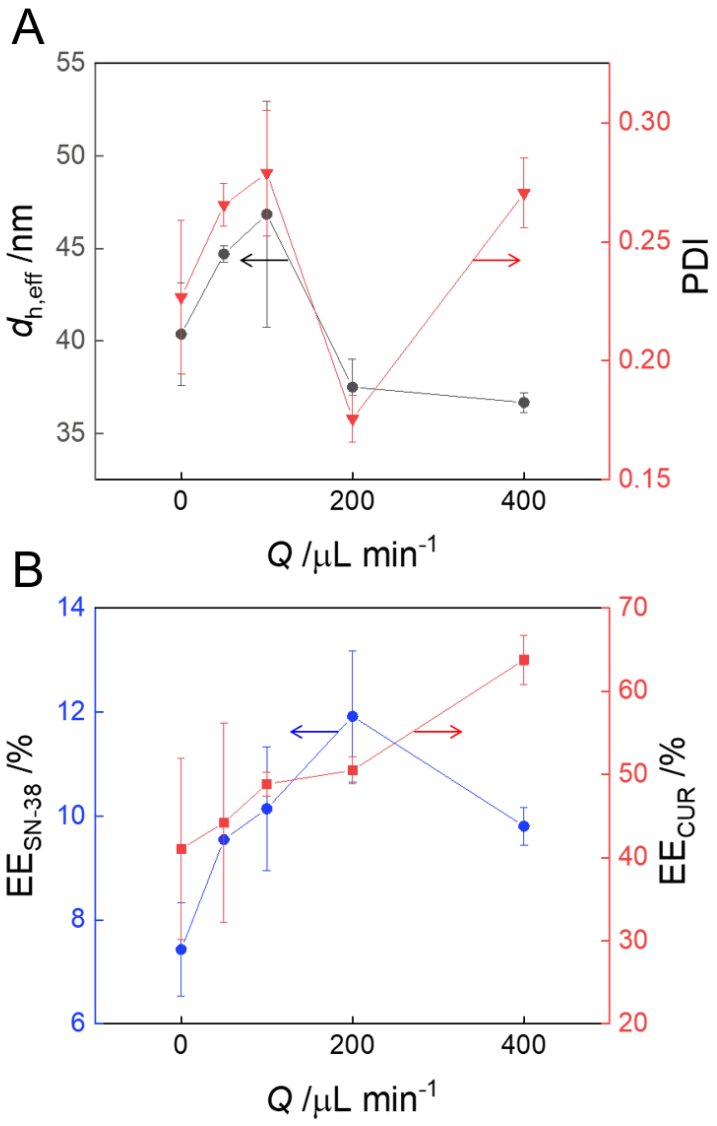

Figure 12. Effect of microfluidic flow rate, Q, on the size, polydispersity, and drug encapsulation of SN-38/CUR-PNPs. Reproduced with permission.

(A) Plots of $d_{h,eff}$ (black symbols) and PDI (red symbols) vs. Q. (B) Plots of EE_{SN-38} (blue symbols) and EE_{CUR} (red symbols) vs. Q. All samples were prepared with constant initial SN-38-to-polymer ratio, r_{SN-38} = 0.1, and constant initial CUR-to-polymer ratio, r_{CUR} = 0.5. All samples were prepared in the microfluidic reactor except Q = 0 μL/min, which represents the bulk method.

2.4.6 Precipitation of SN-38/CUR Blends Without Copolymer.

In order to obtain insights into the mechanism of CUR enhancement, we wanted to determine if CUR increased the dispersion of SN-38 in the solvent environment of SN-38/CUR-PNP formation.

With this goal, we carried out precipitation experiments into 10× excess water of various DMF solutions containing different amounts of SN-38 and CUR; these experiments were identical to the process of bulk SN-38/CUR- PNP formation except with no copolymer added to the DMF solutions. Normalized initial SN-38 and CUR concentrations in DMF are described using equivalent drug-to-copolymer ratios, which are defined in terms of the initial copolymer concentration that would be present in the case of PNP formation (0.33 wt %):

$$r_{eq} = \frac{concentration\ of\ drug}{0.33\ wt\%}$$

Unlike SN-38/CUR-PNP formation, samples were not dialyzed following precipitation into water. Instead, the two-phase mixtures were immediately centrifuged (16,000 × g for 10 min) to separate the clear dispersions from precipitated drug, then the SN-38 and CUR contents of the supernatants were analyzed within 3h to determine dispersion efficiencies (DE) of both drugs. We define DE as follows:

$$DE(\%) = \frac{mass\ dispersed\ drug}{total\ mass\ drug} x\ 100$$

For the discussion below, the initial CUR/SN-38 ratio, R_i, and the dispersed CUR/SN-38 ratio, R_{disp}, are defined as follows:

$$R_i = \frac{r_{eq,CUR}}{r_{eq,SN-38}}$$

$$R_{disp} = \frac{DE_{CUR} x r_{eq,CUR}}{DE_{SN-38} x r_{eq,SN-38}}$$

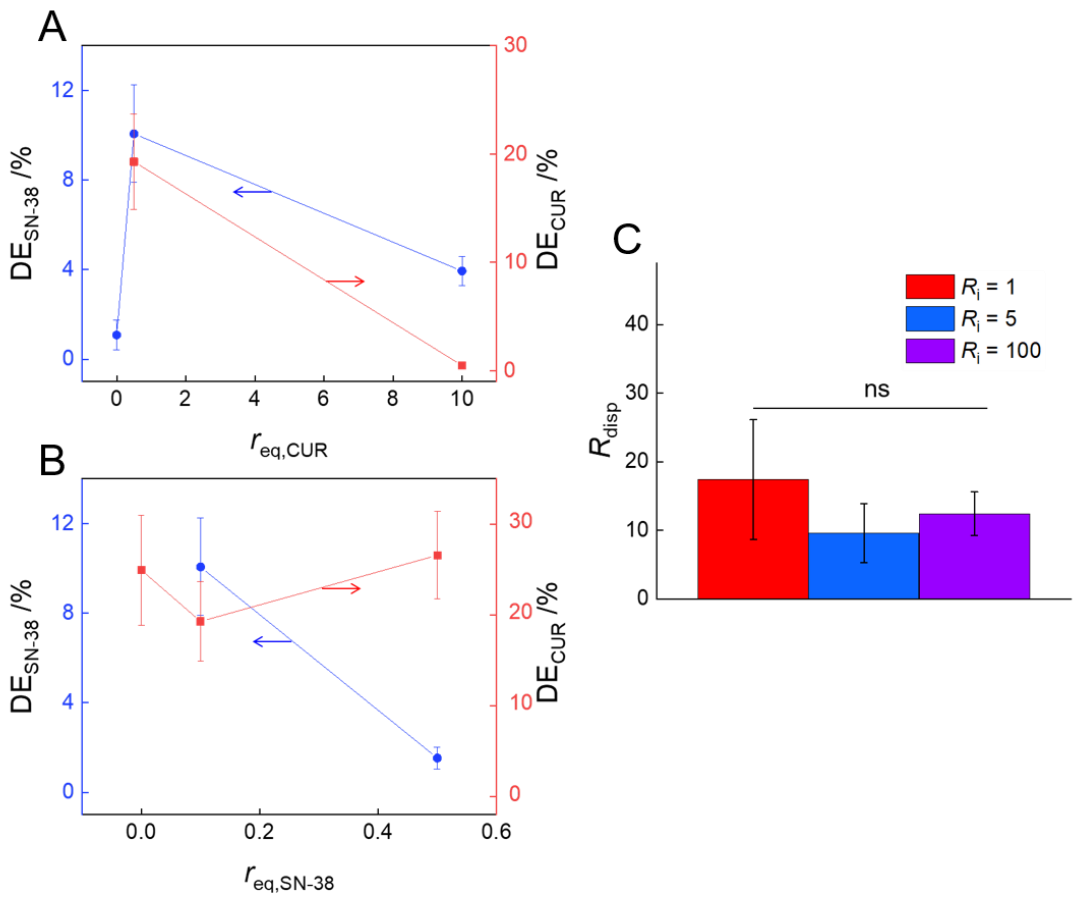

Figure 13. Dispersion efficiencies of SN-38 and CUR following precipitation of various SN-38/CUR blends without copolymer in DMF into water. Reproduced with permission.

(A) Plots of $DE_{SN\text{-}38}$ (blue symbols) and DE_{CUR} (red symbols) vs. $r_{eq,CUR}$ for constant $r_{eq,SN\text{-}38}$ = 0.1. (B) Plots of $DE_{SN\text{-}38}$ (blue symbols) and DE_{CUR} (red symbols) vs. $r_{eq,SN\text{-}38}$ for constant $r_{eq,CUR}$ = 0.5. (C) R_{disp} (dispersed CUR/SN-38 ratios) for various values of R_i (initial CUR/SN-38 ratios); statistical comparison indicates no significant difference (ns; $p > 0.05$) in R_{disp} values (np; $p > 0.05$) for three different R_i values.

Figure 14A plots $DE_{SN\text{-}38}$ (blue symbols) and DE_{CUR} (red symbols) with increasing $r_{eq,CUR}$ and constant $r_{eq,SN\text{-}38}$ = 0.1. When no CUR is present in the blend solution ($r_{eq,CUR}$ = 0), only ~1% of the initial SN-38 remains dispersed in the final solvent medium of 90/10 (w/w) water/DMF following removal of precipitated drug. This result is not surprising, considering the expected low solubility of SN-38 in a mostly aqueous solvent mixture. However, we find that $DE_{SN\text{-}38}$ jumps from ~1 wt % to ~10 wt % when CUR is added to the blend solution ($r_{eq,CUR}$ = 0.5), while DE_{CUR} is measured to be

~19 wt %. This indicates that the presence of the more dispersible CUR increases the dispersion of SN-38 in the water/DMF medium. When the initial CUR amount is increased significantly to $r_{eq,CUR}$ = 10, a much larger percentage of the CUR precipitates in the water/DMF mixture, leading to an expected drop in DE_{CUR}; in addition, we find a corresponding drop in DE_{SN-38}.

Considering the effect of increasing $r_{eq,SN-38}$ on DE_{SN-38} and DE_{CUR} at constant $r_{eq,CUR}$ = 0.5 (Figure 14B), we find very little effect of the presence or amount of SN-38 on CUR dispersion in the final medium. Between $r_{eq,SN-38}$ = 0 and $r_{eq,SN-38}$ = 0.5, DE_{CUR} (red symbols) varies non-monotonically between ~19 % and ~27 %; the absence of a discernible trend and the large associated errors suggest that the effect initial SN-38 concentration is either weak or non-existent. Not surprisingly, DE_{SN-38} (blue symbols) drops sharply between $r_{eq,SN-38}$ = 0.1 to $r_{eq,SN-38}$ = 0.5, as a larger percentage of SN-38 precipitates at the higher initial SN-38 concentration in DMF.

From Figure 14, A and B, we identify three unique blend compositions containing both drugs in DMF (with different initial CUR/SN-38 ratios, R_i) that were precipitated into excess water: 1. $r_{eq,CUR}$ = 0.5 and $r_{eq,SN-38}$ = 0.5 (Figure 13 B; R_i = 1); 2. . $r_{eq,CUR}$ = 0.5 and $r_{eq,SN-38}$ = 0.1 (Figure 13, A and B; R_i = 5); and 3. $r_{eq,CUR}$ = 10 and $r_{eq,SN-38}$ = 0.1 (Figure 13A; R_i = 100). For each initial CUR/SN-38 ratio in DMF (R_i), we calculated the final CUR/SN-38 ratio dispersed in water/DMF (R_{disp}), and these values are plotted in Figure 13C. The surprising result is that we find no significant difference for R_{disp} values over the 2-order-of-magnitude difference in R_i; we further determine an average dispersed ratio of R_{disp} = 13 ± 4 for the three compositions (or ~13 CUR molecules for every SN-38 molecule, considering the similar molecular weights of CUR and SN-38). A "magic number" of ~13 CUR molecules per SN-38 molecule in the 90/10 (w/w) water/DMF environment suggests a

preferred association structure formed through H-bonding and van der Waals interactions, independent of initial drug concentrations; the existence of such SN-38/CUR interactions would explain the observed increased dispersion of SN-38 in precipitated blends of the two drugs. Future work will seek to uncover further details on the bonding interactions, structure and long-term stability of the resulting SN-38/CUR dispersions formed in the absence of copolymer.

2.4.7 Discussion of Possible Mechanisms of CUR Enhancement of SN-38 Encapsulation.

We consider several possible contributions to the observed enhancement of SN-38 encapsulation in SN-38/CUR-PNPs. Firstly, in a previous study from our group, it was shown that CUR can act as a plasticizer for PCL cores, as evidenced by an increased loading capacity as the initial CUR amount increased; this suggested that CUR interactions with the core decreased the crystallite content and increased the amorphous volume for drug loading.[88] The existence of a similar CUR plasticizing effect appears to be operative in the present system, as indicated by an increase in EE_{CUR} values with increasing r_{CUR} for both microfluidic and bulk preparations (Figure 14B). In addition, the effect of r_{CUR} on PDI values for both preparation methods (Figure 10B) is also consistent with PCL cores becoming plasticized by added CUR, as discussed in a previous section. Therefore, as an increased amount of CUR is added, the resulting increase in the amorphous volume of the micelle core is expected to increase the loading capacity for both drugs and therefore contribute to the enhancement of SN-38 encapsulation.

Secondly, the experiments discussed in the previous section provide evidence for attractive SN-38/CUR interactions in the solvent environment of self-assembly, which we expect will further contribute to the observed enhancement effect. As shown in Figure 14, CUR is found to increase

the dispersion of SN-38 in an environment of 90/10 (w/w) water/DMF, identical to the solvent environment of bulk self-assembly, with HPLC analysis indicating ~13 CUR molecules per SN-38 molecule in various dispersions formed from different initial drug ratios. In the presence of copolymer, such an increase in SN-38 dispersion through the formation of intermolecular association structures with CUR would decrease its precipitation from the solvent medium of self-assembly, allowing more SN-38 to migrate into the cores.

Finally, we consider the additional contribution of attractive SN-38/CUR interactions in the micelle cores. Since CUR has a higher affinity for the PCL cores than SN-38, as evidenced by encapsulation data in Figure 9 along with additional references,[41,42] positive interactions between SN-38 and CUR molecules within the core are expected to increase the encapsulation of the former. Indirect evidence for such SN-38/CUR interactions within the micelle cores comes from the observed sharp drop in encapsulated CUR as the initial SN-38 amount increases (Figure 8B). One possible explanation is that as encapsulated SN-38 is drawn from the cores by the increased rate of SN-38 precipitation outside the cores, attractive SN-38/CUR interactions lead to a tandem migration of encapsulated CUR molecules, giving rise to the trend in Figure 9B.

The considerations above provide a qualitative analysis of the possible contributions of core plasticization and attractive SN-38/CUR interactions in both the solvent and core media to the observed CUR enhancement of SN-38 encapsulation. Further experimental work and analysis is required to elucidate more quantitatively the relative importance of these contributions under different experimental conditions.

2.4.8 Release Kinetics of SN-38 and CUR from SN-38/CUR-PNPs.

Based on the results described above, we chose three formulations to carry forward for subsequent characterization, including *in vitro* release kinetics and cytotoxicity assays. The three selected formulations are designated according to their initial CUR/SN-38 ratios ($R_i = r_{CUR}/r_{SN-38}$) as follows: 1. SN-38-PNP was prepared with $r_{CUR} = 0$ and $r_{SN-38} = 0.1$ ($R_i = 0$); 2. SN-38/CUR_5-PNP was prepared with $r_{CUR} = 0.5$ and $r_{SN-38} = 0.1$ ($R_i = 5$); and 3. SN-38/CUR_{100}-PNP was prepared with $r_{CUR} = 10$ and $r_{SN-38} = 0.1$ ($R_i = 100$). All three formulations were prepared using the microfluidic reactor at constant flow rate (Q = 200 µL/min). Pertinent physicochemical characteristics of the three selected formulations are provided in Table 1.

Table 1. Physicochemical Characteristics of Selected Formulations. Reproduced with permission.

Formulation	$d_{h,eff}$ / **nm**	**PDI**	DL_{CUR} / 10^{-2}	DL_{SN-38} / 10^{-2}	$t_{1/2,CUR}$ / **h**	$t_{1/2,SN-38}$ / **h**
SN-38-PNP	41 ± 2	0.33 ± 0.01	N/A	0.49 ± 0.05	N/A	0.7 ± 0.1
SN-38/CUR_5-PNP	38 ± 2	0.18 ± 0.01	25.2 ± 0.8	1.2 ± 0.1	5 ± 1	0.9 ± 0.3
SN-38/CUR_{100}-PNP	56 ± 4	0.07 ± 0.01	21 ± 3	0.9 ± 0.1	1.0 ± 0.4	0.42 ± 0.07

Figure 14A shows the SN-38 release curve for the SN-38-PNP control formulation and Figure 14, B and C show simultaneous CUR and SN-38 release curves for the SN-38/CUR_5-PNP and SN-38/CUR_5-PNP formulations. Corresponding SN-38 and CUR release half times are compared in Figure 14D. We find a significantly shorter CUR release half time in the SN-38/CUR_{100}-PNP formulation ($t_{1/2,CUR}$ = ~1 h) compared to the SN-38/CUR_5-PNP formulation ($t_{1/2,CUR}$ = ~5 h), despite the amount of encapsulated CUR (DL_{CUR},Table 1) in the two formulations not being significantly different. The faster release rate in the SN-38/CUR_{100}-PNP case may be due to the plasticization

effect of higher initial CUR amounts discussed previously; more dynamic, less crystalline cores in the SN-38/CUR_{100}-PNP sample would lead to faster CUR diffusion and explain the resulting shorter $t_{1/2,CUR}$ values. We find that SN-38 release is faster than CUR release in both formulations containing the two drugs. We also note a small decrease in $t_{1/2,SN\text{-}38}$ values between the SN-38/CUR_5-PNP and SN-38/CUR_{100}-PNP formulations, consistent with the corresponding decrease in $t_{1/2,CUR}$ values. However, Student's t-tests reveal no significant differences in $t_{1/2,SN\text{-}38}$ values across all three formulations (Figure 14D), suggesting that SN-38 release rates are not strongly affected by initial CUR amounts.

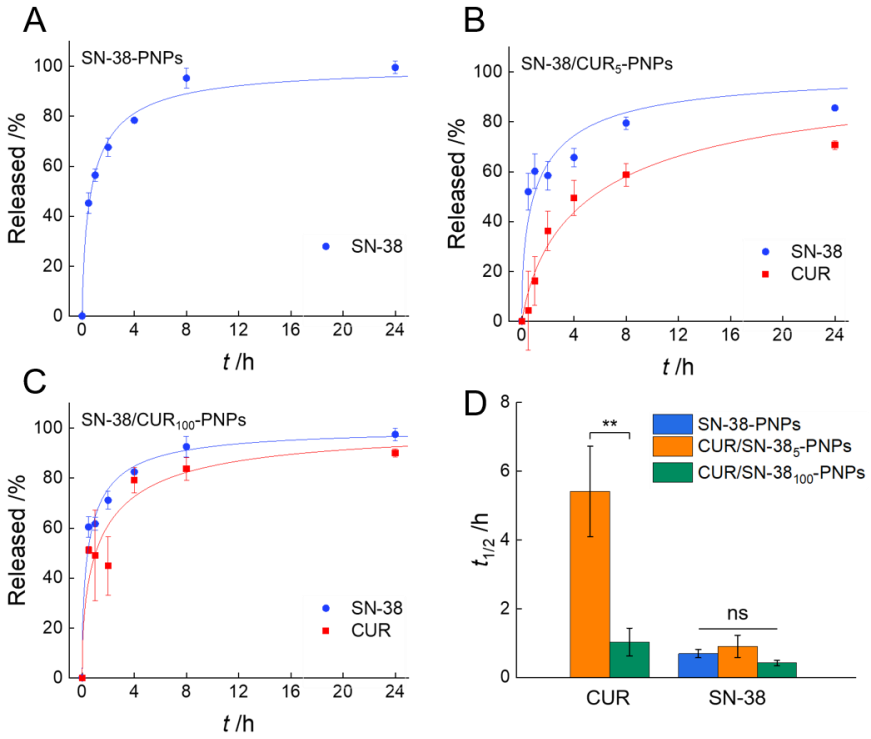

Figure 14. Release kinetics of SN-38 and CUR from selected SN-38/CUR-PNP formulations. Reproduced with permission.

*(A-C) In vitro release curves for SN-38 (blue symbols) and CUR (red symbols) from (A) SN-38-PNPs (R_i = 0), (B) SN-38/CUR_5-PNPs (R_i = 5), and (C) SN-38/CUR_{100}-PNPs (R_i = 100); the associated fits to the release data were obtained as described in the text. (D) Release half times ($t_{1/2}$) for CUR and SN-38 for the three formulations determined from the fits in (A-C). Statistical comparisons indicate a highly significant difference (**; $p < 0.01$) between the two $t_{1/2,CUR}$ values and no significant difference (ns; $p > 0.05$) between all three $t_{1/2,SN\text{-}38}$ values.*

2.4.9 *In Vitro* SN-38-PNP and SN-38/CUR-PNP Cytotoxicity.

The three selected formulations described in Table 1 were next tested for cytotoxic effects against two different cell lines: the human rhabdomyosarcoma (RMS) cell line A204 and the human glioblastoma, astrocytoma cell line U87. Free, unencapsulated drugs, including SN-38 and two different SN-38/CUR blends, were evaluated as positive controls, and empty PNPs without CUR or SN-38 were evaluated as negative controls. Raw cytotoxicity data and fits used to arrive at reported EC_{50} values and associated experimental error are presented in Appendix 1.

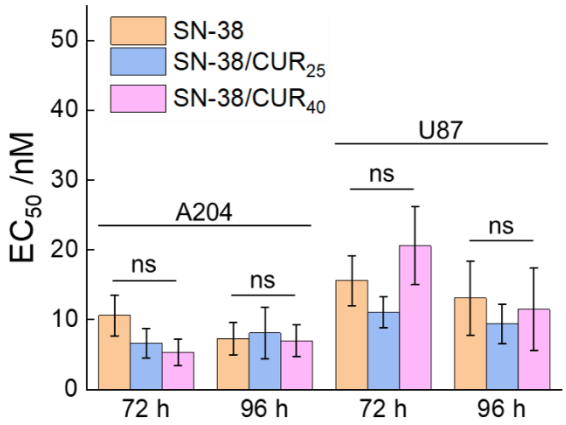

Figure 15. Potency of positive controls against A204 and U87 cancer cells. Reproduced with permission.

The chart shows EC_{50} values for free SN-38 and free SN-38/CUR blends of two different compositions (72 h and 96 h incubation times). Statistical comparisons indicate no significant differences (ns; $p > 0.05$) in potency for the three controls against either cell line and for either incubation time.

The potency of the three free drug formulations were first investigated against both cell lines at two different incubations times (Figure 15). The three formulations included free SN-38 and two free SN-38/CUR blends (SN-38/CUR_{25} and SN-38/CUR_{40} with 25 and 40 mg CUR per mg of SN-

38, respectively); the SN-38/CUR_{25} formulation was selected based on the approximate ratio of encapsulated CUR:SN-38 in both of the CUR-containing PNP formulations in Table 1, with the SN-38/CUR_{40} selected to investigate the possible cytotoxic effect of a higher CUR amount. However, the EC_{50} values of the three formulations showed no significant difference in potency against either cell line at either incubation time. Our results suggest that CUR has neither a negative nor positive effect on SN-38 activity against A207 or U87 cell lines *in vitro*, although that does not rule out potential therapeutic benefits of CUR in anticancer drug delivery applications, underlining the need for future *in vivo* studies. Our negative controls indicated only a weak effect of empty PNPs on both cell lines at a copolymer concentration equal to the highest concentration present in cytotoxicity tests of SN-38/CUR-PNPs; at a copolymer concentration of 0.07 mg / mL, empty PNPs results in <5 % cell death in U87 and < 30% cell death in A204 cell lines (Appendix 1, Table 3: EC50 values of Cytotoxicity Assays for Various Nanoparticle and Free Drug Formulations).

Next, cytotoxicity assays of the three PNP formulations listed in Table 1were carried out against both A204 and U87 cells (Figure 16). Figure 16A compares potencies against A204 cells of free SN-38 with the three selected PNP formulations, SN-38-PNP (no CUR), SN-38/CUR_{100}-PNP (high CUR), and SN-38/CUR_5-PNP (low CUR). Interestingly, SN-38-PNP and SN-38/CUR_{100}-PNP formulations show equivalent or lower EC_{50} values than free SN-38, whereas the SN-38/CUR_5-PNP formulation shows EC_{50} values significantly higher than the free drug. Comparing PNP formulations with different CUR amounts, the SN-38-PNP and SN-38/CUR_{100}-PNP formulations show roughly equivalent potencies within experimental error after 72 h (EC_{50} = ~4 nM and ~6 nm, respectively); however, after 96 h, the EC_{50} of the SN-38/CUR_{100}-PNP (high CUR) formulation

drops to ~0.8 nM, becoming more potent than the SN-38-PNP (no CUR) formulation (EC_{50} = ~4 nM; highly significant difference, $p < 0.01$). On the other hand, the SN-38/CUR_5-PNP (low CUR) formulation is markedly less potent than the other two PNP formulations, with EC_{50} = ~30 nM after 72 h and increasing to EC_{50} = ~39 nM after 96 h. These experiments indicate potential for applying CUR co-encapsulation to increase the potency of encapsulated SN-38 formulations against A204 cells, although the amount of co-encapsulated CUR appears to be critical in this respect, with low CUR amounts leading to decreased potency and high CUR amounts leading to increased potency.

The same formulation series was also tested against the U87 cell line (Figure 16B). In contrast to experiments against A204 cells, encapsulation led to a general decrease in SN-38 potency against U87 cells, with EC_{50} values for all three PNP formulations being equivalent or higher than free SN-38. Also in contrast to A204 experiments, we note that the 96-h potency of SN-38-PNP (no CUR, EC_{50} = ~7 nM) is significantly greater than both SN-38/CUR_5-PNP (low CUR, EC_{50} = ~67 nM) and SN-38/CUR_{100}-PNP (high CUR, EC_{50} = ~49 nM). These results suggest that CUR can have markedly different effects on the potency of co-encapsulated SN-38 against different cell lines, underlining the need for further mechanistic studies. A similar trend for both cell lines was the apparent lower potency of the SN-38/CUR_5-PNP formulation compared to the SN-38/CUR_{100}-PNP formulation, although against the U87 cell line the difference is not found to be statistically significant due to experimental error on the mean EC_{50} values. The particularly large relative error on the 72 h incubation time of the SN-38/CUR_5-PNP formulation is attributed to a combination of low potency and incomplete cell replication at the shorter time point, leading to large variability of cytotoxic response.

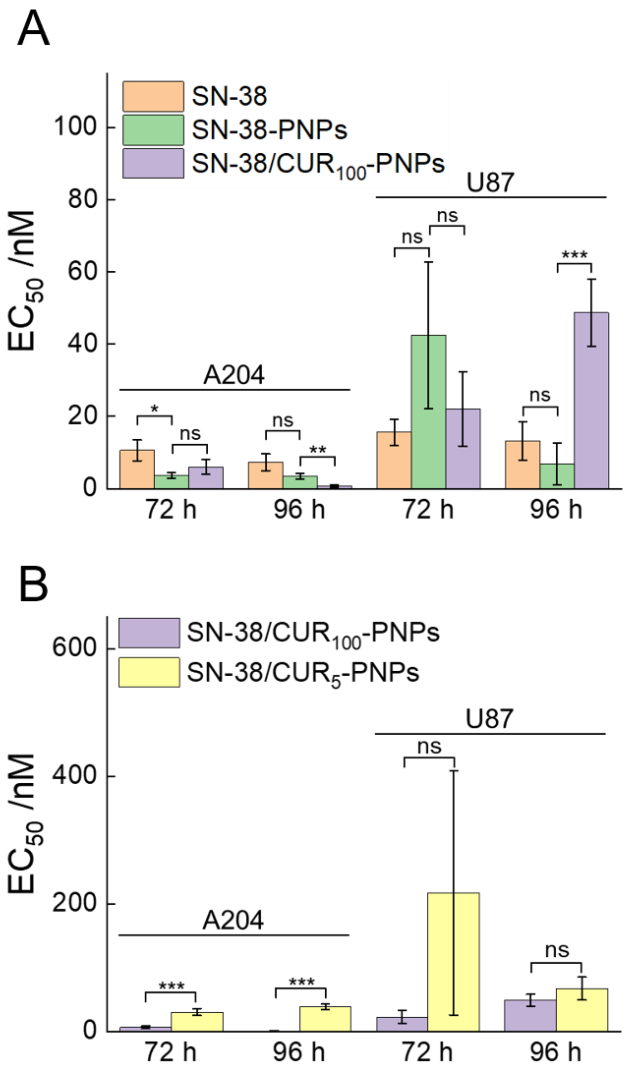

Figure 16. Potency of three PNP formulations and free SN-38 control against A204 and U87 cancer cells (72 h and 96 h incubation times). Reproduced with permission.

*(A) Chart comparing EC_{50} values of free SN-38 control with SN-38-PNP, SN-38/CUR_{100}-PNP, and SN-38/CUR_5-PNP formulations against A204 cells. (B) Chart comparing EC_{50} values of free SN-38 control with SN-38-PNP, SN-38/CUR_{100}-PNP, and SN-38/CUR_5-PNP formulations against U87 cells. Statistical comparisons indicate extremely significant (***; $p < 0.001$), highly significant (**; $p < 0.01$), significant (*; $p < 0.05$) and not significant (ns; $p > 0.05$) differences between values.*

Comparing the physicochemical properties of the three PNP formulations (Table 1), an explanation for the differences in EC_{50} values against both A204 and U87 cells is not immediately apparent. SN-38/CUR_5-PNP (low CUR) has a smaller mean size and a larger polydispersity than SN-38/CUR_{100}-

PNP (high CUR), although neither parameter on its own can explain the large difference in potency, since SN-38-PNP (no CUR) has a similar mean size to SN-38/CUR_5-PNP, along with a larger PDI, and yet shows EC_{50} values closer to those of SN-38/CUR_{100}-PNP (Figure 16). In addition, despite the difference in initial CUR-to-polymer ratios for the low-CUR and high- CUR formulations, they contain very similar encapsulated drug loadings of both SN-38 and CUR (Table 1).

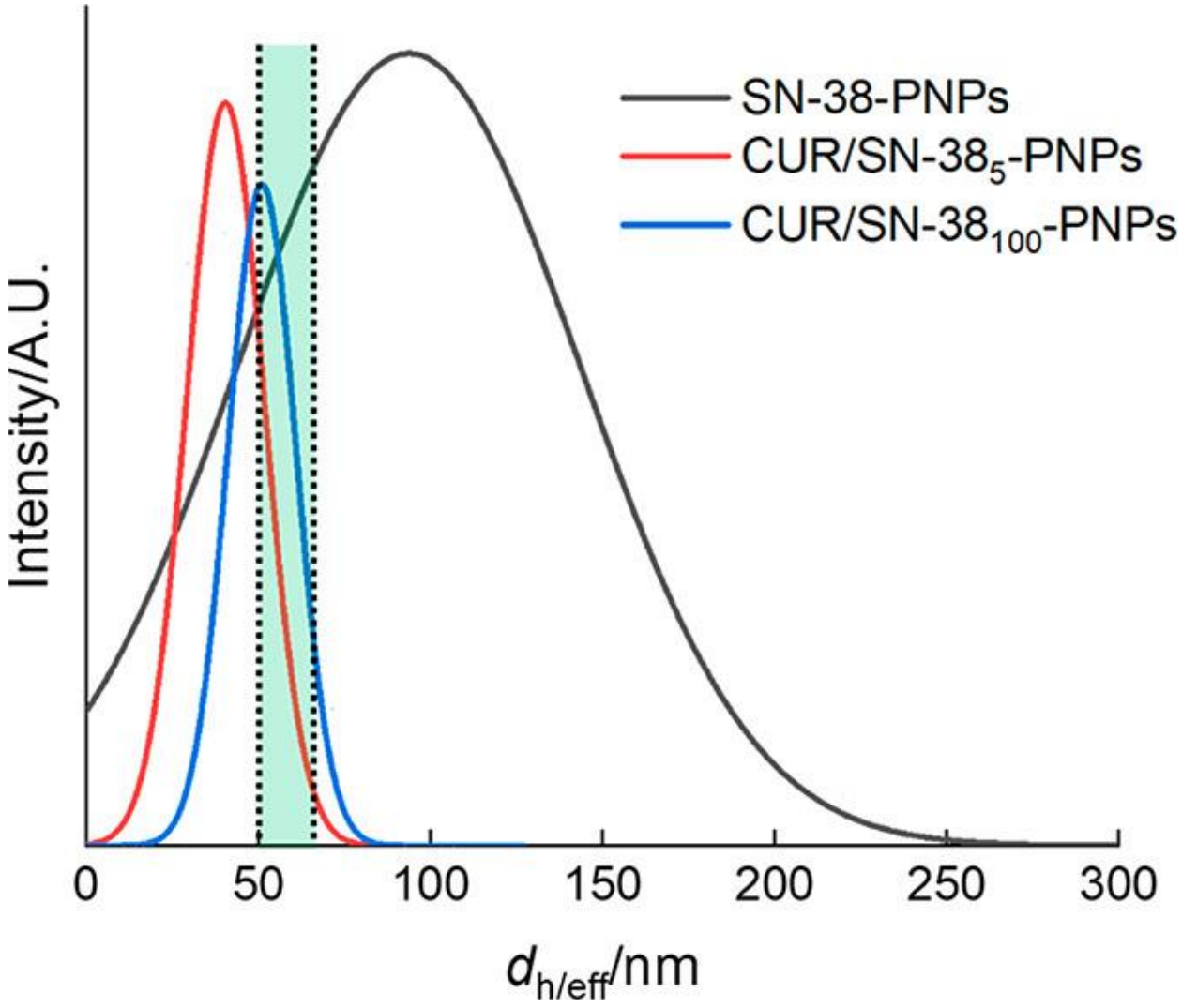

Figure 17. Representative size distributions for the three nanoparticule formulations tested against A204 and U87 cells. Reproduced with permission.

Lines represent Gaussian fits to CONTIN results from DLS measurements for each formulation. The transparent green region represents the 50-60 nm size regime assumed for optimal cell uptake. A tentative explanation for the relative potencies found in A204 cells comes from comparing representative CONTIN size distributions (best Gaussian fits) from DLS data for the three PNP formulations (Figure 17). The CONTIN distributions in Figure 17 generally support the mean size and PDI values described in Table 1; for the SN-38-PNP sample, the Gaussian peak position does not match the $d_{h,eff}$ value from cumulant analysis (Table 1), likely due to the non- Gaussian nature of the actual sample distribution. A wide range of experimental studies suggest an optimal size of around 50 nm for efficient uptake of various nanoparticle types in several cell lines[181–183] consistent with a theoretical model of receptor- mediated endocytosis,[184] with the optimal size showing variability with cell type.[182] Based on this information, we compared the size distributions of the three PNP formulations with an assumed size regime of 50-60 nm for optimal cell uptake (Figure 17, shaded green band).

We see that the broad SN-38-PNP (no CUR) sample shows considerable overlap with the 50-60 nm size regime, although this overlap is increased significantly by the size-focusing of CUR addition in the narrow SN-38/CUR_{100}-PNP (high CUR) sample, which may account for its increased potency against A204 cells (Figure 16A, 96 h). On the other hand, the moderate distribution narrowing in the SN-38/CUR_5-PNP (low CUR) sample leads to a PNP population peaked below 50 nm and with minimal overlap with the 50-60 nm size regime, explaining the low potency of this sample compared to the other two PNP formulations (Figure 16A, 96 h). The somewhat different potency trend against U87 cells, with SN-38-PNPs showing higher potency than SN-38/CUR_{100}-PNPs, could be explained by a larger optimal PNP size for cell uptake in U87 cells compared to

A204 cells, with only the broad distribution sample (no CUR) resulting in significant overlap with the optimal size regime of the former cell line. In addition to the size effects described above, differences in PNP potency may also be attributed to changes in the distribution of encapsulated SN-38 throughout the PNP populations with different CUR amounts. For example, the small amount of added CUR within the SN-38/CUR_5-PNP formulation may skew the distribution of encapsulated SN-38 towards PNPs within the population that are less readily taken up by the cells. On the other hand, the plasticizing effect of the larger initial CUR amount in the SN-38/CUR_{100}-PNP formulation should increase chain mobility within the cores, allowing encapsulated SN-38 to distribute more uniformly over the entire PNP population such that more anticancer drug can be taken into the cells. Further experiments are required to elucidate a better mechanistic understanding of the effect of CUR addition on the potency of SN-38/CUR-PNPs, although the current results highlight the importance of formulation chemistry and manufacturing conditions on both the physicochemical and therapeutic properties of multidrug-encapsulated polymer nanomedicines.

2.5 Conclusions

We have shown that nanoprecipitation of PNPs from poly(ε-caprolactone)-*block*-poly(ethylene glycol) (PCL-*b*-PEG) copolymer with combinations of CUR and SN-38 provides a number of advantages for the delivery of the potent anticancer drug SN-38 compared to formulations containing SN-38 alone. For example, SN-38 encapsulation efficiencies were enhanced by up to a factor of 10 by adding varying amounts of co-encapsulated CUR to PNP formulations. We also demonstrated a dramatic decrease in PNP polydispersities, from 0.34 to 0.07, as the initial CUR-to-polymer ratio was increased from $r_{CUR} = 0$ to $r_{CUR} = 10$ at a constant SN-38-to-polymer ratio of

$r_{SN\text{-}38}$ = 0.1, while PNP sizes increased modestly from 40 nm to 55 nm. Comparison of co-loaded PNP formulations using nanoprecipitation in the bulk or in a gas-liquid, two-phase microfluidic reactor resulted in similar trends with respect to CUR content, although improvements in SN-38 encapsulation efficiencies were found using the microfluidic method. Additional precipitation experiments were carried out in the absence of copolymer, showing that CUR increases the dispersion of SN-38 in the solvent medium of PNP formation, which may contribute to the observed encapsulation enhancement. Cytotoxicity studies of unencapsulated SN-38/CUR mixtures showed that CUR did not significantly affect SN-38 potency against either U87 (glioblastoma) or A204 (rhabdomyosarcoma) cell lines. However, we found significant differences in the potencies of PNP formulations depending on initial CUR-to-polymer ratios, with a selected formulation (SN-38/CUR$_{100}$-PNP) showing sub-nanomolar cytotoxicity against A204 cancer cells, significantly more potent than free SN-38 or a SN-38-PNP formulation containing no CUR. Given the numerous recorded health benefits of CUR, together with the improvements to encapsulation efficiencies and polydispersities along with potential cytotoxic benefits described in this study, co-encapsulation with CUR appears to provide an excellent methodology for forming improved polymeric vehicles for SN-38 delivery in cancer patients.

2.6 Acknowledgements

We are grateful to the Natural Sciences and Engineering Research Council of Canada, NSERC (Discovery Grant and CREATE programs), for financial support. We acknowledge Dr. Patrick Nahirney and the UVic EM lab (Department of Biology) for the continued use of their TEM. We also thank Prof. Eugenia Kumacheva and her group for sharing their flow rate analysis software.

3 Chapter 3: The Effect of PEG Terminal End Groups on Physico-Chemical Characteristics of Polymer Nanoparticles Co-Encapsulating SN-38 and Curcumin.

3.1 Contributions

I designed all experiments under the supervision of Prof. Matt Moffitt. Undergraduates Jiawei Tao, Amelie Cazelais, and Trevor Macfarlane contributed to the synthesis and characterization of nanoparticles. PCL-b-PEG-C6 was kindly synthesized and provided to me by Dr. Chuangqi Zhao of the Manners Group.

3.2 Introduction

Surface functionalization or surface modification has become a major area of research in the field of nanomedicine. Surface functionalization of nanoparticles (NPs) is the modification of surface properties of nanoparticles through the conjugation of chemicals or biomolecules. This process aims to improve or add properties useful for NPs in various applications.[185–187]

PEGylation of nanoparticles has long been used to give nanoparticles "stealth" properties, elongating circulation times and avoiding uptake by the reticuloendothelial system (RES).[10,188,189] However, further modifications, often of the PEG itself, allow for finer tuning of the nanoparticles, including crosslinking and active targeting.

Some benefits of surface functionalization include improved biocompatibility and cellular uptake[185], enhanced molecular imaging and multimodal imaging[190]. In theranostics, this imaging function of the nanoparticles is often combined with a drug payload to treat the condition being imaged, particularly cancer. Surface modification can also allow for targeted functionalities,

enabling nanoparticless to target cells of interest with high specificity. Additionally, surface modification can provide improved solubility, biodistribution, and clearance of nanoparticless.

On its own, PEGylation is an important tool for surface functionalization. However, PEG coatings also provide a good starting point for further surface modifications. By modifying the end of the PEG, ligands and antibodies can be added to nanoparticles for active targeting and other benefits. Active targeting has become ever more important as the use of nanomedicine in research has expanded. Nanoparticles tend to naturally accumulate in the liver, and extra-hepatic delivery can be a challenge.[191] In order to overcome this, active targeting can be an essential tool for avoiding the liver and directing nanoparticles to other parts of the body.

PEG polymers typically end in an OH or OCH_3 group. OCH_3 is not reactive and generally does not lend itself to further modification. However, PEG can be modified with a variety of different molecules to make it more amenable to even further modifications. Some of these modifications are so common that they are available "off the shelf" from polymer manufacturers for use in nanomedicine. These include amine modified PEG, carboxylate modified PEG, thiol modified PEG, and maleimide modified PEG. Each of these have different advantages and disadvantages, including changing the size of the endgroups and adding a positive or negative charge. Different endgroups can also change the polarity of the resulting polymer, particularly locally.

In one example, Tian et.al took a maleimide-modified 1,2-distearoyl-sn-glycero-3-phosphoethanolamine-polyethylene glycol (DSPE-PEG) and conjugated it to polyethyleneimine (PEI).[192] The resulting particles showed slow release at pH 7.4, but rapid release at pH 5, which the researchers believe may be a function of PEI dissociating from the nanoparticle and causing dissolution at acidic pH.

In another study, Zhang Y et. al purchased PEG already modified with folic acid on one end and an amine on the other.[193] They further modified the PEG using the amine terminal end to add an ethyl choline phosphate. These modifications when added to their poly(lactic-co-glycolic acid) (PLGA) nanoparticle system, allowed better tumor targeting and tumor killing than un-modified nanoparticle systems.

In yet another study, Zhang L et. al found that modifying PEG with the peptide sequence arginine-glycine-asparagine (RGD) can target nanoparticles to cells expressing integrin, making the nanoparticles more effective at fighting gliomas. RGD has been found to have high affinity with the cell adhesion molecule integrin $\alpha_v\beta_3$, which has a role in cancer progression, and is therefore a useful active targeting agent. [194]

The terminal charge of PEG can also play a significant role in the interaction of nanoparticles with cells and their cytotoxicity,[195] In one study, researchers designed PEG termini ending in either acidic (-COOH) or amino ($-NH_2$) functionalities to study the effect of terminal charge in nanoparticle-biomolecule conjugates.[196] The choice of terminal charge can result in final negative or positive net charges on the nanoparticles, which can affect their interaction with cells.[196]

These studies underscore the potential of PEG modifications in improving the delivery of drugs and genes using nanoparticles.

Functionalizing PEG terminal ends on the corona of a nanoparticle is a common method of adding functionality to it,[197–204] but this requires modification of the end of the PEG to allow for connecting something new to it. While many papers have been published on the functionalization of nanoparticles for various purposes, and many reviews summarize advances in surface modification of nanoparticles and their applications,[185,205,206] there has been relatively little

research on the effect of these PEG terminal endgroups on the physicochemical characteristics of the nanoparticles, including size, polydispersity, and drug loading.

One common reason for functionalizing PEG is to crosslink particles. Prof. Karen Wooley in particular has done extensive research on the effect of crosslinking on release rates, cytotoxicity, immunogenicity, and other characteristics of nanoparticles.[73–76,207] Research in her lab has found that crosslinking can improve many characteristics of nanoparticles.

In this article, we functionalize PEG with some common terminal endgroups and examine the effects on polymer nanoparticles co-encapsulating SN-38 and curcumin.

We tried out a variety of different PEG terminal groups and found distinct effects on the physico-chemical effects of our nanoparticle system. Some end groups increased drug loading, while others reduced drug loading in particles. Size and polydispersity also varied among particles made with different terminal end functionalized PEG groups. We attempted to find a trend to predict which terminal end groups would lead to the best drug loading but found that the factors leading to the effect of terminal end groups on our nanoparticle system are too many and too varied to provide a clear picture of any one factor. Perhaps future research could further elucidate this effect and find clearer trends between different aspects of functionalized PEG terminal end groups and the effects on the nanoparticle system.

For our research we used a polymer nanoparticle system composed of PCL-PEG and loaded with SN-38 and curcumin. This formulation has been established in our lab and was studied in an earlier publication.[62]

We then looked at the same terminal end-groups but in nanoparticles containing only a single compound, either SN-38 or curcumin. We also compared the effects of terminal endgroups in nanoparticles synthesized using bulk nanoprecipitation and using microfluidic nanoprecipitation.

Resulting PNPs were characterized by DLS and HPLC for effective hydrodynamic diameter, polydispersity, and drug encapsulation. The most promising formulation was also compared to our standard methoxy terminated PEG PNP for release kinetics.

By better understanding the effect of terminal end groups of PEG in nanoparticle systems, scientists can choose the best terminal end group for their purposes, forearmed with the knowledge of what effects this choice might have on their nanoparticle systems.

3.3 Experimental Section

3.3.1 Materials

A number of different derivatives of a PCL-*b*-PEG block copolymer were used in this study. PCL-*b*-PEG-OCH_3 (Advanced Polymer Materials) possessed PCL and PEG blocks with number-average molecular weights of M_n = 12 000 and 5000 g/mol, respectively, and overall dispersity of $Đ$ = 1.20. PCL-*b*-PEG-COOH (Advanced Polymer Materials) possessed PCL and PEG blocks with number-average molecular weights of M_n = 5000 and 12600 g/mol, respectively, and overall dispersity of $Đ$ = 1.47, and a functionality of > 85% as determined by NMR. PCL-*b*-PEG-NH_2-TFA (Advanced Polymer Materials) possessed PCL and PEG blocks with number-average molecular weights of M_n = 12100 and 5200 g/mol, respectively, and overall dispersity of $Đ$ = 1.50, and a functionality of >80% as determined by NMR. PCL-*b*-PEG-$(CH_2)_2$-COO-$(CH_2)_2$-SH (Advanced Polymer Materials) possessed PCL and PEG blocks with number-average molecular weights of M_n = 5000 and 12000 g/mol, respectively, and overall dispersity of $Đ$ = 1.47, and a functionality of > 80% as determined by NMR. PCL-*b*-PEG-$(CH_2)_2$-COO-$(CH_2)_2$-S-$(CH_2)_5$-CH_3 was synthesized by Dr. Chuangqi Zhao of the Manners Lab at the University of Victoria from the PCL-*b*-PEG-$(CH_2)_2$-COO-$(CH_2)_2$-SH. Because it was made from this precursor, it possessed also

PCL and PEG blocks with number-average molecular weights of M_n = 5000 and 12000 g/mol, respectively, and overall dispersity of $Đ$ = 1.47, and a functionality of > 80% as determined by NMR for the SH moiety, but with a secondary functionality of 81% for the hexyl group. Multiplying the functionality of the SH group (80%) by the functionality of the hexyl group (85%) yieldS a final functionality of 68%. After drying in vacuum overnight, the product was obtained as a white solid (168 mg, 84%).

SN-38 (≥98.0%) was purchased from Cedarlane Laboratories and CUR (for synthesis) was purchased from MilliporeSigma. NaCl (Bio Basic Canada, 99.9%), KCl (Caledon, 99.0%), Na_2HPO_4 (BioBasic Canada, 98.0%), and KH_2PO_4 (Caledon, 99.0%) were used to prepare phosphate-buffered saline (PBS, pH 7.4). DMF (Caledon, 99.8%) and acetonitrile (Caledon, HPLC-grade) were used as received.

3.3.2 Microfluidic Reactor Fabrication

Negative masters were fabricated on silicon wafers (Silicon Materials) using the negative photoresist SU-8 100 (Kayaku). A 150 μm thick SU-8 film was spin-coated at 2000 rpm onto the silicon wafer and heated at 65 °C for 12 min and then at 95 °C for 50 min. After the wafer was cooled, a photomask was placed directly above, and the wafer was exposed to UV light for 100 s. Then, the UV-treated film was heated at 65 °C for 1 min and then 95 °C for 20 min. Finally, the silicon wafer was submerged in SU-8 developer (Kayaku) and rinsed with isopropanol until all unexposed photoresist was removed.

Microfluidic chips were fabricated from poly(dimethylsiloxane) (PDMS) using a SYLGARD 184 silicon elastomer kit (Dow Corning). For fabrication of all PDMS chips, the elastomer and curing agent were mixed at a 7:1 ratio and degassed under vacuum. The resulting mixture was poured

over a clean negative master chip in a Petri dish and further degassed until all remaining air bubbles were removed. The PDMS was heated at 85 °C until cured (~20 min) and then peeled from the negative master; holes were punched through the reservoirs of the resulting PDMS chip to allow for the insertion of tubing. A thin PDMS film (substrate layer) was also made on a glass slide by spin-coating a 20:1 elastomer/curing agent mixture followed by curing. The substrate layer was then permanently bonded to the base of the microfluidic reactor (channel layer) after both components were exposed to oxygen plasma for 90 s. The resulting reactor (Figure 19 B) has a set channel depth of 150 μm and consists of a sinusoidal mixing channel 100 μm wide and a sinusoidal processing channel 200 μm wide, identical to the reactor described in previous publications from our group.[93,94,120,121,208]

3.3.3 Flow Delivery and Control

Pressure-driven flow of liquids to the reactor inlet was provided using 1 mL gastight syringes (Hamilton, Reno, NV) mounted on syringe pumps (Harvard Apparatus, Holliston, MA). The microfluidic chip was connected to the liquid syringes via 1/16th-inch (OD) Teflon tubing (Scientific Products and Equipment, ON). Argon (Ar) gas flow was introduced to the chip via an Ar tank regulator and a downstream regulator (Johnston Controls) for fine adjustments. The chip was connected to the downstream regulator through a 1/16 i.n. (OD)/100 μm (ID) Teflon tube (Upchurch Scientific, Oak Harbor, WA). The liquid flow rate (Q_{liq}) was programmed via the syringe pumps, and the gas flow rate (Q_{gas}) was fine-tuned via the downstream pressure regulator in order to set the nominal total flow rates (Q) of 50, 100, 200, and 400 μL/min described in the main text. Due to the compressible nature of the gas and the high gas/liquid interfacial tension, discrepancies arise between the nominal (programmed) and actual values of Q_{gas}, Q_{gas}/Q_{liq}, and the

total flow rate (Q_{total}). Therefore, actual values of Q_{gas}, Q_{gas}/ Q_{liq}, and $Q_{total} = Q_{gas} + Q_{liq}$ for each microfluidic experiment (Appendix 3) were calculated from the frequency of bubble formation and the average volume of gas bubbles, determined from image analysis of the mean lengths of liquid and gas plugs, L_{liq} and L_{gas}, respectively, under a given set of flow conditions. Visualization and actual flow rate calculations were done using a modified version of Matlab software originally developed by the Kumacheva lab at the University of Toronto and generously shared with our lab. For all experiments, $Q_{gas}/Q_{liq} \sim 1$; actual Q_{total} values are within 10% of nominal Q values reported in the main text. Images of the microchannels were captured using a Genie Nano-C1280 camera (1stVision) equipped with an On-Semi Python1300 sensor and a C-Mount Manual Iris Varifocal lens (1/1.8 in., 4–13 mm, *f*/1.5, Tamron).

3.3.4 Microfluidic Preparation of SN-38/CUR-Loaded Polymer Nanoparticles (SN-38/CUR-PNPs)

PNPs containing various quantities of SN-38 and CUR were prepared using a microfluidic nanoprecipitation method. For microfluidic preparation of SN-38/CUR-PNPs, the following three fluid streams were combined to form gas-segmented liquid plugs within the reactor (Figure 19): (1) 1.0 wt % PCL-*b*-PEG in DMF containing variable amounts of codissolved SN-38 and CUR, described by the initial drug-to-polymer ratios (*w*/*w*) r_{SN-38} and r_{CUR}, respectively, with r_{SN-38} of either 0 or 0.1 and r_{CUR} of either 0 or 10; (2) pure DMF; and (3) DMF/deionized water. In the case of SH-modified polymer, a 40x molar ratio of NaBH4 to SH was added to the DMF, and the mixture was stirred for 30 minutes before use. This ratio was based on research found in the literature[209], and then optimized with preliminary experiments in our lab. The flow rates of the three liquid streams were equal for all runs such that the steady state on-chip copolymer concentration was 0.33 wt %. The water content of the DMF/water stream was selected to yield a

steady state on-chip water concentration of 15.6 wt %. The critical water content (cwc) of 0.33 wt % PCL-*b*-PEG in DMF was determined to be 5.6 wt % (, Appendix 1), such that the water content for all microfluidic SN-38/CUR-PNP preparations was cwc +10 wt %. This water content was used for all polymer derivatives prepared on chip, for consistency, because they all had similar cwcs (, Appendix 2). For each SN-38/CUR-PNP preparation, the sample was collected from the chip into vials containing 10-fold excess by volume of deionized water. In order to remove residual DMF, the resulting samples were then dialyzed (6–8 kDa MWCO dialysis membrane, Spectrum Laboratories) against deionized water for 18 h, with changing of water every hour for the first 4 h. Precipitated drug in the aqueous samples was removed by centrifugation at 16 000 × *g* for 20 min; the resulting dispersions were designated SN-38/CUR-PNPs.

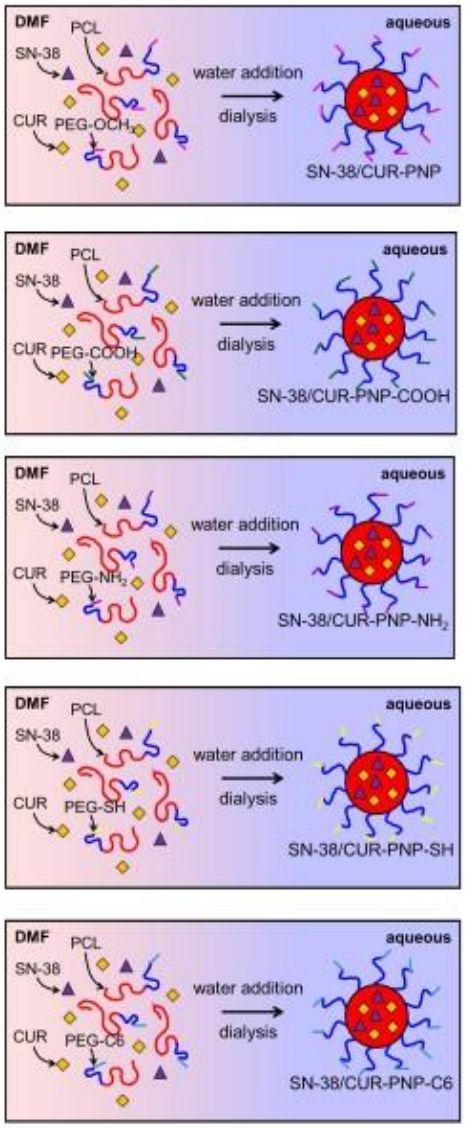

Figure 18. Figure 16. Schematic depicting the different terminal end groups and the resulting nanoparticle. The standard PNP formulation is the methoxy terminated formulation.

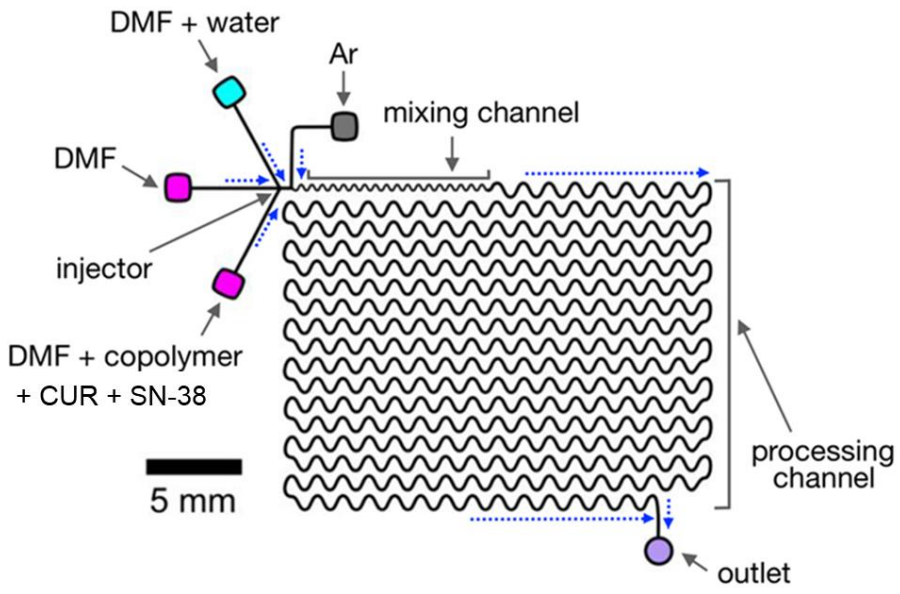

Figure 19. Schematic showing the two-phase gas–liquid microfluidic reactor used in this study

Adapted with permission from Mol. Pharmaceutics 2022, 19, 6, 1866–1881 Publication Date:May 17, 2022 https://doi.org/10.1021/acs.molpharmaceut.2c00005. Copyright 2022 American Chemical Society.

3.3.5 Bulk Preparation of SN-38/CUR-Loaded Polymer Nanoparticles (SN-38/CUR-PNPs)

Selected PNP formulations were also prepared using a bulk nanoprecipitation approach. Specifically, ∼3 g quantities of 0.33 wt % copolymer in DMF containing variable amounts of codissolved SN-38 and CUR, with $r_{SN\text{-}38}$ = 0 or 0.1 and r_{CUR} = 0 or 10, were prepared. The various solutions were stirred overnight, then each solution was added dropwise at a rate of 120 μL/min using a syringe pump into 10× excess volume of deionized water with continuous high-speed stirring. In the case of SH-modified polymer, a 80x molar ratio of $NaBH_4$ to SH was added to the DMF, and the mixture was stirred for 30 minutes before use. This ratio was based on research found in the literature[209], and then optimized with preliminary experiments in our lab. In order to remove residual DMF, the resulting samples were then dialyzed (6–8 kDa MWCO dialysis

membrane, Spectrum Laboratories) against deionized water for 18 h, with changes of water 1 h for the first 4 h. Precipitated drug in the aqueous samples was removed by centrifugation at 16 000 × *g* for 20 min; the resulting dispersions were designated SN-38/CUR-PNPs.

3.3.6 Dynamic Light Scattering

DLS measurements were carried out for determination of hydrodynamic sizes, polydispersities, and size distributions of PNPs. DLS experiments were performed on a Brookhaven Instruments photocorrelation spectrometer equipped with a BI-200SM goniometer, a BI-9000AT digital autocorrelator, and a BI-Mini-L30 30 mW red (636 nm) compact diode laser, at a scattering angle of 90° and a temperature of 25 °C. PNP concentrations for all DLS measurements were ∼0.01 mg/mL. For each PNP dispersion, mean effective hydrodynamic sizes and polydispersities were determined from three measurements of the autocorrelation function using cumulant analysis. Representative intensity-weighted size distributions were determined from CONTIN analysis. Reported mean effective hydrodynamic sizes and polydispersities for each condition were determined by averaging values from triplicate preparations. Standard errors (σ) on hydrodynamic sizes and polydispersities were calculated from the standard deviation (*s*) of triplicate values: $\sigma = s/\sqrt{3}$.

3.3.7 Determination of SN-38 and Curcumin Encapsulation Efficiencies and Drug Loadings

A high-performance liquid chromatograph (HPLC) (Agilent 1100) equipped with an Agilent Eclipse C18, 4.6 mm × 150 mm (5 μm) column and a diode array detector (DAD) set at 265 and 425 nm was used to quantify SN-38 and curcumin concentrations, respectively. The mobile phase consisting of acetonitrile and water (65:35, *v*/*v*) with 0.3 vol % acetic acid was run at 1 mL/min. The column temperature was kept at 25 °C during all measurements. To prepare samples for

HPLC, water was removed from ~2 g of a gravimetrically determined quantity of SN-38/CUR-PNPs by rotary evaporation at 25°C until dryness, followed by addition of a known gravimetrically determined quantity of acetonitrile (~1 g) and overnight sonication to ensure complete dissolution of all solids. Next, 10 μL of the drug/copolymer/acetonitrile solution was injected into the HPLC instrument by an autosampler for analysis of SN-38 and curcumin concentrations. An SN-38 calibration curve was generated using five standards of known concentrations of SN-38 in acetonitrile (1, 3, 5, 10, and 25 ppm). A CUR calibration curve was generated using eight standards of known concentrations of CUR in acetonitrile (1, 3, 5, 10, 25, 50, 100, and 200 ppm).

Encapsulation efficiencies (EE) and drug loadings (DL) of SN-38 and curcumin ($EE_{SN\text{-}38}$, EE_{CUR}, $DL_{SN\text{-}38}$, and DL_{CUR}) for each sample were calculated using the following equations:

$$\text{EE (\%)} = \frac{\text{mass encapsulated drug}}{\text{total mass drug}} \times 100$$

$$r = \frac{\text{total mass drug}}{\text{total mass copolymer}}$$

$$\text{DL} = \frac{\text{mass encapsulated drug}}{\text{total mass copolymer}}$$

$$\text{DL} = (\text{EE}/100) \times r$$

Reported $EE_{SN\text{-}38}$, EE_{CUR}, $DL_{SN\text{-}38}$, and DL_{CUR} values were determined by averaging values from triplicate PNP preparations under the same conditions. Standard errors (σ) on encapsulation efficiencies and drug loadings were calculated from the standard deviation (*s*) of triplicate values: $\sigma = s/\sqrt{3}$.

3.3.8 *In Vitro* Release Kinetics of SN-38/CUR-PNPs

Near-perfect sink conditions were established for *in vitro* release experiments, meaning that the volume of the PBS (pH 7.4, ∼4 L) release medium was sufficiently greater (∼200×) than the sample volume (∼10 mL) so as to approximate the large dilution of drug delivery particles in the human body. These sink conditions ensured that a large concentration gradient was maintained between the particles and the surrounding medium, driving continuous diffusion-controlled drug release. HPLC was used to monitor the SN-38 and CUR release kinetics of SN-38/CUR-PNPs. In a typical experiment, a known mass (∼10 g) of SN-38/CUR-PNP sample was put into a 10 mL Float-A-Lyzer tubes (SpectrumLabs, MWCO 100 kDa). These tubes were then placed, two per beaker, in a 5-L beaker of the release medium, consisting of ∼4 L of PBS; throughout the release experiments, the release medium was constantly stirred using magnetic stirring and maintained at physiological temperature (37 ± 0.2 °C). Then, at each predetermined time (t = 0, 0.5, 1, 2, 4, 8, and 24 h), a gravimetrically determined aliquot (∼1 g) of the larger sample was transferred from the Float-A-Lyzer tube to a vial and dried by rotary evaporation at 25 °C. A gravimetrically determined quantity of acetonitrile (∼0.5 g) was then added to the dried aliquot followed by overnight sonication to ensure complete dissolution of all solids. The concentrations of SN-38 and CUR were then determined by HPLC as described in the previous section; percentages of SN-38 and CUR released were calculated relative to the t = 0 h release time. Reported release percentages at each time point were determined by averaging values from triplicate PNP preparations under the same conditions. Standard errors (σ) on release percentages were calculated from the standard deviation (s) of triplicate values: $\sigma = s/\sqrt{3}$.

The release profiles were fit using the Levenberg–Marquardt algorithm within OriginLab, and mean release half times were extrapolated from the fits; experimental errors on half time vales were determined based on the quality of the fits. The following fitting model was used for all conditions:

$$Y = 1/B*\{\ln(A*B*x+1)\}$$

3.4 Results and Discussion

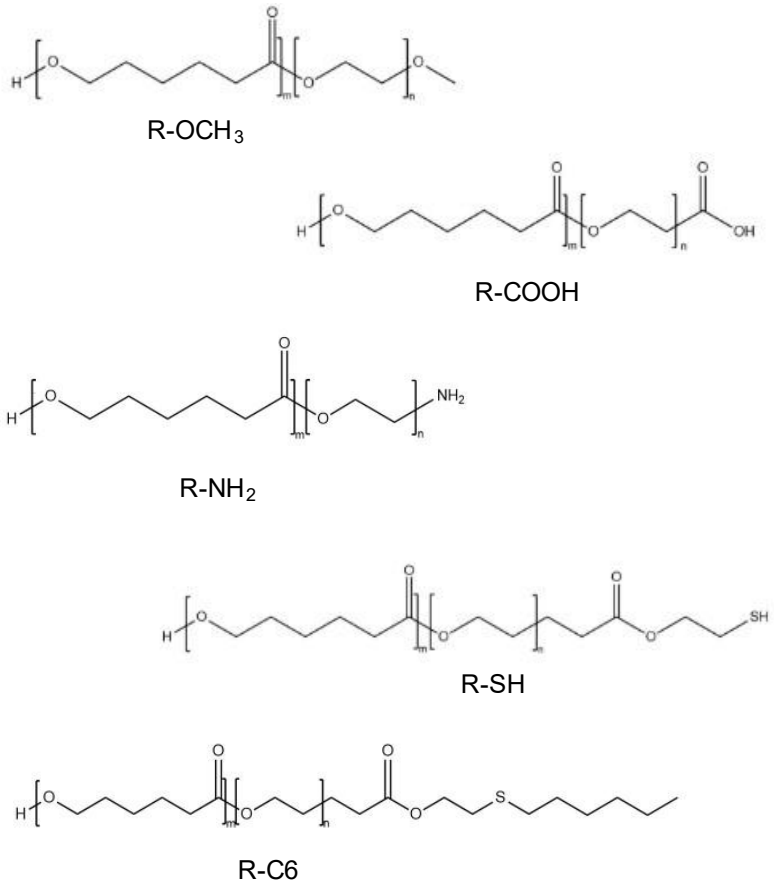

Figure 20. Molecular structures of each polymer and end group used in the study

3.4.1 Effect of PEG terminal end groups on SN-38 and CUR encapsulation of SN-38/CUR-PNPs, CUR-PNPs, and SN-38-PNPs prepared by bulk nanoprecipitation.

In order to investigate the effect of PEG terminal end groups on drug encapsulation of SN-38/CUR_{100}-PNPs, we synthesized PNPs using PCL(12k)-b-PEG(5k) block co-polymer, where the

terminus of the PEG was altered slightly in each variation of polymer, (Figure 20). The terminal end groups attached to the PEG were named OCH_3, COOH, NH_2, SH, and C6, again, see Figure 20. This variety of end groups added a number of different qualities to the end of the PEG of the PNPs. At neutral pH such as is used for our synthesis of PNPs, COO^- is negatively charged, NH_3^+ is positively charged, and OCH_3, SH, and C6 are neutral. SH and C6 are longer than the other end groups. The polarity of each end group is also different, with COOH the most polar and C6 the least polar. All these differences can be expected to affect the physico-chemical characteristics of the resulting PNPs, including drug loading. One hypothesis we tested is that the polarity of the PEG end group would affect the drug encapsulation, particularly of SN-38, due to its hydrophobicity. This trend did hold for SN-38/CUR_{100}-PNP-COOH, SN-38/CUR_{100}-PNP-NH_2, SN-38/CUR_{100}-PNP, and SN-38/CUR_{100}-PNP-SH as prepared in the bulk, see Figure 22, but the trend broke with SN-38/CUR_{100}-PNP-C6, which showed significantly lower encapsulation of SN-38 than did SN-38/CUR_{100}-PNP-SH (21 % ± 2 % for SN-38/CUR_{100}-PNP-SH, and 15 % ± 1% for SN-38/CUR_{100}-PNP-C6.) SN-38/CUR_{100}-PNP-SH showed the best SN-38 encapsulation, more than a two-fold increase over our reference standard of SN-38/CUR_{100}-PNPs. SN-38/CUR_{100}-PNP-OCH_3, are used as the reference standard throughout this chapter as it is the PEG terminal end group used in our research group for the synthesis of PNPs up until we decided to explore other options, and was used in the synthesis of our PNPs in our previous publication.[62] One possibility for the polarity trend breaking for SN-38/CUR_{100}-PNP-C6 is that this end group is significantly bulkier than the other end groups and may have sterically hindered drug from entering the PNP. Another possibility is that the reactivity of the S on the SH group had some kind of beneficial effect on the drug encapsulation separate from the effect of the end group being less polar. SN-38/CUR_{100}-PNP-C6 does show higher encapsulation of SN-38 than any formulation with the

exception of SN-38/CUR_{100}-PNP-SH. In the presence of a reducing agent such as the $NaBH_4$ used in the synthesis of the SN-38/CUR_{100}-PNP-SH, the S would be available as an H donor for hydrogen bonding, which may have had some effect on drug loading. Another possibility for the lower SN-38 encapsulation in SN-38/CUR_{100}-PNP-C6 is that the dramatically reduced polarity of the C6 end group could have caused a misalignment of the polymer during self assembly, with an occasional PEG hydrophobic terminal group pushing small quantities of PEG into the hydrophobic PCL core. This would have two effects. One, the bulky PEG group would take up space that could then not be occupied by drug in the core, and also, the PEG itself would make the core less hydrophobic, making it a less favorable environment for the hydrophobic drug. All of these are interesting possibilities that merit further investigation if we wish to fully understand the effect of PEG terminal end groups on drug encapsulation.

Another interesting effect that can be seen in Figure 23 if we compare across the two groups of results displayed, is that while significant differences can be seen in SN-38 drug loading in SN-38/CUR-PNPs depending on which PEG terminal end group is used, these differences disappear in SN-38-PNPs, which do not contain curcumin. One possible explanation for this is that, as posited in our previous paper,[62] there is an interaction between CUR and SN-38 that slightly reduces the hydrophobicity of SN-38 and allows it to stay in aqueous solution slightly longer. This gives it time to partition into the hydrophobic core of the PNP, and in this way the drug loading can benefit from effects of the PEG terminal end group. In SN-38-PNPs, SN-38 is alone, and the fact that it is more hydrophobic than the polymer means that it likely aggregates and falls out of solution before the PNPs self-assemble, as has been shown by another group doing similar research.[167] This prevents the SN-38 from partitioning into the hydrophobic core of the particle

under any circumstances, and thus differences in the effect of the PEG terminal end group cannot be seen.

When we look at CUR encapsulation in all forms of SN-38/CUR_{100}-PNPs (Figure 21), we see a similar situation to that of SN-38 encapsulation, where a trend of drug encapsulation following polarity is seen in the four formulations until SN-38/CUR_{100}-PNP-C6, when the trend breaks. This is perhaps due to the same reasons postulated above for the potential reasons for this break in the trend of SN-38 encapsulation. Curcumin is also hydrophobic, although not as highly hydrophobic as SN-38, and may also benefit from a less polar PEG terminal end group. A difference in the effect seen with SN-38 and that seen with CUR in the SN-38/CUR_{100}-PNP blends, is that SN-38 encapsulation in SN-38/CUR_{100}-PNP-C6 is higher than the reference SN-38/CUR_{100}-PNP or any of the others except for SN-38/CUR_{100}-PNP-SH. In the case of CUR encapsulation, SN-38/CUR_{100}-PNP-C6 shows lower encapsulation not just than SN-38/CUR_{100}-PNP-SH, but also than the SN-38/CUR_{100}-PNP, a small but statistically significant reduction. Perhaps, due to the weaker hydrophobicity of CUR, it is less affected by the polarity of the PEG terminal end group and therefore relatively more affected by the other considerations mentioned above for reasons SN-38/CUR_{100}-PNP-C6 might have less drug encapsulation than expected.

In Figure 21, as in Figure 22, we see that there are statistically significant differences of CUR encapsulation when PNPs are made with a SN-38/CUR blend, but when CUR-PNPs are made, with no SN-38, there are no significant differences between different PEG terminal end groups in drug encapsulation. The explanation here seems less straightforward than for SN-38, as CUR does remain in solution during the spontaneous assembly of PNPs and is thus available to partition into the hydrophobic core of the PNP. Perhaps, with its lower hydrophobicity, CUR on its own is not subject to the effect of polarity of PEG terminal end groups. However, when SN-38 is present, and

CUR and SN-38 associate with each other, the effect of the PEG terminal end group on SN-38 encapsulation is transferred to the associated CUR as well. This would explain a certain change in CUR that is directly associated to the SN-38 but given that far more CUR than SN-38 is incorporated into the particles, this does not explain the entire phenomenon.

It should be noted that the different SN-38/CUR_{100}-PNPs, as noted, have an excess of CUR far beyond what can be encapsulated in the PNP. This initial drug ratio was chosen because of the effect of CUR on the polydispersity of particles and the increased cytotoxicity of PNPs made with such an excess of CUR, as discussed in our previous work.[62] These reasons led us to choose a 100x fold greater CUR initial concentration than SN-38, but it may be that differences in CUR loading would be more easily seen with a lower initial drug ratio. However, since the focus of this chapter was the effect on the chemotherapeutic drug SN-38 rather than the CUR excipient, it was logical to continue with the initial drug ratio of CUR that made the most sense for the resulting particles, rather than optimizing the experiments to see changes in CUR drug encapsulation.

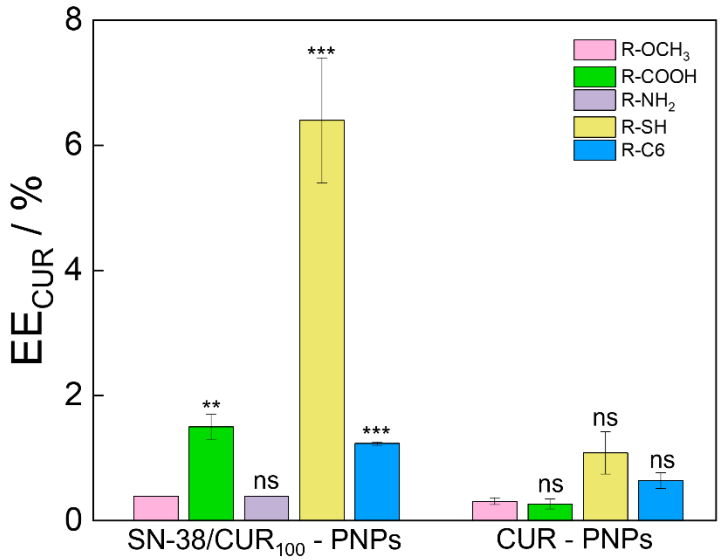

Figure 21. Encapsulation efficiency of CUR in PNPs with different PEG- terminal end groups, prepared with only one drug or the other, or a blend of both.

R-OCH$_3$ is the standard PNP from previous chapters, against which the new formulations were prepared. Statistical signicance was determined using a two tailed T-test, with p<0.05 considered to be significant. (; p < 0.05) (**, p < 0.01) (***, p < 0.001)*

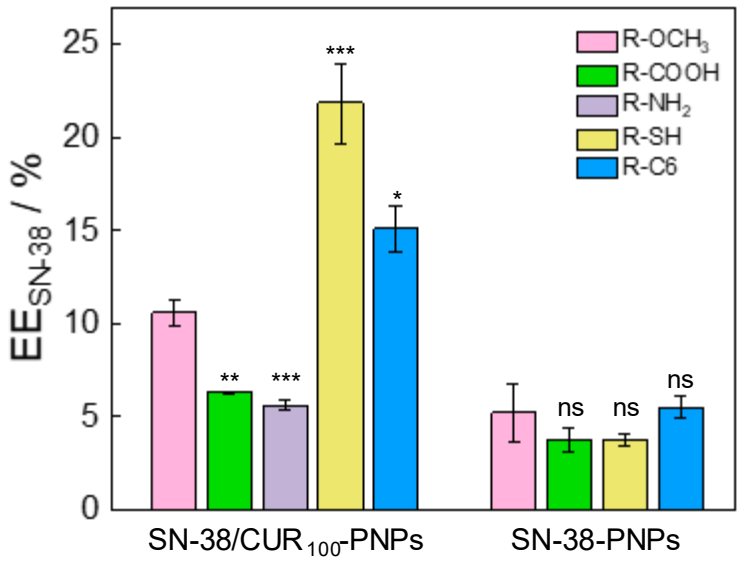

Figure 22. Encapsulation efficiency of SN-38 in PNPs with different PEG- terminal end groups, prepared with only one drug or the other, or a blend of both

All PNPs prepared using bulk nanoprecipitation.

3.4.2 Effect of PEG terminal end groups on effective hydrodynamic diameter and polydispersity of SN-38/CUR$_{100}$-PNPs, CUR-PNPs, and SN-38-PNPs prepared by bulk nanoprecipitation.

The hydrodynamic size of PNPs prepared using different PEG terminal end groups does not vary greatly, with a range of only 40 to 100 nm. That being said, there are statistically significant differences seen in sizes of different preparations, see Figure 24. These do not follow any trend of polarity of PEG terminal end groups, such as can be seen in the drug encapsulation data shown in Figure 22 and Figure 23. Not surprisingly, SN-38-PNPs show the greatest variation in size and CUR-PNPs show no significant differences in size. CUR has been shown in our previous work to act as

a plasticizer and results in consistent particles.[62,208] This effect of CUR in excess may be stronger than any effect of PEG terminal end group on the size of CUR-PNPs. Changes are therefore more likely to be seen in PNPs that do not contain CUR. One surprising result is the SN-38/CUR_{100}-PNP-SH as contrasted with the SN-38-PNP-SH. In the SN-38/CUR-PNPs, SN-38/CUR_{100}-PNP-SH show a significantly smaller size than the other PNPs, which are all fairly similar to each other. This points to a possible crosslinking effect of the thiol groups when exposed to water for 18 hours during dialysis, leading to smaller particles. However, this effect is not seen in the SN-38-PNPs, and in fact the SN-38-PNP-SH show the largest particles. This result is unexpected and merits further investigation. That the other two SN-38-PNPs, SN-38-PNP-COOH and SN-38-PNP-C6, in comparison with our reference of SN38-PNP, are somewhat bigger in size, is less surprising. COOH would be ionized at neutral pH, and this charge could well effect the size of the resulting PNPs. Perhaps the negative charge on the terminal PEG end group causes repulsion between PEG chains and pushes them apart a little, causing a larger particle. One potential reason the SN-38-PNP-SH could show a larger average size is a certain amount of crosslinking between, rather than within, particles, creating aggregates that elevate the average size. This is definitely possible, but it remains to be further understood why this would happen with SN-38-PNP-SH and not SN-38/CUR-PNP-SH. Perhaps the excess of curcumin in the mixture during PNP formation shielded the PNPs from each other and prevented inter-PNP crosslinking, while the lack of shielding in the absence of CUR did lead to inter-particle crosslinking. Further experimentation would be required to elucidate these hypotheses and while they merit further study, they are beyond the scope of this specific project.

The effect of PEG terminal end group on the resulting PNP polydispersity also does not follow the polarity trend seen in drug encapsulation (Figure 25). There are a few interesting differences in

polydispersity within the group of variables that bear further discussion. The first effect that stands out is between the reference SN-38-PNP and the other groups in SN-38-PNPs. Our previous research has also shown that SN-38-PNPs with OCH_3 PEG terminal group show relatively high polydispersity, around 0.33.[62] This result is repeated here, but surprisingly, seems limited to the OCH_3 terminal end group, as all the other group PNPs show lower polydispersity, closer to 0.2 This result is difficult to understand. As OCH_3 is not reactive, it seems confusing that it would lead to a higher polydispersity than charged or potentially reactive terminal end groups. However, while this result is somewhat difficult to interpret, it is still important, as 0.3 for polymer nanoparticles is typically regarded as too polydisperse for clinical use, while 0.2 is generally considered within the window of acceptable polydispersity.[182] This result of SN-38-PNPs demonstrates that by changing the PEG terminal end group, the polydispersity of the resulting PNPs can be reduced.

Also, with regards to polydispersity, SH terminated PEG shows some unexpected results. In comparison with the reference of OCH_3, SN-38/CUR_{100}-PNP-SH shows no significant different in polydispersity, SN-38-PNP-SH shows lower polydispersity, and CUR-PNP-SH shows higher polydispersity. The result in SN-38-PNPs may have more to do with the OCH_3 end group than the SH end group, as the SH end group shows similar results to all end groups other than OCH_3. This effect appears to be mitigated by the presence of CUR, as we do not see the same effect in either CUR-PNPs or SN-38/CUR_{100}-PNPs. The question of why CUR-PNP-SH have a higher polydispersity than the reference CUR-PNPs, while SN-38/CUR_{100}-PNP-SH polydispersity is not significantly different than the reference of SN-38/CUR_{100}-PNP is puzzling. In general, there seems to be an interaction within the three-way mixture of SH PEG terminal group endings, SN-38 and CUR all together that creates a different effect than any of these two parameters alone. What exactly is the nature of this interaction is a topic for further exploration.

If indeed the hydrophobic C6 terminal end group is causing the occasional misplacement of the PEG inside the PNP core, this would explain why the polydispersity of C6 PEG terminated PNPs show higher polydispersity than the reference OCH_3 PNPs, as can be seen in both SN-38/CUR-PNP and CUR-PNP groupings in Figure 21. SN-38-PNP-C6 shows lower polydispersity than the SN-38-PNP-OCH_3 reference. However, this may be more of an effect of the polydispersity of SN-38-PNP being high than the polydispersity of SN-38-PNP-C6 being low.

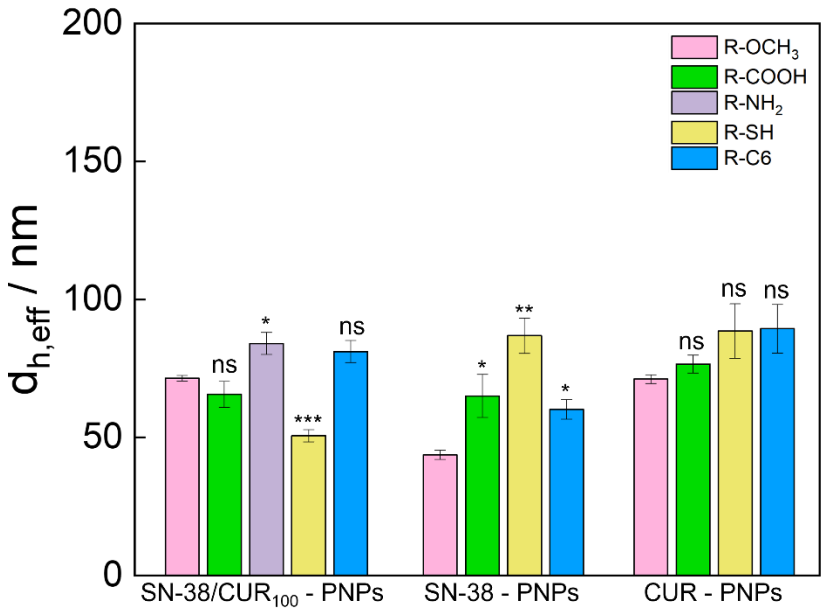

Figure 23. Effective hydrodynamic diameter of PNPs with different PEG-terminal end groups prepared with either CUR, SN-38, or a blend of both.

All PNPs prepared using bulk nanoprecipitation.

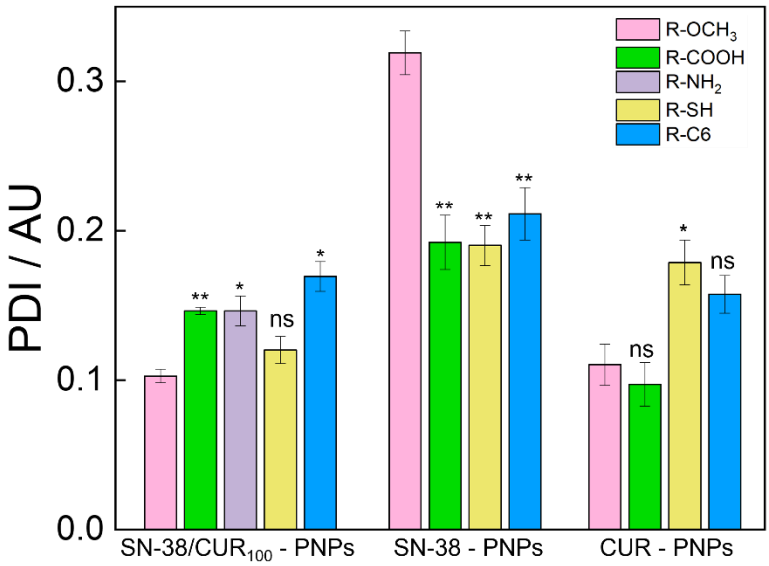

Figure 24. Polydispersity of PNPs with diffeerent PEG-terminal end groups prepared with either CUR, SN-38, or a blend of both.

All PNPs prepared using bulk nanoprecipitation.

3.4.3 Comparison of chip and bulk nanoprecipitation methods for SN-38/CUR-PNPs with varying PEG-terminal end groups

SN-38/CUR-PNPs with different PEG-terminal end groups were synthesized using both bulk and microfluidic nanoprecipitation, and their physico-chemical characteristics were compared. Encapsulation efficiency results, especially for SN-38, were unexpected and quite surprising. In contrast to previous work with exclusively the OCH_3 end group presented in chapter 2, where microfluidic preparation increased drug encapsulation efficiency, in this study, SN-38 encapsulation efficiency decreased significantly in every end group when synthesized on chip, as can be seen in Figure 26. Despite this, trends of encapsulation efficiency from one end group to another were preserved between bulk and chip preparation, indicating that the effect of the end group on drug encapsulation is still important, independent of the method of nanoprecipitation.

While the reduction in drug encapsulation in the methoxy-terminated reference PNPs is statistically significant, it is still quite small, and smaller than the differences seen in other formulations, and may simply be an artifact of variation between batches of the same formulation, especially given the results seen in Chapter 2. The other formulations are either more reactive (amine and carboxyl) or bulkier (thiol and C6) than our reference methoxy formulation, and perhaps these properties cause them to react differently to the shear forces on the chip than we have been accustomed to seeing with all our methoxy formulations used previously. For all that we often see in our research group increased drug encapsulation in our lab using microfluidic reactors [62,208] we also often see the opposite.[94,120] We have yet to publish a study on the mechanism of action responsible for the differences in encapsulation efficiency. One likely hypothesis is that more rapid mixing allows better incorporation of drug into the cores of the PNPs, and why that would be different for different PEG-terminal end groups is not immediately clear. This hypothesis also only goes so far however, as faster flow rates and higher shear forces to do not always give the highest drug encapsulation results.[62,93,120] Given the unexpected results presented here, perhaps a more thorough investigation into the mechanism of shear-force-induced changes in PNP drug encapsulation are warranted, across different polymers, polymer end groups, microfluidic flow rates, and drugs.

It is also unclear why this phenomenon is so much more pronounced with SN-38 than with CUR. With CUR encapsulation, as can be seen also in Figure 26, there was generally no significant different in drug encapsulation between chip and bulk synthesis methods, with the exception of the methoxy end group, which showed better encapsulation on chip, and the thiol end group, which showed better encapsulation in the bulk. As with some other trends explored above, one confounding factor here is the high initial concentration of CUR used in the preparations. Also in

chapter 2, we saw that the effects of the chip were less pronounced as CUR concentrations increased. It is particularly interesting that even with two hydrophobic drugs and identical polymer compositions, differences are seen in encapsulation efficiency trends when bulk and microfluidic nanoprecipitation are compared. Given the other trends we have seen with this drug mixture behaving very differently than individual drugs alone, a first step for further research in this direction would be to duplicate the bulk experiments done with SN-38 alone and CUR alone on chip, to see if the trends seen in the mixture still hold.

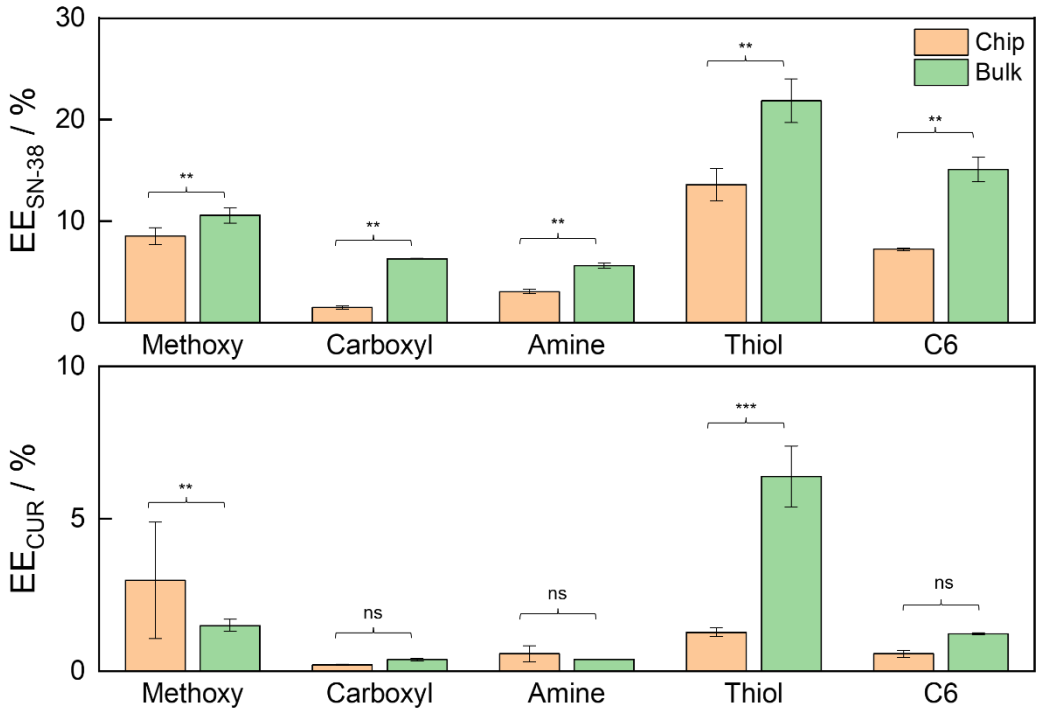

Figure 25. SN-38 encapsulation efficiencies

(Upper) SN-38 encapsulation efficiencies of SN-38/CUR PNPs with different PEG terminal end groups. (Lower) SN-38 encapsulation efficiencies of SN-38/CUR PNPs with different PEG terminal end groups

3.4.4 Effect of select PEG terminal end groups and cross-linking on release kinetics of SN-38/CUR-PNPs prepared by bulk nanoprecipitation.

The most promising formulation, that of SN-38/CUR_{100}-PNP-SH, prepared in the bulk, was tested for release kinetics as compared to the reference polymer, SN-38/CUR_{100}-PNP-OCH_3. Both samples showed somewhat of a burst release (Figure 27, with time to 50% drug release showing no significant difference between the two preparations (Figure 26) and both formulations showing 50% release of drug before 2.5 hours. However, one other point to note about the drug release is that after 24 hours, full drug release was not reached, but rather less than 85% of drug release. This indicates some drug remains in the PNPs for over 24 hours.

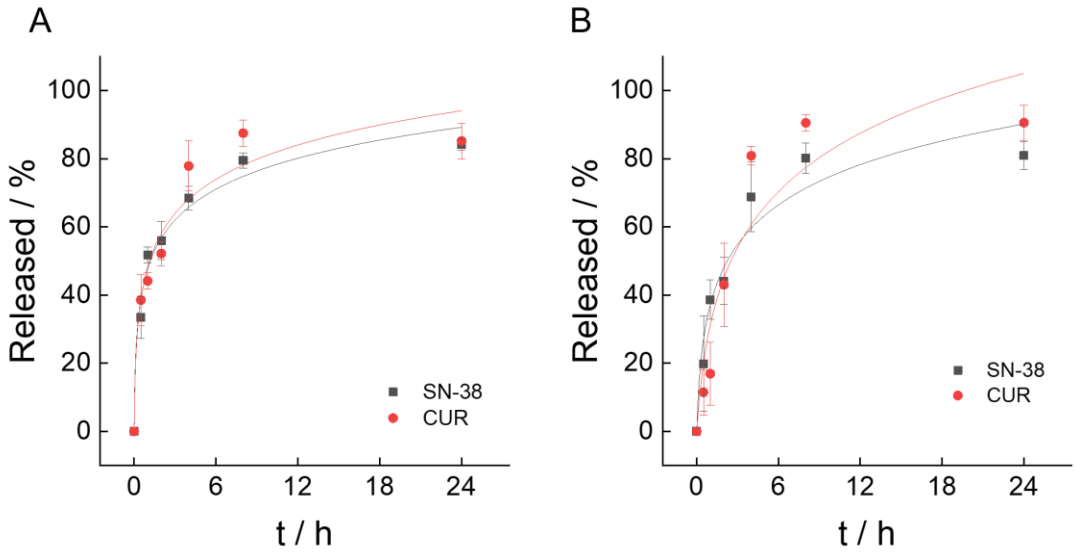

Figure 26. Release kinetics of two PNP formulations

Release kinetics of two PNP formulations, SN-38/CUR-PNP-OCH_3 (A) and SN-38-PNP-SH (B).

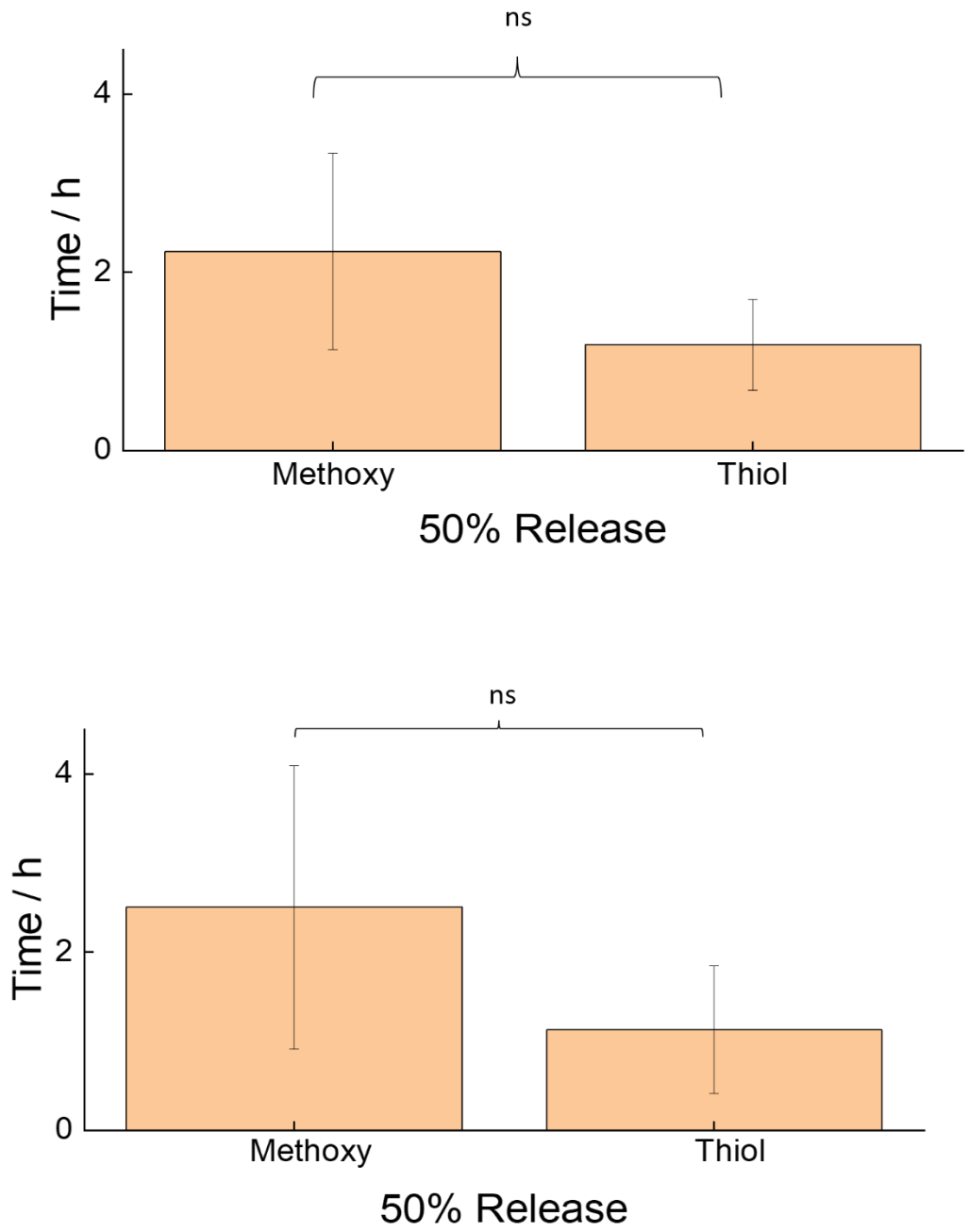

Figure 27. A comparison of the half times of release for the two formulations, for each drug, SN-38(upper) and CUR (lower).

3.5 Conclusions

We prepared polymer nanoparticles containing a blend of SN-38 and CUR, SN-38 alone, or CUR alone, using PCL(12K)-b-PEG(5K) block copolymer with one of a variety of small end groups at the terminal end of the PEG corona. We found that changing the terminal end group has an effect on size, polydispersity, and most significantly, drug encapsulation of the particles, but this effect on drug encapsulation was only seen when SN-38 and CUR were both present in the particles. The effect appeared to show increasing drug encapsulation with decreasing polarity of the end group, but this was trend was broken with the most non-polar end group, SN-38/CUR-PNP-C6, which showed lower encapsulation than that of SN-38-CUR-PNP-SH. These findings represent important information about the effect of polymer composition, specifically terminal PEG end groups, on PNP physico-chemical characteristics, even before any crosslinking or further modifications are performed.

4 Chapter 4: The effect of selected formulations of SN-38/CUR-PNPs on 2-dimensional and 3-dimensional cell culture models

4.1 Contributions

I designed all experiments with the assistance of Prof. Matt Moffitt, Prof. Jeremy Wulff and Prof. Mohsen Akbari. Cell culture was carried out under my supervision by Brookelyn White and Emma Martin, both of whom also participated in EC_{50} experiments. Jiawei Tao contributed to the synthesis and characterization of the particles used in the cell experiments. Confocal microscopy was performed by Dr. Stanislav Konorov, resulting in the images shown in Figure 7. Dr. Amir Seyfoori, of the Akibari lab, kindly provided us with the tumor cell spheroids used in all 3-dimensional cell experiments. Carter Castor, of Indiana University East, fitted the EC_{50} curves and determined the resulting EC50 values and errors, providing the data for Figure 29 to Figure 31, and the curves shown in Appendix 4.

4.2 Introduction

Chemotherapy drugs are widely used in the treatment of cancer, but their efficacy can vary depending on the cell culture model used for testing. Two-dimensional (2D) cell culture systems, which are commonly used, have limitations in fully incorporating the in vivo environment.[210] In contrast, three-dimensional (3D) cell culture systems provide a more physiologically relevant model that better mimics the in vivo conditions.[211]

All efforts of in-vitro testing are aimed at simplifying but replicating the effects of disease and medication in-vivo. 2D and 3D cell cultures both try to accomplish this, and while 3D cell culture clearly better mimics life, which is undeniably three-dimensional, one unavoidable advantage of

2D cell culture is its simplicity and ease of use. Cells are grown as a monolayer on a flat surface, allowing for straightforward experimental manipulation and analysis.[211] This simplicity also enables high-throughput screening of large compound libraries.[212] Additionally, 2D cell culture systems are cost-effective and require less time and resources compared to 3D models.[212] Another advantage of 2D cell culture is the ability to study cell behavior and drug responses in a controlled environment. The absence of complex cell-cell and cell-matrix interactions in 2D culture allows for a clearer understanding of the direct effects of chemotherapy drugs on cancer cells.[212] Moreover, 2D culture systems provide a platform for studying specific cellular processes, such as cell proliferation and gene expression, in a simplified manner.[212]

Despite its advantages, 2D cell culture has several limitations. One major disadvantage is the lack of physiological relevance. Cells grown in 2D culture do not fully recapitulate the complex three-dimensional architecture and microenvironment of tumors in vivo.[211] This discrepancy can lead to differences in drug efficacy between in vitro and in vivo settings.[211] Furthermore, cells grown in 2D culture may exhibit altered cell surface receptor expression and proliferation rates compared to their 3D counterparts. [211] Another limitation of 2D cell culture is the absence of cell-cell and cell-matrix interactions that play crucial roles in drug responses. In 2D culture, cells are not exposed to the same spatial constraints and signaling cues as they would be in a 3D environment.[212] This can result in altered drug sensitivity and resistance, as well as differences in drug distribution within the cell population.[212]

In contrast to 2D cell culture, 3D cell culture systems offer several advantages for investigating chemotherapy drugs. One major advantage is the ability to mimic the complex architecture and microenvironment of tumors in vivo.[211] Cells grown in 3D culture form spheroids or multicellular aggregates that better represent the physiological conditions of tumors.[211] This allows for the study

of cell-cell and cell-matrix interactions, which are critical for drug responses.[213] Furthermore, 3D cell culture systems provide a more accurate representation of drug penetration and distribution within the tumor mass. The presence of extracellular matrix components in 3D culture can create barriers that limit drug diffusion and penetration.[211] This can result in reduced drug efficacy compared to 2D culture, reflecting the challenges faced in clinical settings.[211] Additionally, 3D cell culture systems can better capture the heterogeneity of tumors. Tumors are composed of various cell types with distinct characteristics, and 3D culture allows for the co-culture of different cell types to better mimic the tumor microenvironment.[214] This enables the investigation of drug responses in a more physiologically relevant context.

Despite its advantages, 3D cell culture also has limitations. One major disadvantage is the increased complexity and technical challenges associated with culturing cells in a 3D environment.[215] The use of specialized scaffolds or matrices is often required to support the growth and organization of cells in 3D culture .[215] This can introduce additional variables and potential artifacts that may affect drug responses. Another limitation of 3D cell culture is the difficulty in performing high-throughput screening compared to 2D culture. The complex nature of 3D culture systems makes it more challenging to automate and analyze large compound libraries.[212] This can limit the scalability and efficiency of drug screening in 3D models. Because of this, there may be a place for simplified and streamlined 3D models that, while less complex than true in-vivo experiments, or more complex models involving microfluidics or cell co-culturing, still give more realistic results that 2D culture alone can.

Both 2D and 3D cell culture systems have advantages and disadvantages for investigating chemotherapy drugs. 2D culture offers simplicity, ease of use, and the ability to study specific cellular processes. However, it lacks physiological relevance and the ability to capture the complex

architecture and microenvironment of tumors. On the other hand, 3D culture provides a more physiologically relevant model that better mimics the in vivo conditions. It allows for the study of cell-cell and cell-matrix interactions, as well as drug penetration and distribution within the tumor mass. However, 3D culture is more complex and challenging to implement, and high-throughput screening can be more difficult compared to 2D culture. Overall, the choice between 2D and 3D cell culture systems for investigating chemotherapy drugs should be based on the specific research objectives and the need for physiological relevance and complexity.

In the study performed in this thesis, the tumor spheroid model used was developed by Amir Seyfoori in the Akbari group at the University of Victoria, in collaboration with the company founded by Dr. Seyfoori, Apricell Biotechnology, Inc, and to whom the licensed technology is proprietary. In his article,[216] Dr. Seyfoori discusses the development and application of self-filling microwell arrays (SFMAs) for the formation of tumor spheroids. Tumor spheroids are three-dimensional (3D) cell culture models that better mimic the in-vivo tumor microenvironment compared to traditional two-dimensional (2D) cell culture systems. The SFMAs provide a unique approach to generate uniform and scalable tumor spheroids, addressing some of the limitations of other forms of 3D cell culture[216], including lack of standardization and widespread adoption,[217] insufficient vascularization,[218] technical challenge and complexity,[217] limited scalability,[217] variability in cell culture conditions,[218] differences in drug responses,[219] limited understanding of complex cell-cell interactions[218], and challenges in imaging and analysis.[217] While Dr. Seyfoori's technology does not address all of these limitations, his innovation represents an advance in many of the drawbacks currently plaguing 3D cell culture models.

The most commonly used microwell arrays can only support a limited number of spheroids per well in a culture plate.[220] This limitation hinders high-throughput screening and scalability. In

contrast, SFMAs offer the advantage of higher density culture, allowing for the formation of a larger number of spheroids in a single well.[220] In our case, we were able to use 12 wells in a 48 well plate format. This scalability is achieved by the self-filling mechanism of the microwells, which enables the efficient distribution of cells and media throughout the array. One key differentiating factor of SFMAs from other forms of 3D cell culture is the oxygen permeability of the microwell device. Traditional microwell arrays are anchored in non-oxygen-permeable culture plates, leading to limited oxygen supply for avascular spheroids.[220] In contrast, SFMAs are designed with an oxygen-permeable microwell device, allowing for improved oxygen diffusion and better mimicking the physiological oxygen levels found in tumors.[220] This oxygen permeability is crucial for maintaining the viability and functionality of the tumor spheroids. SFMAs also have advantages in terms of reproducibility and ease of use. The microwell arrays are fabricated using microfabrication techniques, ensuring precise control over the size and shape of the microwells.[221] This enables the formation of uniform spheroids with consistent characteristics, which is essential for reliable and reproducible experimental results. Additionally, the self-filling mechanism simplifies the process of cell seeding and media exchange, reducing the labor and time required for spheroid formation.[220]

SFMAs have been successfully applied in various studies for drug evaluation. In one study, Paolillo et al. (2021)[222] used SFMAs to screen new potential anticancer compounds and evaluate personalized treatment options for glioblastoma multiforme (GBM). The authors highlighted SFMAs as an innovative approach for drug screening in GBM. In another study, He et al. (2022)[220] developed an oxygen-permeable microwell device using SFMAs for the formation of highly viable and functional hepatocellular carcinoma (HCC) spheroids. This device was used for anti-tumor drug evaluation, including the assessment of doxorubicin efficacy. Somewhat earlier, Breslin &

O'Driscoll [223] compared the drug sensitivity and resistance of breast cancer cells in 2D monolayer culture and 3D SFMAs. They found that 3D SFMAs provided a more physiologically relevant model for evaluating breast cancer drug sensitivity and resistance, including the assessment of neratinib efficacy. Additionally, Casey et al. [224] utilized SFMAs as a tumor microenvironment model to study breast cancer growth. They demonstrated the formation of breast cancer spheroids in SFMAs and investigated their response to different growth factors and drugs. Finally, Mirab et al. [225] employed agarose hydrogel microwells fabricated by soft lithography, similar to SFMAs, for the preparation of glioma spheroids with uniform size and morphology. These spheroids were used for drug testing and evaluation.

SFMAs have great potential for anti-tumor drug screening, as the uniform and scalable spheroids generated in the microwell arrays provide a more physiologically relevant model for drug testing.[220] The present study aimed to make use of this potential for the screening of SN-38 PNPs in different formulations. The improved oxygen supply in SFMAs also allows for the evaluation of drug efficacy under conditions that better mimic the tumor microenvironment.[220] SFMAs offer several advantages over traditional microwell arrays and other forms of 3D cell culture. The scalability, oxygen permeability, reproducibility, and ease of use make SFMAs a promising tool for studying tumor biology and evaluating the efficacy of anti-tumor drugs. The application of SFMAs in drug screening can provide more reliable and predictive data, contributing to the development of more effective cancer therapies.

SFMAs are bioprinted. Bioprinting represents a promising new direction for the creation of 3D cell culture tumor models, as has been investigated in the Akbari lab at the University of Victoria. There is a need for biomimetic human tissue models that can accurately represent the pathophysiological conditions involved in disease initiation and progression.[226] The limitations of

conventional 2D in-vitro assays and animal models in fully recapitulating the complex characteristics of human physiology are significant.[226] In contrast, 3D tissue models have the potential to overcome these limitations by providing a more physiologically relevant environment.[226] However, traditional methods of developing 3D tissue models are often low-throughput and lack native-like architecture.[226] The emergence of bioprinting technologies has revolutionized the field by enabling the creation of 3D tissue models with precise control over the arrangement of biomaterials and the incorporation of patient-derived cells.[226] Bioprinting involves the layer-by-layer deposition of bioinks, which are composed of living cells and biomaterials, to create complex 3D structures that mimic the native tissue architecture.[226] There have been many advancements in bioprinting techniques, such as the use of multiple bioinks, vascularization strategies, and integration of functional components.[226] Furthermore, the development of bioprinted tissue models has contributed to our understanding of disease characteristics, including disease initiation and progression.[226] These models have been used to study various diseases, such as cancer, cardiovascular diseases, and neurodegenerative disorders.[226] Bioprinted tissue models offer the advantage of providing a more accurate representation of the disease microenvironment, allowing for better investigation of disease mechanisms and drug responses.[226] Overall, bioprinted tissue provides models for disease and drug discovery applications.[226] The use of bioprinting technologies has the potential to significantly advance our understanding of disease pathophysiology and facilitate the development of personalized medicine approaches.[226]

In some ways, the drawbacks and advantages of 3D cell culture models are the same. In much the same way that in-vivo models will always have higher variability and error than their 2D cell culture counterparts, [227,228] 3D models will always show “messier” data than neater 2D models. However, this “messiness” may be exactly what we need in trying to close the gap in in-vitro-in-

vivo-correlation. (IVIVC.) While all scientists long for neat, clear, and easily understood and analyzable data, the variability and vagaries of the living creatures make this an unattainable reality for those scientists attempting to investigate life and everything that can go wrong with it. My results in this regard are no exception. Each 3D tumor spheroid model was done in parallel with a 2D flat cell culture model, and unsurprisingly, in every instance, the 2D model was neater, "prettier" and easier to interpret. However, while that is the case, perhaps there would be fewer billions of dollars wasted, not to mention the precious time of those sick and waiting for cures, if the messiness of potential disease treatments could be seen earlier on in the drug discovery process.

4.3 Methods

4.3.1 2D Models

4.3.1.1 Cell-Culture and Antiproliferation Assays.

U87 cells were grown to ~80% confluence in Dulbecco's Modified Eagle's Medium (DMEM) supplemented with 10% fetal bovine serum (FBS) and 1% penicillin/streptomycin in a 75 cm^2 tissue culture flask and maintained at 37 °C with 5% CO_2 in a tissue culture incubator. Cells were then trypsinized, collected, and pelleted by centrifugation at 4 °C and 1200 rpm for 5 min. The cell pellet was then resuspended in DMEM with 10% fetal bovine serum and 1% penicillin/streptomycin), and the cell concentration was determined using a Countess cell counter (Invitrogen). After the initial cell concentration was determined, the suspension was diluted to 1.0 × 10^5 cells/ml. Next, a multichannel pipet was used to fill a 96-well plate with 100 μL/well of the diluted cell suspension. The cell-loaded plates were then incubated for 24 h at 37 °C under an atmosphere of 5% CO_2 in order to allow the cells to completely adhere to the surface of the wells.

PNPs were prepared as described in earlier chapters and analyzed by HPLC for drug content. 24 hours after cell seeding, PNPs were diluted with autoclaved water to a normalized SN-38 concentration of 6 µM. The curcumin concentration was then calculated based on the HPLC data. SN-38-PNPs did not contain enough SN-38 to reach a concentration of 6 µM and were simply used "as is" at the maximum concentration possible.

For free drug mixtures, stock solutions of 1 wt % SN-38 in DMSO and 10 wt % of CUR in DMSO were prepared. SN-38 and CUR stock solutions were then combined in various ratios to match the ratio of the analyzed PNPs and each of the mixtures was diluted to a final concentration of 6 µM SN-38. Serial dilutions were carried out in autoclaved water containing 0.05% DMSO, and then each diluted stock was diluted 1:1 in 2x DMEM containing 20% FBS and 2% penicillin/streptomycin to a concentration of 3 µM SN-38 and 1x concentration of DMEM. All samples, whether containing free drug, PNPs, or simply media, contained an equal concentration of 0.05% DMSO, for consistency. Each well was gently aspirated, and then 200 µl of the appropriate dilution was added to the appropriate well of the 96-well plate, in order to generate a range of different concentrations for analysis. The treated cells were incubated for 3 or 7 d at 37 °C under a 5% CO_2 atmosphere. In order to determine cell viability, PrestoBlue was used according to the published instructions. Briefly, PrestoBlue was mixed 1:9 in 1x DMEM containing 10% FBS and 1% penicillin/streptomycin. Media was aspirated from all plate wells, and 110 µl of diluted PrestoBlue/DMEM was added to each well. After the addition of the PrestoBlue, the 96-well plates were incubated for 40 m (5% CO_2, 37 °C). 100 µl of the media was then transferred to a clean 96 well plate and fluorescence (λ_{ex} = 560 nm; λ_{em} = 590 nm) readings were recorded on a 96-well plate reader. Cell death was calculated for each well based upon the following formula:

$$\%\ Death = \left[1 - \frac{(S - B_o)}{(B_t - B_o)}\right] \times 100$$

where S is the sample reading (cells + drug + media), B_t is the average reading for the untreated population of cells (cells + media), and B_0 is the average reading of wells containing media only.

% Death vs. SN-38 concentration data sets were fit by Carter Castor using R. Each data point in the curve (and its error bars) is derived from four separate technical replicates of the same PNP preparation and concentration. Curves were normalized to 0% cell death at the lowest drug concentrations.

EC_{50} values were then determined by calculating the SN-38 concentration required to elicit a 50% reduction in cell viability, based on the fitted curves. Experimental errors on these values were determined on the basis of the quality of the fits.

For 3D cell models: U87 cells at the same passage number and from the same source as those used in the equivalent 2D cell model were used. Cells were seeded in bioprinted well microarrays called EZ-Seed plates, proprietary to Apricell Biotechnology using proprietary techniques. Wells were placed in 48 well plates and seeded there. After 4 days for spheroids to form, the 48 well plates, containing 500 µl of DMEM containing 10% FBS and 1% penicillin/streptomycin were dosed with PNPs and free drug mixtures in exactly the method described above for 2D cell cultures. The only difference is that the final volume per well was 500 µl.

PrestoBlue was diluted in the same way as for the 2D cell models, and after all wells were gently aspirated, 200 µl of the PrestoBlue dilution was added to each well, which was enough to fully cover the microwell chips. After the addition of the PrestoBlue, the 96-well plates were incubated for 1 h (5% CO_2, 37 °C) to allow full penetration of the spheroids. 100 µl of the media was then

transferred to a clean 96 well plate and fluorescence (λ_{ex} = 560 nm; λ_{em} = 590 nm) readings were recorded on a 96-well plate reader. Cell death was calculated in the same was as for the 2D model.

For both 2D and 3D models, control wells were used containing PNPs containing only curcumin, empty PNPs containing no drug, and untreated cells. DMSO controls were not used as all wells contained an equal concentration of DMSO.

For both 2D and 3D models, for the 3 d timepoint, media aspirated from each well was carefully saved. After PrestoBlue readings were complete, each well was washed twice with PBS, aspirated, and then the original media was replaced in the well. For 2D models, an additional 100 µl of 2x DMEM containing 20% FBS and 2% penicillin/streptomycin was added to each well. For 3D models, an additional 250 µl of 2x DMEM containing 20% FBS and 2% penicillin/streptomycin was added to each well. This was to ensure there was no nutrient depletion of the cell environment in the second half of the 7 d experiment.

4.3.2 Imaging

After the 7 d experiment, in the 3D model, certain samples were set aside for imaging. Because curcumin is naturally fluorescent, spheroids could be imaged without the need for altering PNPs with fluorescent tags. One sample each of untreated cells, cells treated with the maximum dose of SN-38/CUR-PNPs, cells treated with the maximum dose of CUR-PNPs, and cells treated with the maximum dose of free drug mixture were set aside for imaging. CUR-PNPs were selected along with SN-38/CUR-PNPs because those PNPs containing SN-38 often showed so much cell death that the spheroids were no longer intact. Therefore the CUR-PNPs were used as a better indicator of PNP tumor penetration.

The wells selected for imaging were washed thoroughly twice with PBS and then aspirated. They were then filled with 10% formamide solution and allowed to incubate for 20 m (5% CO_2, 37 °C), until spheroids could be seen as white pinpoints in the 48 well plate. Plates were then sealed in parafilm and refrigerated at 4 °C until imaging could be completed.

The following day, samples were imaged on a confocal microscope Zeiss LSM880 to determine the degree of tumor penetration by CUR. Images used fluorescence excitation wavelength 458 nm and detected emission at 415 nm wavelength. These are not the ideal wavelengths for CUR, and are instead optimized for the use of GFP, but we were limited in our choices by the configuration of the microscope.

4.3.3 Statistics and Data Handling.

For comparison of cytotoxicity data, dose−response curves were first established using models created in R using the drc library.[229] All curves are four-parameter log-logarithmic functions:

$$f(x) = c + \frac{d - c}{1 + \exp\left(b(\log(x) - e)\right)}$$

where e is the ED_{50}. For Free OCH_3 3 day 3, the ED_{50} was fixed as a function of the two-parameter log-logarithmic function

$$f(x) = c + \frac{1}{1 + \exp\left(b(\log(x) - e)\right)}$$

to reduce the standard error. Experimental errors on these values were determined on the basis of the quality of the fits.

To compare any two results, the combined standard error SE_c was calculated from the square root of the sum of the squares of the standard errors from the individual curve fits:

$$SE_c = \sqrt{SE_1^2 + SE_2^2}$$

Similarly, the combined degrees of freedom *DOF* were calculated based upon the number of concentration values (*N*) in each data set:

$$DOF = [(N_1 - 1) + (N_2 - 1)]$$

N was 9 for each experiment; *DOF* was therefore equal to 18 for each pairwise comparison. The difference between measured results (*t*) was then expressed in terms of units of combined standard error:

$$t = \frac{EC_1 - EC_2}{SE_c}$$

Finally, a *p* value was calculated using a two-tailed test. This was carried out with the TDIST function in Excel for all pairwise comparisons, using the equation:

$$p = \text{TDIST}(t, DOF, 2)$$

Two-tailed *p*-values were then calculated as above. In all cases, differences were assumed to be statistically significant when $p < 0.05$.

4.4 Results and Discussion

Three different formulations of PNPs containing SN-38 were tested for cytotoxicity in U87 glioblastoma cells. Two formulations contained SN-38 and CUR, and one formulation contained only SN-38. Two formulations used block co-polymer PCL-b-PEO, PEO terminating in OCH_3, and one formulation used an identical block co-polymer, but terminating in C chain in an SH group. (See Table 1.) Of these formulations, all 3 were tested in 2D cell models, and 2 were tested in 3D tumor spheroid models discussed above. Each formulation of PNP had a different drug

content of both SN-38 and CUR. Dosages were normalized to a given concentration of SN-38, without consideration given to either polymer concentration or CUR concentration, because these were dependent variables that couldn't be changed without changing the SN-38 concentration. When cells were dosed with CUR-PNPs not containing SN-38, the CUR concentration was calculated from the SN-38/CUR-PNP in the experiment, and then the CUR-PNP concentration was normalized to that, again without taking into account polymer concentration, because polymer concentration is a dependent variable that cannot be altered independently. Empty PNP concentrations were calculated based on the highest polymer concentration used in the other aspects of the experiment. Empty PNPs did not show cell death, either with block co-polymer containing OCH_3 terminated PEO, or SH terminated PEO, and therefore the polymer of the PNPs is considered a harmless excipient in the experiment.

All free drug mixtures were calculated according to the drug content analyzed in the SN-38/CUR-PNPs, and mixed to match the dosages of the PNPs in the study. Therefore, for each experiment containing a different PNP, the free drug mixture was different. While SN-38/CUR-PNP-SH show higher drug encapsulation than SN-38/CUR-PNP-OCH_3 do, because the PNPs were normalized to a standard SN-38 concentration, the relevant variable was not the amount of CUR encapsulated, but rather the ratio of CUR:SN-38 encapsulated. Although CUR encapsulation was higher in SN-38/CUR-PNP-SH, it was lower relative to the amount of SN-38 encapsulated, and therefore the free drug equivalents for the two experiments show higher concentrations of CUR in the SN-38/CUR-PNP-OCH_3 experiment than in the SN-38/CUR-PNP-SH experiment. All CUR levels were also much lower than those found in Chapter 2 of this thesis, and in the accompanying published work, because the CUR drug content in the PNPs synthesized during these experiments was much lower. There is no clear reason why the CUR encapsulation was lower, but it was

consistent across the experiments in both chapters 3 and 4 of this thesis. Because of this, free drug mixtures in Chapter 2 were 25:1 and 40:1 CUR:SN-38, whereas in the experiments presented here, free drug mixtures were 4:1 and 7.3:1 CUR:SN-38.

Another area of variability between the results presented in Chapter 2 of this thesis and those presented here in Chapter 4 is the toxicity of CUR alone to U87 cells. In Chapter 2, U87 cells seem relatively impervious to even high dosages of CUR, whereas in chapter 4, different passages of the same originally sourced U87 cells show significant sensitivity to CUR. Therefore, in Chapter 2, CUR was treated primarily as an excipient, used only to increase the loading efficiency of SN-38 in PNPs and change the physico-chemical characteristics of those PNPs, whereas here in Chapter 4, it will need to be treated as a chemotherapeutic agent in its own right. Perhaps the change in the physical properties of the CUR used that resulted in the lower encapsulation of CUR in PNPs in Chapters 3 and 4 are also reflected in changes in their cytotoxic properties. Whatever the reason, we can only deal with the data that is presented to us and draw conclusions as best we can.

Experiments will be designated Experiment SH-2D, SH-3D, OCH_3-CUR-2D, OCH_3-CUR-3D, and OCH_3-NO CUR-2D. Experiment nomenclature reflects which polymer was used in the PNP formulation, and whether CUR is co-encapsulated in the SN-38-PNPs. SN-38 is not listed in the nomenclature because all experiments contain SN-38.

In Figure 29 we can see the trend in efficacy between day 3 and day 7 of the experiment across different formulations, both encapsulated and free drug. Overall there is a trend of increasing efficacy as time increases, but this is primarily significant in the formulation not containing curcumin. Free drug at a ratio of 7.3:1 CUR:SN-38 also shows a significant difference in EC_{50} between day 3 and day 7, but it is less significant than the difference seen when CUR is not present.

It can also be seen in Figure 29 that overall, the OCH_3-NO CUR is less potent than the formulations containing CUR, but especially at day 3. This will be further described in further figures below. One possibility for this observation is that curcumin is enabling the penetration of SN-38 into the cell. Studies have shown that curcumin may affect membrane permeability, and cause thinning of the membrane.[230–232] Therefore, it may take longer for SN-38 to permeate the cells and have a cytotoxic effect when administered

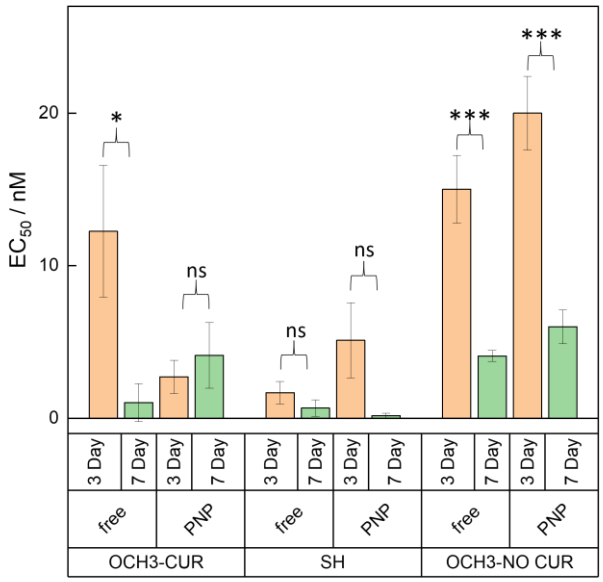

Figure 28. Comparison of EC50 values for each formulation between day 3 and day 7. Note that axes differ between figures 28-31.

A few things of note can be seen from Figure 30, some of which are more straightforward to explain than others. First of all, on day 3, there are statistically significant differences in potency between free and encapsulated drug, whereas by day 7, there are no statistically significant differences. This

can be fairly easily explained by the idea that by day 7, all drug has been released from the PNPs and entered the cells, and therefore shows very similar efficacy.

On day 3, the differences between free and encapsulated drug for each formulation is a bit confusing. For OCH_3-CUR, free drug is more potent than encapsulated drug. For OCH_3-NO CUR, the reverse is true, and for SH, there is no significant difference between encapsulated and unencapsulated drug.

Since the polymer formulation of OCH_3-CUR and OCH_3-NO CUR are identical, it can be assumed that the difference in effect is based on the presence or absence of curcumin. There is no significant different between the effect of free drug equivalents of OCH_3-CUR and OCH_3-NO CUR at day 3, as can be seen in Figure 28. What is changing here is the efficacy of the PNP formulation. Why would a PNP containing CUR be more effective, and a PNP not containing CUR, be less effective? And if the difference is the presence or absence of CUR, why is this difference not significant either in the free drug equivalents or in the SH-PNP formulation?

One possibility is that the presence or absence of CUR in the PNP is changing the crystallinity of the PNP, which is somehow affecting the cell uptake. In previous work done in our lab, [61] CUR was found to reduce the crystallinity of PNP formulations. Perhaps the more flexible and amorphous PNP is more easily taken up by cells than the more crystalline version, and this is why we see greater efficacy in the PNP containing CUR, even though the free drug equivalents do not show a difference.

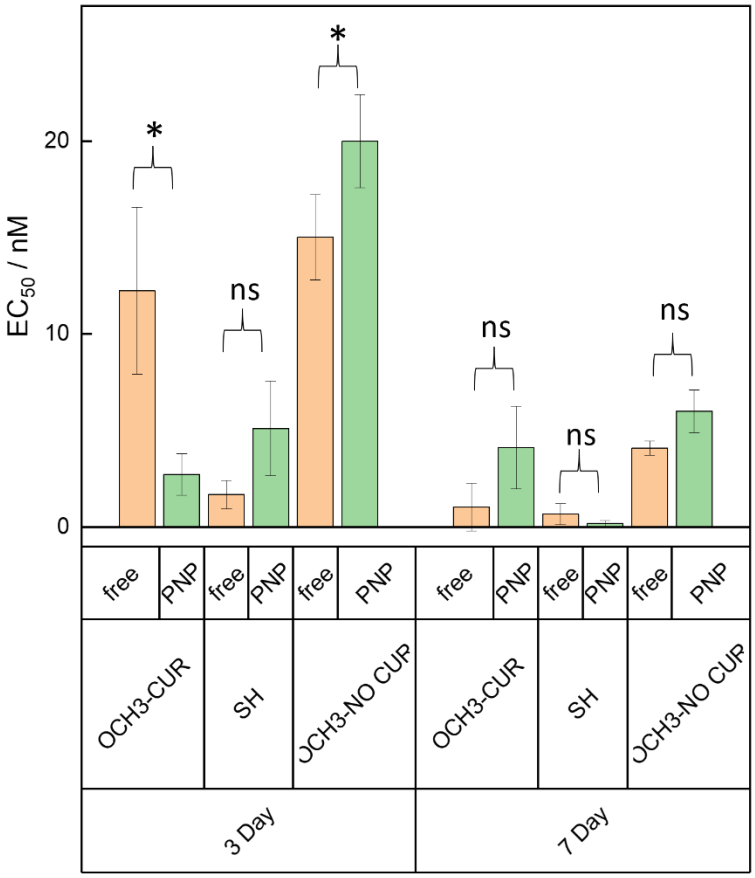

Figure 29. A comparison of free and encapsulated formulations EC_{50} values. Note that axes differ between figures 28-31.

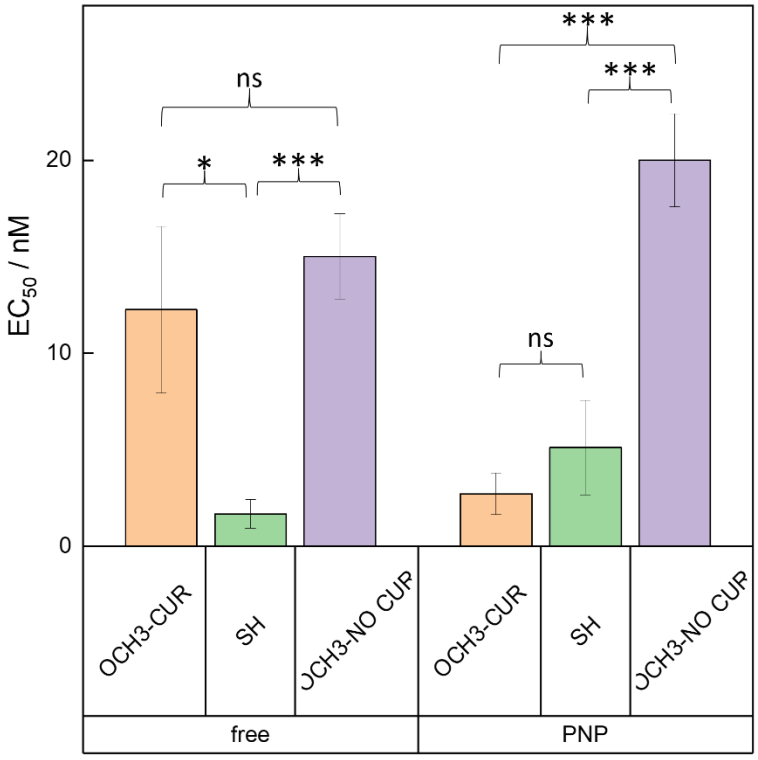

Figure 30. EC_{50} data for both free and encapsulated formulations at day 3. Note that axes differ between figures 28-31.

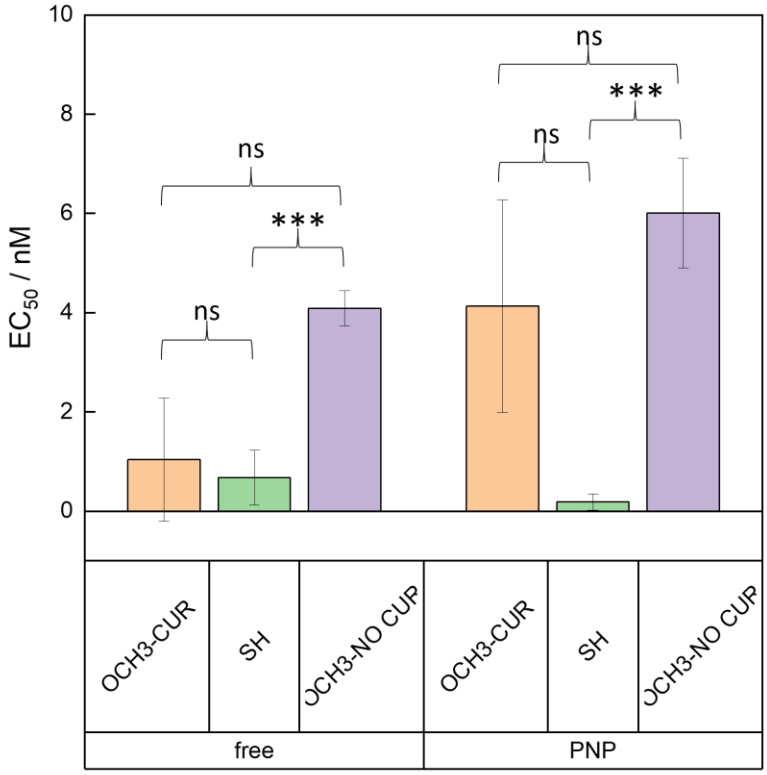

Figure 31. EC_{50} data for both free and encapsulated formulations at day 7. Note that axes differ between figures 28-31.

Looking at Figure 29 and 31 together, we can see a few different effects. One is that the significant differences of the free drug remain constant between day 3 and day 7, where the differences between the PNP formulations become somewhat less significant from day 3 to day 7. At day 3, the difference between OCH_3-CUR and OCH_3-NO CUR is statistically significant, but by day 7,

it is not. This strengthens the idea that the curcumin is influencing the cell uptake of the PNPs, but that by day 7, the PNPs are taken up by the cells and therefore the effects become more uniform. The SH-PNP formulation, however, remains significantly more potent than the OCH_3-NO CUR formulation at day 7. This is a bit confusing, as there is no significant difference between OCH_3-CUR and OCH_3-NO CUR, indicating the presence or absence of CUR is not the source of the difference, and there is also no significant difference between OCH_3-CUR and SH-CUR, indicating the polymer formulation is not the source of the difference. Perhaps the two properties are additive, and while either change alone does not produce a significant difference in potency, both together are enough to significantly increase potency.

The free drug differences are also a bit puzzling. The ratio of CUR:SN-38 in OCH_3-CUR is 7.3:1, and in SH is only 4:1. Why then is the difference in efficacy between formulations greatest between the lower concentration of CUR and the SN-38 alone? One might expect a higher concentration of CUR to give a more distinct effect. However, in the research conducted by Barry et. al, it seems that CUR behaves differently at different concentrations.[230] Their research shows that at lower concentrations, CUR behaves like cholesterol in membranes and induces ordering of the membrane, but at higher concentrations, CUR binds in a trans-membrane fashion and may not have the same ordering effect.[230] Based on this, perhaps there is a 'sweet spot' for the ideal concentration of curcumin for increased drug penetration, and the 4:1 ratio is actually more effective for drug penetration than the 7.3:1 ratio.

Experiment SH-3D, as seen in Figure 32 below, is unfortunately harder to interpret than the 2D results. As expected in 3D models, error bars are larger, and it is difficult to interpret any dose dependent trend from the limited data provided. 3D experiments were performed with significantly

fewer samples than the 2D experiments, because of the logistical difficulties of creating large quantities of tumor spheroids. Therefore, what conclusions we can draw must be drawn from a smaller pool of data than would be ideal

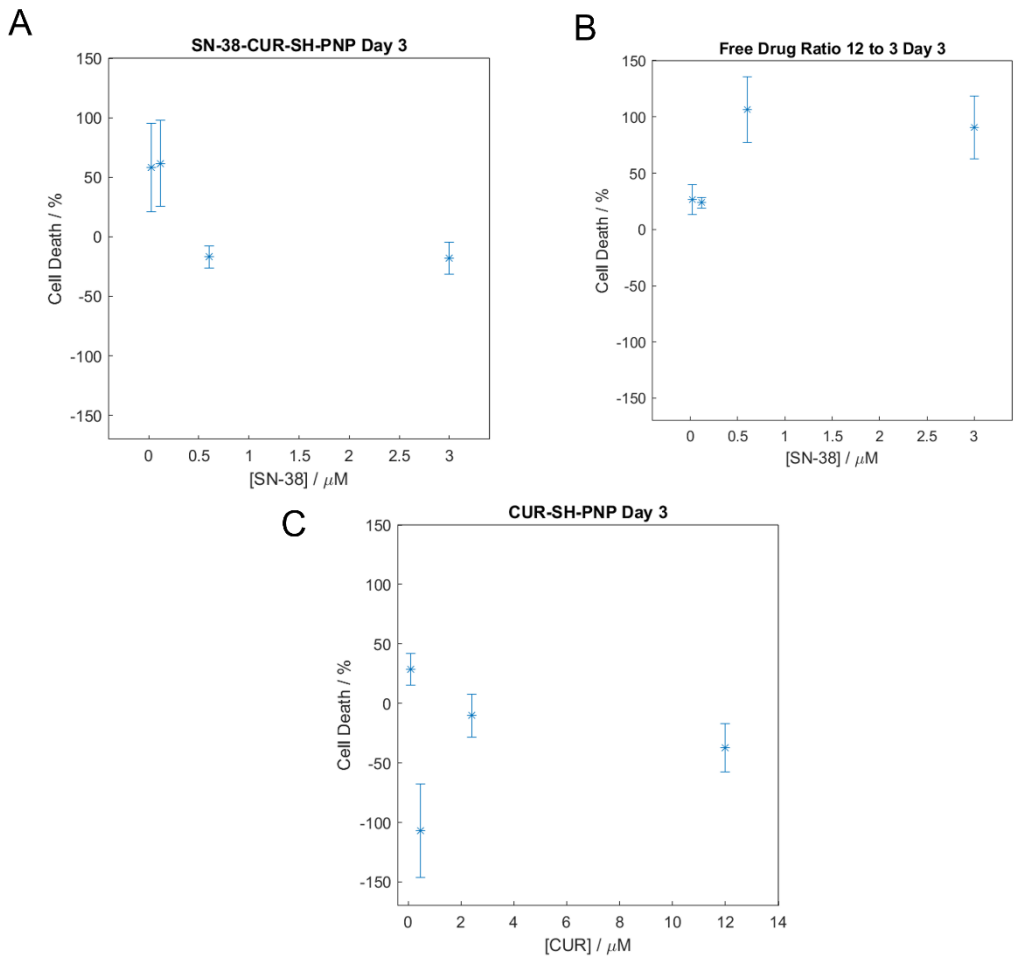

Figure 32. Dimension SN-38/CUR-PNP-SH cytotoxicity day 3

(A) CUR-SH-PNP, (B) SH-PNP free drug equivalent, (C) SN-38/CUR-PNP-SH

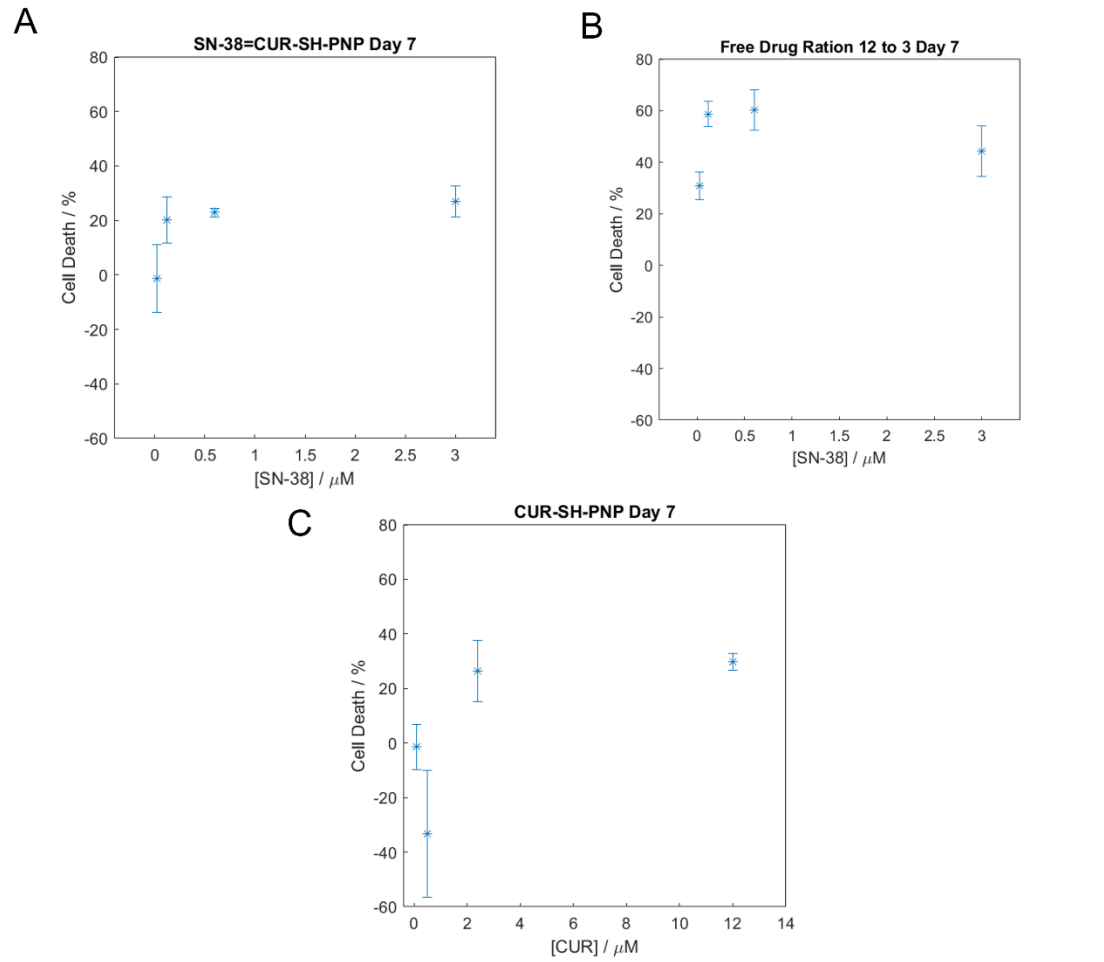

Figure 33. 3-dimension SN-38/CUR-PNP-SH cytotoxicity day 7

(A) CUR-SH-PNP, (B) SH-PNP free drug equivalent, (C) SN-38/CUR-PNP-SH

From the data presented above, one clear conclusion that can be drawn is that 3 days may not be enough time to understand the effects of the drug dosing on the cell spheroids. Day 3 data shows no dosage dependency, large error bars, and perhaps most confusingly, no cell death at the highest concentrations of SN-38/CUR-PNP-SH. However, when we examine the data from day 7, many if not all these problems resolve. The error bars shrink significantly by day 7, a dose dependency becomes clear to at least some extent, and, as expected, higher concentrations of SN-38/CUR-PNP-SH show higher cell death than lower concentrations. Continuing to concentrate on the day

7 data, a few things stand out. While four concentration points did not give sufficient data to fit an EC50 curve, percentages of cell death can still be seen.

One immediate observation that can be made, and is to be expected based on the literature,[223,233–236] is that the potency of the same concentration of SN-38 in the tumor spheroids is much lower than that same concentration in 2D models. Without fitting a curve and extrapolating an exact value, 50% killing seems to be achieved, where achieved at all, closer to µM concentrations than nM concentrations. This is not surprising, and fits well with previous knowledge in the field, underscoring the importance of using 3D models before attempting to determine dosages for in-vivo experiments.

In addition to this, two items in the data are stand out particularly. One is that, in contrast to the 2D data, free drug at 7 days seems more potent than PNPs, showing ~60% cell death at 1 µM SN-38, in contrast to 30% cell death with the same SN-38 concentration in PNPs. The second point, which is even stranger and harder to explain, is that PNPs containing CUR alone seem to show similar results to data with SN-38-PNPs.

The first point is particularly puzzling when combined with the imaging data, shown below in Figure 35.

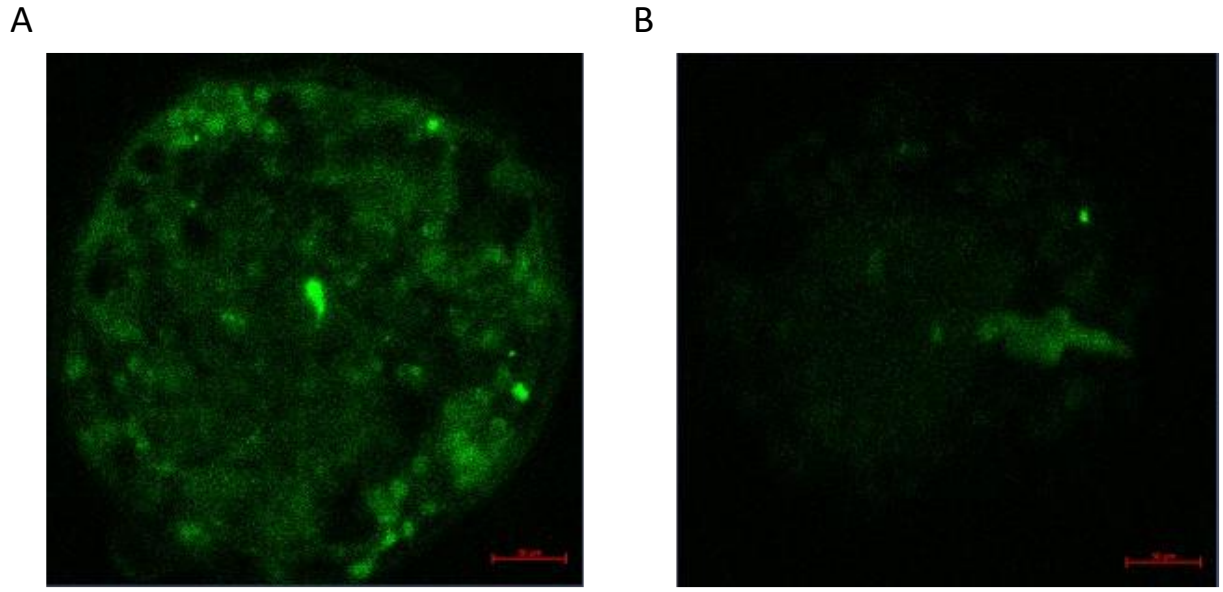

Figure 34. Confocal images of individual tumor spheroids

Confocal images of individual tumor spheroids treated with (A) CUR-SH-PNPs and (B) SH-PNP free drug equivalent.

As seen from the fluorescence of CUR in the confocal images, free drug does not appear to have significant tumor penetration, whereas PNPs do. Why then, would free drug have higher killing than PNPs? As with previous hypotheses, obviously nothing can be proven or disproven without further experiments, but there are some possibilities. One possibility is that, while our release kinetics data in Chapter 3 show SN-38 and CUR more or less releasing together, it's always possible that we see CUR, but SN-38 is not there. Since SN-38 is the chemotherapeutic agent, using CUR for imaging has an inherent weakness in that we have to assume that where we see CUR, we would also see SN-38, were it visible. While this explanation is possible, it doesn't seem all that compelling, because of the release results we've seen, and because of the 2D data, which could indicate that SN-38 is still present in the particles between day 3 and day 7. Another possibility is while there is both CUR and SN-38 in the PNPs still, they are both still inside the PNPs. In our previous hypothesis regarding the potency of SN-38/CUR-PNP-SH in 2D culture on day 7, we posited that the ester bonds in the PCL of the PNPs was hydrolyzing by day 7 and

releasing the drug. However, that hydrolysis requires the presence of water, something that is plentiful in 2D culture, but perhaps is less plentiful in the center of a tumor spheroid. The center of the tumor spheroid could also be hypoxic, which could change the hydrolysis kinetics. More broadly, perhaps there is simply something different in the physical environment of the tumor spheroid that slows down the hydrolysis of the PNPs, and if we were able to continue the experiment for a longer time scale, we would see the kind of cell death we would anticipate based on previous data. Another possibility is that, with our confocal resolution, we can clearly see tumor penetration, but we can't see whether the PNPs, or more accurately, the CUR, is inside the cells or between the cells. Perhaps, again because of differences in the physical environment, the PNPs are not getting internalized into the cells as we had hoped, and therefore are not as effective. While the free drug seems clearly not to be penetrating the tumors, perhaps it is more effective at killing the cancer cells it does reach, and the cell killing at the periphery of the tumor is enough to create the discrepancy we see in potency, which is averaged across all cells in the spheroid.

Additionally, 2D and 3D cultures may behave differently in regards to the way the remaining healthy cells are growing and dividing. The centers of the cell spheroids may be hypoxic, and certainly have less access to the nutrients of the cell media than the cells on the outside of the spheroid do. They are also spatially more crowded, with less area to multiply than the cells on the surface of the spheroid. Therefore, tumor penetration may not be as helpful as one would assume in overall tumor killing. Perhaps by distributing the same total concentration of drug throughout the tumor, less drug is concentrated around the surface of the tumor, and these surface cells are continuing to grow and divide, providing healthy cells for the PrestoBlue assay and obscuring the cell death that is occurring. This result wouldn't necessarily translate to longer term results, particularly in-vivo, because if tumor cells deep inside the spheroids were surviving the free drug,

once the other dead cells were cleared away by the systems of the organism, the living cancer cells would be free to start new tumors and prevent cancer remission. Certainly for clinical use of chemotherapeutic agents, tumor penetration is essential for treating cancer,[237–239] regardless of whether the EC_{50} cell data shows better efficacy when averaged across the entire spheroid.

Even more puzzling is the second point, which is that, at 7 days, CUR-PNPs seem to show similar efficacy to SN-38/CUR-PNPs. While U87 cells in this study did show a distinct sensitivity to CUR, it is still widely accepted that the cytotoxic potency of CUR is far less than that of SN-38. CUR is routinely eaten by people without causing harm, in contrast to SN-38, and previous research in our own group shows EC_{50} values for CUR-PNPs in 2D cell culture cytotoxicity studies to be in the range of 25 μM, albeit using a different cell line and different PNP formulation.[88] One possibility that cannot be eliminated without the repetition of the experiment is of course some sort of experimental error, but assuming the data is correct, one possibility goes back to the same explanation above for why free drug is so much more potent than PNPs in spheroids. Perhaps the SN-38 trapped in the PNPs has simply not released from the PNPs, even at 7 days, and is therefore not exerting any cytotoxic effect as yet, and if the experiment could be continued for a longer time scale, we would start to see the effects of the release of the SN-38.

Experiment 3D-CUR-OCH_3 has some of the same features as the 3D-SH, but not entirely, as seen in Figure 35 and 36, below.

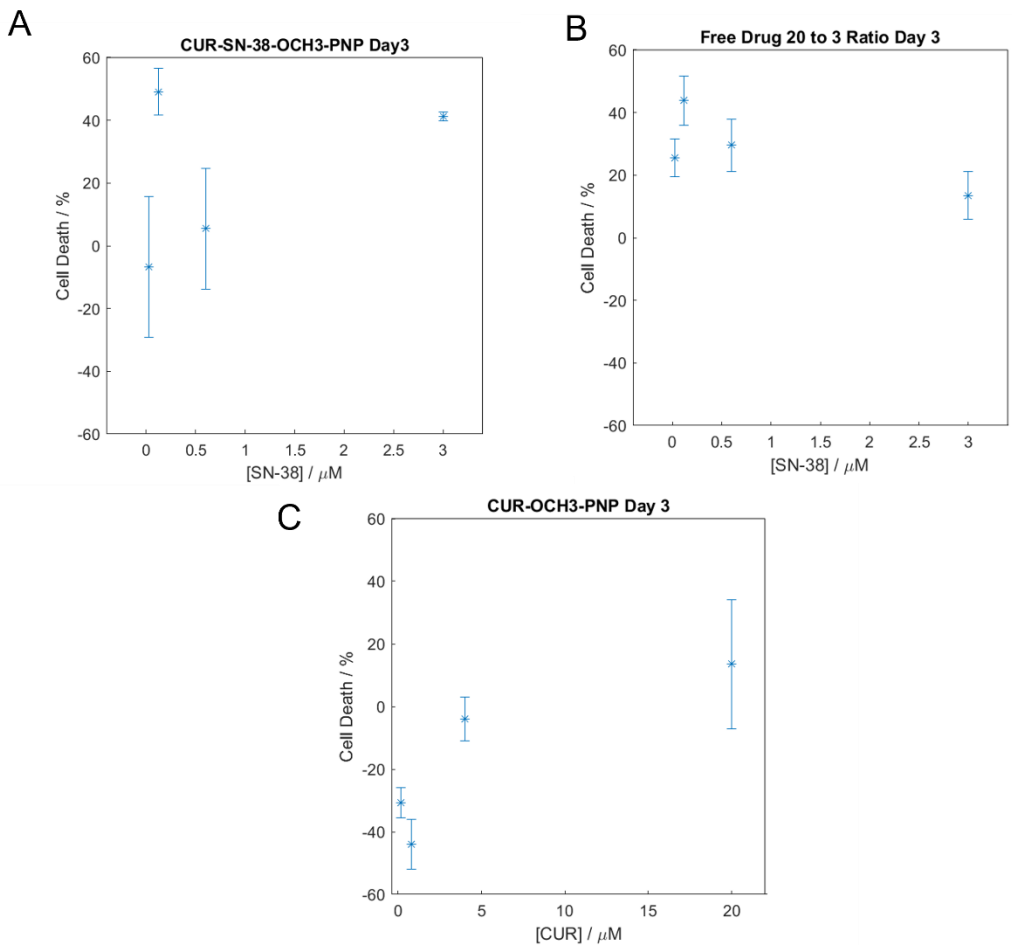

Figure 35. 3-dimensional SN-38/CUR-OCH_3-PNP cytotoxicity day 3

(A) CUR- OCH_3-PNP, (B) OCH_3-PNP free drug equivalent, (C) SN-38/CUR-PNP- OCH_3

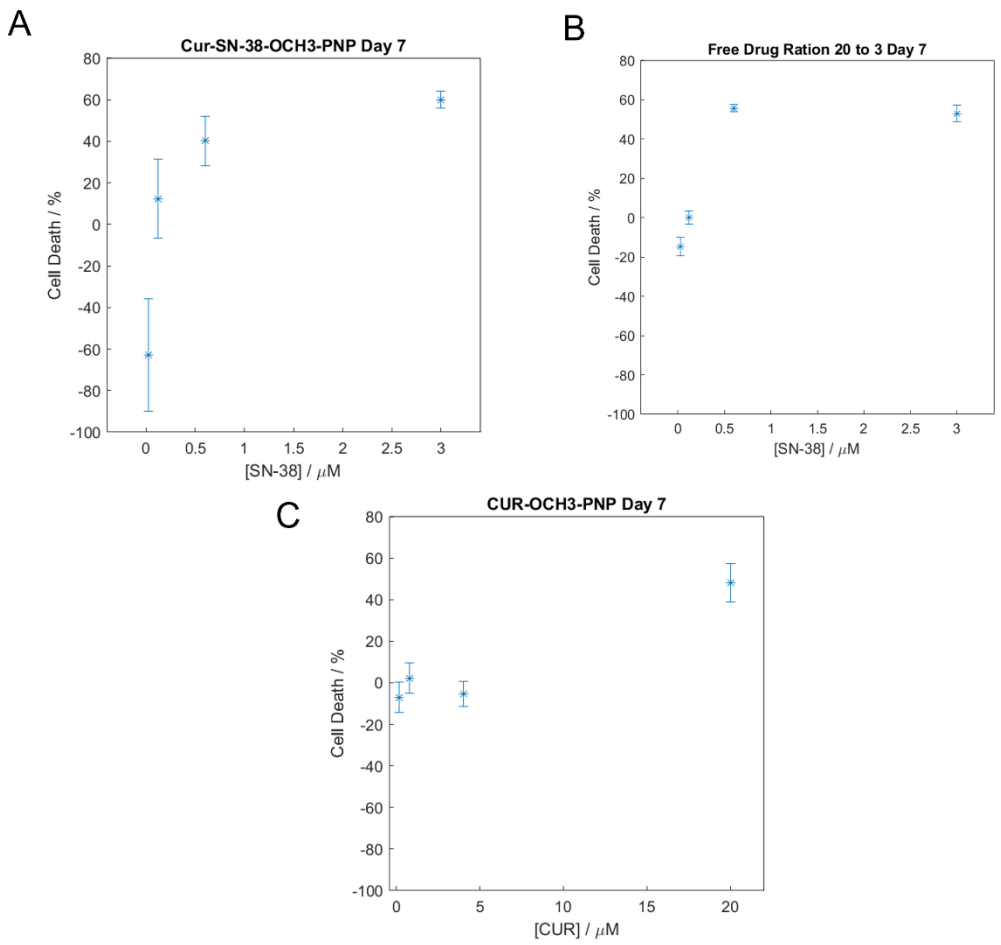

Figure 36. 3-dimensional SN-38/CUR-OCH$_3$-PNP Cytotoxicity day 7

(A) CUR- OCH$_3$-PNP, (B) OCH$_3$-PNP free drug equivalent, (C) SN-38/CUR-PNP- OCH$_3$

Again, in this experiment, 3 days may have been too early to get meaningful results, with data showing large error bars and a lack of dosage dependency. However, as we look at day 7, some of the strange effects we saw in Experiment 3D-SH do not seem to be present, and the results are a bit easier to interpret. First, CUR-PNPs do not show cytotoxicity until they reach concentrations of 20 µM, at which point cytotoxicity would be expected. Secondly, both PNPs and free drug mixtures show a clear dose dependent curve. Cell killing overall is also higher with these PNPs than those from the previous experiment, while free drug cell killing holds relatively steady between the two experiments. In 3D-CUR-OCH$_3$, while PNPs don't clearly outperform free drug

at day 7, they appear to hold steady with free drug in efficacy, as opposed to the results in 3D-SH. As before, all potency in the 3D models is much lower than that seen in the 2D models, as is expected from the literature. Perhaps the increased efficacy of the PNPs in this experiment is due to increased polarity of the exterior of the PNPs, somehow allowing for better or different localization within the cells of the spheroids. Again, the results are averaged across all the cells of the spheroids, and so we don't know if the free drug is killing more of the outer surface cells in contrast to a more spread-out cell killing by the PNPs, which is a subject that bears further research.

Confocal images were taken of representative samples of both 3D experiments. CUR-SH-PNP and SH-PNP free drug equivalent were optimized using the same parameters, are shown in Figure 35, clearly indicating that PNPs achieve better penetration than free drug. Below, in Figure 35, the

same two SH samples are shown alongside CUR-OCH_3-PNP and OCH_3 free drug equivalent, this time all 4 optimized using identical parameters to best compare between samples.

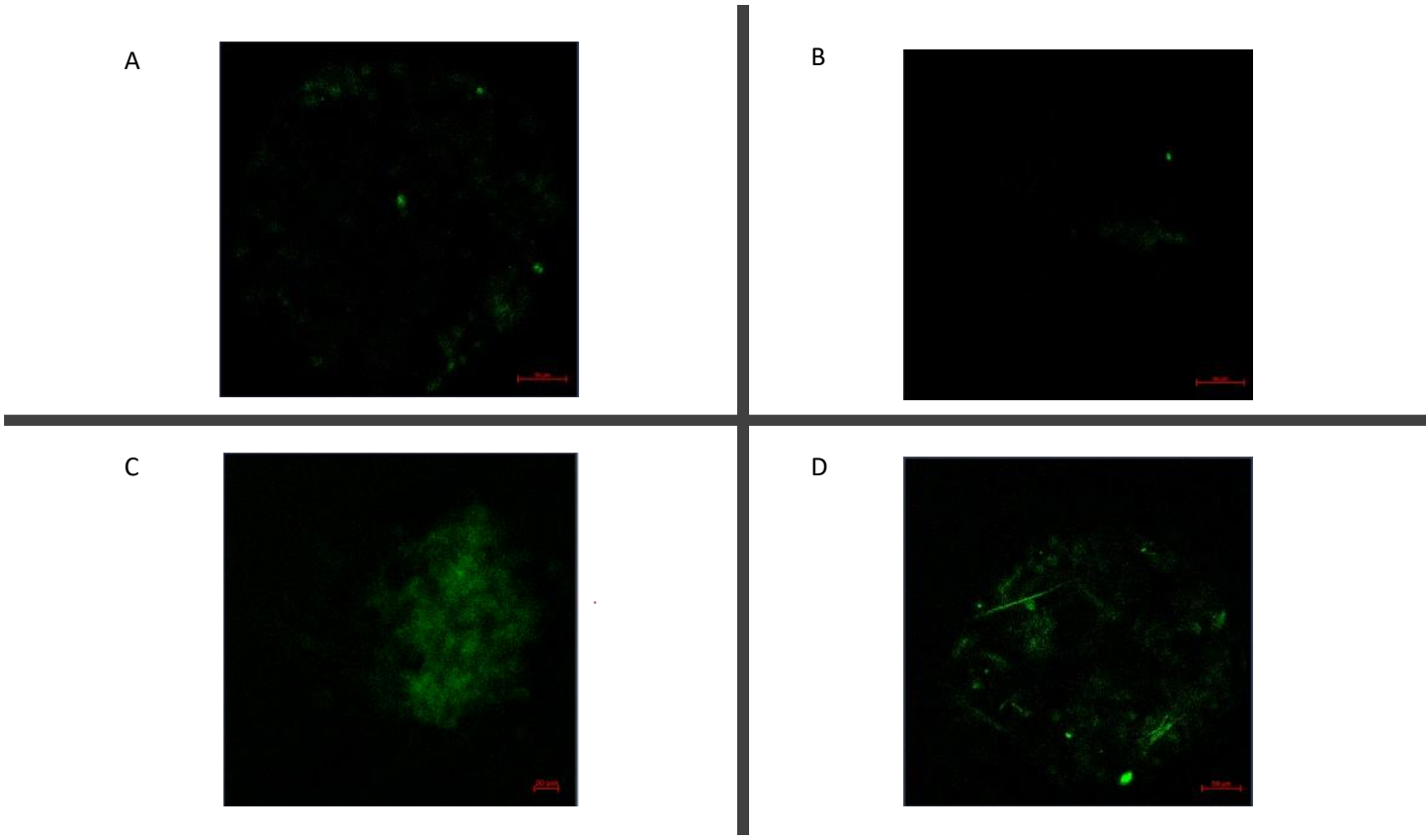

Figure 37: Confocal images of tumor spheroids 7 days after dosing

(A) CUR-SH-PNP (B) SH free drug equivalent (C) CUR-OCH_3-PNP (D) OCH_3 free drug equivalent.

As can be seen when compared across samples, OCH_3-PNP shows markedly better tumor penetration than SH-PNP, which perhaps explains the increased efficacy of OCH_3-PNP in 3D models, as compared so SH-PNP in the same models.

4.5 Conclusions

There are many interesting differences between the formulations tested in 2D and 3D cell models. As expected, 3D cell models required significantly higher doses of drug to induce cell death.

Variation and error was also higher in 3D cell models, as expected. Knowing just how much drug potency was reduced using a 3D model will be instrumental in devising appropriate dosages for any in-vivo experiments going forward.

On the face of it, the differences between the formulations are slightly disappointing, in that the PNP-SH formulation seemed to show great promise in both physico-chemical characteristics, particularly drug loading, and in the 2D cell models, but then in the 3D tumor spheroid model does not show as much promise and is eclipsed by the reference formulation of the PNP-OCH_3. However, further refinement could still bear out the promise of the PNP-SH formulation. One problem faced by the PNP-OCH_3 formulation, which is not clearly seen in the data because of the normalization to SN-38 concentrations, is how large a dose of medication would be needed to achieve the desired cell killing effect. It can be seen from these data that 3 μM is barely enough to get to 60% killing, and presumably in-vivo or clinical studies would be aiming for closer to a 100% cell killing level. Because of the low drug content of these particles, and the inherent dilution of the particles that occurs during the nanoprecitation method, it will be hard to achieve higher doses without either concentrating the particles, which can change their stability, or using extremely large volumes, a method that carries its own risks and adverse effects. One advantage of the SH-PNP formulation is, although it is also dilute because of the nanoprecipitation method, each particle contains twice as much SN-38, and therefore reaching the higher doses that 3D models and presumably in-vivo work would require may be easier to achieve. That being said however, further research into the mechanism of action allowing for twice the efficacy of PNP-OCH_3 particles as PNP-SH particles in tumor spheroids might allow us to combine the best of both worlds for a formulation that would be truly the most effective.

Previous work in our lab worked with stimulus responsive polymers that shed parts of the polymer chain under certain conditions.[93,121] If indeed, the PEG terminal end group is improving drug encapsulation and certain other properties, but hindering proper localization of the PNP in the cell, perhaps a new formulation could be designed that allowed for the end group to be present during synthesis and encapsulation but then be shed once the PNP reached the tumor.

Repetition of the experiments presented here is a prerequisite for any work going forward, and then a thorough digging into mechanism of action of cell death would be extremely beneficial to understanding the differences between efficacy of formulations.

Further research is always needed to continue to refine and develop a product, however the results presented here provide a firm basis for the merit of continued research into the use of polymeric nanoparticles for the delivery of SN-38 for cancer treatment, and particularly the use of co-encapsulation of CUR with SN-38 and of thiol terminated PEG end groups to optimize the PNP formulation. The use of 3D models highlights some of the inconsistencies between formulations and also the need to increase available concentration of SN-38 in order to achieve efficacy.

5 Chapter 5: Conclusions

In this thesis study, formulations of SN-38 encapsulated in PCL-b-PEO polymer nanoparticles were optimized and extensively tested. The overall goal was to improve the drug encapsulation of SN-38 in the PNPs, and to increase efficacy of the formulation at eradicating cancer cells, with an eye toward the eventual use of such a formulation in the clinic for cancer patients.

In Chapter 2, curcumin (CUR) was co-encapsulated with SN-38 in the PNPs, using both bulk and microfluidic nanoprecipitation methods, and the addition of CUR was found to both improve SN-38 encapsulation and also decrease polydispersity of the resulting particles. Microfluidic manufacturing did give an advantage over bulk nanoprecipitation in both drug encapsulation and polydispersity of particles. Cell experiments showed a clear advantage of one SN-38/CUR formulation over another but did not provide hints into the mechanism of this advantage. Release kinetics studies found a drawback of these formulations in that they showed a burst release of drug in the first few hours. Polymer-free nanoprecipitation experiments gave an insight into mechanism of increased SN-38 encapsulation by showing an association of SN-38 and CUR in DMF.

In Chapter 3, efforts to crosslink the PNPs in order to slow release kinetics led to an in depth investigation of the effect of PEO-terminal end groups on the physico-chemical characterization of SN-38/CUR PNPs. Clear differences were seen between different end-groups, and a trend of less polar end groups showing better drug encapsulation was seen, but this trend was broken by the least polar end group, the C6-PNP. The SH-PNPs, synthesized with bulk nanoprecipitation, ended up showing the most promise, and was the formulation brought forward for further testing.

Chapter 4 detailed the cytotoxicity experiments in both two and three dimensional cell models of PNPs using OCH_3 and SH PEO end groups, some PNPs containing a blend of SN-38 and CUR, and one formulation containing SN-38 alone. Further study is required to elucidate clear trends from this work, but it can be seen from confocal microscopy of the naturally fluorescent curcumin that PNPs do have good tumor penetration, and better penetration than unencapsulated drug of equivalent concentration. It could also be clearly seen that concentrations required to achieve efficacy in three dimensional cell models is far higher than what is required in two dimensional models, giving insight into appropriate dosages for in-vivo experiments in the future. Longer timescales were also required to see efficacy in the three dimensional models. Two dimensional cell study results showed some interesting preliminary findings, but will require further study before clear conclusions can be reached.

One trend that becomes clear throughout this study that I think bears further study is the effect of the hydrophobic nature of SN-38 and its resulting difficulty in encapsulating using the system and methods traditionally used in our lab. While co-encapsulation with curcumin and the addition of an SH-end group do greatly increase drug encapsulation, at the end of the study, drug encapsulation numbers are still relatively low, uniformly below 30%. Given the difficulty of concentrating particles, and the increased dosages of drug required for efficacy in three dimensional models, I believe further research must return to the initial system to optimize it for the use of such a hydrophobic drug. There are solvents far less polar than DMF, and polymers more hydrophobic than PCL. Compatibility issues between the PDMS microfluidic reactor and the solvent could be circumvented by using a glass chip rather than a PDMS chip. PDMS is an excellent material for use in labs where microfluidic chips are frequently redesigned and changed, but in a system such as ours, where the chip remains constant throughout the

experiments, a glass chip would allow a wider range of solvents for microfluidic nanoprecpitation.[240,241] Research in the Lavasanifar group showed the use of a modified PCL polymer with a benzyl pendant, which showed promise for the encapsulation of SN-38[242], but was too hydrophobic for use in a DMF nanoprecipitation system. By using a more hydrophobic solvent such as THF or acetone, such a modified polymer could also be used, and I believe this, combined with our discoveries of co-encapsulation with curcumin, two-phase microfluidic reactors, and the use of SH-terminated PEO end groups, could yield truly exciting results. Additionally, unpublished initial experiments done at the beginning of this study tested PNPs made with 2k, 6k and 12k lengths of PCL. 12k was found to be the best option, and all further experiments were carried out with 12k PCL. However, given that it was the longest polymer chain that showed the best results, I believe we were remiss in not pursuing this trend to its logical conclusion, and attempting synthesis of PNPs with 16k or even 20k PCL chains. This too, I believe, could positively influence the characteristics of the resulting PNPs. It is my hope that these modifications, in addition to further cell studies and continued efforts to improve the release kinetic profile of the PNPs, will be carried out by future students and one day bring SN-38 into use to benefit cancer patients who desperately need more effective treatments for their disease.

6 References

1. Ernsting MJ, Murakami M, Roy A, Li SD. Factors Controlling the Pharmacokinetics, Biodistribution and Intratumoral Penetration of Nanoparticles. *J Control Release*. 2013;172(3):782. doi:10.1016/J.JCONREL.2013.09.013

2. Patra JK, Das G, Fraceto LF, et al. Nano based drug delivery systems: recent developments and future prospects. *J Nanobiotechnology 2018 161*. 2018;16(1):1-33. doi:10.1186/S12951-018-0392-8

3. Mitchell MJ, Billingsley MM, Haley RM, Wechsler ME, Peppas NA, Langer R. Engineering precision nanoparticles for drug delivery. *Nat Rev Drug Discov 2020 202*. 2020;20(2):101-124. doi:10.1038/s41573-020-0090-8

4. Sánchez A, Mejía SP, Orozco J. Recent Advances in Polymeric Nanoparticle-Encapsulated Drugs against Intracellular Infections. *Molecules*. 2020;25(16). doi:10.3390/molecules25163760

5. Bourquin J, Milosevic A, Hauser D, et al. Biodistribution, Clearance, and Long-Term Fate of Clinically Relevant Nanomaterials. *Adv Mater*. 2018;30(19):1704307. doi:10.1002/ADMA.201704307

6. Wilczewska AZ, Niemirowicz K, Markiewicz KH, Car H. Nanoparticles as Drug Delivery Systems. *Pharmacol Reports*. 2012;1140(12):70901-70905. doi:10.1016/s1734-1140(12)70901-5

7. Sun T, Zhang Y, Pang B, Cha DH, Yang M, Xia Y. Engineered Nanoparticles for Drug Delivery in Cancer Therapy. *Angew Chemie*. 2014;November 1. doi:10.1002/anie.201403036

8. Palanikumar L, Choi EH, Oh J, et al. Importance of Encapsulation Stability of Nanocarriers With High Drug Loading Capacity for Increasing in Vivo Therapeutic Efficacy. *Biomacromolecules*. 2018;19(7):3030-3039. doi:10.1021/acs.biomac.8b00589

9. Wais U, Jackson AW, Chen Y, Zhang H. Nanoformulation and Encapsulation Approaches for Poorly Water-Soluble Drug Nanoparticles. *Nanoscale*. 2016;January 28. doi:10.1039/c5nr07161e

10. Yoo J-W, Chambers E, Mitragotri S. Factors That Control the Circulation Time of Nanoparticles in Blood: Challenges, Solutions and Future Prospects. *Curr Pharm Des*. 2010;16(21):2298-2307. doi:10.2174/138161210791920496

11. Houdaihed L, Evans JC, Allen C. Dual-Targeted Delivery of Nanoparticles Encapsulating Paclitaxel and Everolimus: a Novel Strategy to Overcome Breast Cancer Receptor Heterogeneity. *Pharm Res*. 2020;37(3):1-10. doi:10.2174/138161210791920496

12. Zhou Y, Zhou C, Zou Y, et al. Multi pH-sensitive polymer-drug conjugate mixed micelles for efficient co-delivery of doxorubicin and curcumin to synergistically suppress tumor metastasis. *Biomater Sci*. 2020;8(18):5029-5046. doi:10.1039/d0bm00840k

13. Shrestha B, Zheng C, Romero G. Nanoparticles-Mediated Combination Therapies for Cancer Treatment. *Adv Ther*. 2019;2(11). doi:10.1002/adtp.201900076

14. Huang CM, Liu L, Hu R, Qu J. Effect of Surface Coating of Gold Nanoparticles on Cytotoxicity and Cell Cycle Progression. *Nanomaterials*. 2018;8(12). doi:10.3390/nano8121063

15. Kim JM, Åberg C, Cárcer G de, Malumbres M, Salvati A, Dawson KA. Low Dose of Amino-Modified Nanoparticles Induces Cell Cycle Arrest. *ACS Nano*. 2013;7(9):7483-7494. doi:10.1021/nn403126e

16. Xiong Y, Gulavita SPP, Chen J, Xing J. Gold Nanoparticle Sensitize Radiotherapy of Prostate Cancer Cells by Regulation of the Cell Cycle. *Nanotechnology*. 2009;20(37). doi:10.1088/0957-4484/20/37/375101

17. Yao Y, Zhou Y, Liu L, et al. Nanoparticle-Based Drug Delivery in Cancer Therapy and Its Role in Overcoming Drug Resistance. *Front Mol Biosci*. 2020;August 20. doi:10.3389/fmolb.2020.00193

18. Wang F, Wang Y, Dou S, Xiong M-H, Sun T, Wang J. Doxorubicin-Tethered Responsive Gold Nanoparticles Facilitate Intracellular Drug Delivery for Overcoming Multidrug Resistance in Cancer Cells. *ACS Nano*. 2011;5(5):3679-3692. doi:10.1021/nn200007z

19. Silva CG Da, Peters GJ, Ossendorp F, Cruz LJ. The Potential of Multi-Compound Nanoparticles to Bypass Drug Resistance in Cancer. *Cancer Chemother Pharmacol*. 2017;November 1. doi:10.1007/s00280-017-3427-1

20. Yuan Y, Cai T, Xia X, Zhang R-H, Chiba P, Cai Y. Nanoparticle Delivery of Anticancer Drugs Overcomes Multidrug Resistance in Breast Cancer. *Drug Deliv*. 2016;November 2. doi:10.1080/10717544.2016.1178825

21. Aslam M, Naveed S, Ahmed A, Abbas Z, Gull I, Athar MM. Side Effects of Chemotherapy in Cancer Patients and Evaluation of Patients Opinion About Starvation Based Differential Chemotherapy. *J Cancer Ther*. 2014;5(8):817-822. doi:10.4236/jct.2014.58089

22. Schuell B, Gruenberger T, Kornek G, et al. Side Effects During Chemotherapy Predict Tumour Response in Advanced Colorectal Cancer. *Br J Cancer*. 2005;93(7):744-748. doi:10.1038/sj.bjc.6602783

23. Blanco E, Shen H, Ferrari M. Principles of Nanoparticle Design for Overcoming Biological Barriers to Drug Delivery. *Nat Biotechnol*. 2015;September. doi:10.1038/nbt.3330

24. Odeniyi MA, Omoteso OA, Adepoju A, Jaiyeoba KT. Starch Nanoparticles in Drug Delivery: A Review. *Polym Med*. 2019;48(1):41-45. doi:10.17219/pim/99993

25. Ways TMM, Ng KM, Lau WM, Khutoryanskiy V V. Silica Nanoparticles in Transmucosal Drug Delivery. *Pharmaceutics*. 2020;August 1. doi:10.3390/pharmaceutics12080751

26. Lee BS, Yun YS, Park K. Smart Nanoparticles for Drug Delivery: Boundaries and Opportunities. *Chem Eng Sci*. 2015;125:158-164. doi:10.1016/j.ces.2014.06.042

27. Cowie JMG, Arrighi V (Valeria). *Polymers Chemistry and Physics of Modern Materials, Third Edition.* CRC Press; 2007.

28. Zhang L, Eisenberg A. Multiple Morphologies and Characteristics of "Crew-Cut" Micelle-like Aggregates of Polystyrene-b-poly(acrylic acid) Diblock Copolymers in Aqueous Solutions. *J Am Chem Soc*. 1996;118(13):3168-3181. doi:10.1021/JA953709S

29. Park S, Lee DH, Xu J, et al. Macroscopic 10-Terabit–per–Square-Inch Arrays From Block Copolymers With Lateral Order. *Science (80-).* 2009;323(5917):1030-1033. doi:10.1126/science.1168108

30. Ku S, Brady MA, Treat ND, et al. A Modular Strategy for Fully Conjugated Donor–Acceptor Block Copolymers. *J Am Chem Soc*. 2012;134(38):16040-16046. doi:10.1021/ja307431k

31. Massey JA, Temple K, Cao L, et al. Self-Assembly of Organometallic Block Copolymers: the Role of Crystallinity of the Core-Forming Polyferrocene Block in the Micellar Morphologies Formed by Poly(ferrocenylsilane-b-Dimethylsiloxane) in n-Alkane Solvents. *J Am Chem Soc*. 2000;122(47):11577-11584. doi:10.1021/ja002205d

32. Mai Y, Eisenberg A. Self-Assembly of Block Copolymers. *Chem Soc Rev*. 2012;41(18):5969. doi:10.1039/c2cs35115c

33. Wang Z, Cao Y, Song J, Xie Z, Wang Y. Cooperation of Amphiphilicity and Crystallization for Regulating the Self-Assembly of Poly(ethylene Glycol)-block-Poly(lactic Acid) Copolymers. *Langmuir*. 2016;32(37):9633-9639. doi:10.1021/acs.langmuir.6b02211

34. Siddiqui N, Asawa S, Birru B, Baadhe R, Rao S. PCL-Based Composite Scaffold Matrices for Tissue Engineering Applications. *Mol Biotechnol 2018 607*. 2018;60(7):506-532. doi:10.1007/S12033-018-0084-5

35. Ducrée J, Koltay P, Zengerle R. *Microfluidics*.; 2006. doi:10.1016/b978-081551497-8.50014-7

36. Li W, Zhang L, Ge X, et al. Microfluidic Fabrication of Microparticles for Biomedical Applications. *Chem Soc Rev*. 2018;47(15):5646-5683. doi:10.1039/c7cs00263g

37. Liu D, Cito S, Zhang Y, Wang C-F, Sikanen T, Santos HA. A Versatile and Robust Microfluidic Platform Toward High Throughput Synthesis of Homogeneous Nanoparticles With Tunable Properties. *Adv Mater*. 2015;27(14):2298-2304. doi:10.1002/adma.201405408

38. Wang J, Chen W, Sun J, et al. A Microfluidic Tubing Method and Its Application for Controlled Synthesis of Polymeric Nanoparticles. *Lab Chip*. 2014;14(10):1673-1677. doi:10.1039/c4lc00080c

39. Khan SA, Duraiswamy S. Controlling Bubbles Using Bubbles—microfluidic Synthesis of Ultra-Small Gold Nanocrystals With Gas-Evolving Reducing Agents. *Lab Chip*. 2012;12(10):1807. doi:10.1039/c2lc21198j

40. Tresset G, Marculescu C, Salonen A, Ni M, Iliescu C. Fine Control Over the Size of Surfactant–Polyelectrolyte Nanoparticles by Hydrodynamic Flow Focusing. *Anal Chem*. 2013;85(12):5850-5856. doi:10.1021/ac4006155

41. Shin Y, Lim YW, Kwak T, et al. Microfluidic Multi-Scale Homogeneous Mixing With Uniform Residence Time Distribution for Rapid Production of Various Metal Core–Shell Nanoparticles. *Adv Funct Mater*. 2020;31(5). doi:10.1002/adfm.202007856

42. Nightingale AM, DeMello JC. Segmented Flow Reactors for Nanocrystal Synthesis. *Adv Mater*. 2012;25(13):1813-1821. doi:10.1002/adma.201203252

43. Xu Z, Lu C, Riordon J, Sinton D, Moffitt MG. Microfluidic Manufacturing of Polymeric Nanoparticles: Comparing Flow Control of Multiscale Structure in Single-Phase Staggered Herringbone and Two-Phase Reactors. *Langmuir*. 2016;32(48):12781-12789. doi:10.1021/acs.langmuir.6b03243

44. Karnik R, Gu F, Basto PA, et al. Microfluidic Platform for Controlled Synthesis of Polymeric Nanoparticles. *Nano Lett*. 2008;8(9):2906-2912. doi:10.1021/nl801736q

45. Feng Q, Sun J, Jiang X. Microfluidics-Mediated Assembly of Functional Nanoparticles for Cancer-Related Pharmaceutical Applications. *Nanoscale*. 2016;8(25):12430-12443. doi:10.1039/c5nr07964k

46. Lim JM, Bertrand N, Valencia PM, et al. Parallel Microfluidic Synthesis of Size-Tunable Polymeric Nanoparticles Using 3D Flow Focusing Towards in Vivo Study. *Nanomedicine Nanotechnol Biol Med*. 2014;10(2):401-409. doi:10.1016/j.nano.2013.08.003

47. Bains A, Cao Y, Moffi tt MG, Bains A, Cao Y, Moffi tt MG. Multiscale Control of Hierarchical Structure in Crystalline Block Copolymer Nanoparticles Using Microfluidics. *Macromol Rapid Commun*. 2015;36(22):2000-2005. doi:10.1002/MARC.201500359

48. Kastner E, Kaur R, Lowry D, Moghaddam B, Wilkinson A, Perrie Y. High-Throughput Manufacturing of Size-Tuned Liposomes by a New Microfluidics Method Using Enhanced Statistical Tools for Characterization. *Int J Pharm*. 2014;477(1-2):361-368. doi:10.1016/j.ijpharm.2014.10.030

49. Kciuk M, Marciniak B, Kontek R. Irinotecan—still an important player in cancer chemotherapy: A comprehensive overview. *Int J Mol Sci*. 2020;21(14):1-21. doi:10.3390/ijms21144919

50. Xu Y, Villalona-Calero MA. Irinotecan: mechanisms of tumor resistance and novel strategies for modulating its activity. *Ann Oncol*. 2002;13(12):1841-1851. doi:10.1093/annonc/mdf337

51. Takimoto CH, Wright J, Arbuck SG. Clinical applications of the camptothecins. *Biochim Biophys Acta*. 1998;1400(1-3):107-119. doi:10.1016/S0167-4781(98)00130-4

52. O'Leary J, Muggia FM. Camptothecins: A review of their development and schedules of administration. *Eur J Cancer*. 1998;34(10):1500-1508. doi:10.1016/S0959-8049(98)00229-9

53. Kawato Y, Aonuma M, Hirota Y, Kuga H, Sato K. Intracellular roles of SN-38, a metabolite of the camptothecin derivative CPT-11, in the antitumor effect of CPT-11. *Cancer Res*. 1991;51(16):4187-4191.

54. Zhao H, Rubio B, Sapra P, et al. Novel Prodrugs of SN38 Using Multiarm Poly(ethylene glycol) Linkers. *Bioconjug Chem*. 2008;19(4):849-859. doi:10.1021/bc700333s

55. Peng CL, Lai PS, Lin FH, Yueh-Hsiu Wu S, Shieh MJ. Dual chemotherapy and photodynamic therapy in an HT-29 human colon cancer xenograft model using SN-38-loaded chlorin-core star block copolymer micelles. *Biomaterials*. 2009;30(21):3614-3625. doi:10.1016/j.biomaterials.2009.03.048048

56. Koizumi F, Kitagawa M, Negishi T, et al. Novel SN-38-incorporating polymeric micelles, NK012, eradicate vascular endothelial growth factor-secreting bulky tumors. *Cancer Res*. 2006;66(20):10048-10056. doi:10.1158/0008-5472.can-06-1605

57. Li SD, Huang L. Pharmacokinetics and biodistribution of nanoparticles. *Mol Pharm*. 2008;5(4):496-504. doi:10.1021/mp800049w

58. Kaimin Cai, Jonathan Yen, Qian Yin, et al. Redox-responsive self-assembled chain-shattering polymeric therapeutics. *Biomater Sci.* 2015;3(7):1061-1065. doi:10.1039/c4bm00452c

59. Abdollahi E, Momtazi AA, Johnston TP, Sahebkar A. Therapeutic effects of curcumin in inflammatory and immune-mediated diseases: A nature-made jack-of-all-trades? *J Cell Physiol*. 2018;233(2):830-848. doi:10.1002/jcp.25778

60. Tomeh MA, Hadianamrei R, Zhao X. A Review of Curcumin and Its Derivatives as Anticancer Agents. *Int J Mol Sci*. 2019;March 1. doi:10.3390/ijms20051033

61. Chen R, Wulff JE, Moffitt MG. Microfluidic Processing Approach to Controlling Drug Delivery Properties of Curcumin-Loaded Block Copolymer Nanoparticles. *Mol Pharm*. Published online September 17, 2018:acs.molpharmaceut.8b00529. doi:10.1021/acs.molpharmaceut.8b00529

62. Silverman L, Bhatti G, Wulff JE, Moffitt MG. Improvements in Drug-Delivery Properties by Co-Encapsulating Curcumin in SN-38-Loaded Anticancer Polymeric Nanoparticles. *Mol Pharm*. 2022;19(6):1866-1881. doi:10.1021/acs.molpharmaceut.2c00005

63. Washington KE, Kularatne RN, Biewer MC, Stefan MC. Combination Loading of Doxorubicin and Resveratrol in Polymeric Micelles for Increased Loading Efficiency and Efficacy. *ACS Biomater Sci Eng*. 2018;4(3):997-1004. doi:10.1021/acsbiomaterials.7b00972

64. Soltantabar P, Calubaquib EL, Mostafavi E, Biewer MC, Stefan MC. Enhancement of Loading Efficiency by Coloading of Doxorubicin and Quercetin in Thermoresponsive Polymeric Micelles. *Biomacromolecules*. 2020;21(4):1427-1436. doi:10.1021/acs.biomac.9b01742

65. Chou T-C, Talalay P. Quantitative analysis of dose-effect relationships: the combined effects of multiple drugs or enzyme inhibitors. *Adv Enzyme Regul*. 1984;22:27-55. doi:10.1016/0065-2571(84)90007-4

66. Chou T-C. Drug Combination Studies and Their Synergy Quantification Using the Chou-Talalay Method. *Cancer Res*. 2010;70(2):440-446. doi:10.1158/0008-5472.can-09-1947

67. Wong PT, Choi S-K. Mechanisms of Drug Release in Nanotherapeutic Delivery Systems. *Chem Rev*. 2015;May 13. doi:10.1021/cr5004634

68. Gupta R, Chen Y, Xie H. In Vitro Dissolution Considerations Associated With Nano Drug Delivery Systems. *Wiley Interdiscip Rev Nanomedicine Nanobiotechnology*. 2021;November 1. doi:10.1002/wnan.1732

69. Bains A, Wulff JE, Moffitt MG. Microfluidic Synthesis of Dye-Loaded Polycaprolactone-block-poly(ethylene oxide) Nanoparticles: Insights into Flow-Directed Loading and In Vitro Release for Drug Delivery. *J Colloid Interface Sci*. 2016;475:136-148. doi:10.1016/j.jcis.2016.04.010

70. Peleg-Shulman T, Gibson D, Cohen R, Abra R, Barenholz Y. Characterization of sterically stabilized cisplatin liposomes by nuclear magnetic resonance. *Biochim Biophys Acta - Biomembr*. 2001;1510(1-2):278-291. doi:10.1016/S0005-2736(00)00359-X

71. Zamboni WC, Gervais AC, Egorin MJ, et al. Systemic and tumor disposition of platinum after administration of cisplatin or STEALTH liposomal-cisplatin formulations (SPI-077 and

SPI-077 B103) in a preclinical tumor model of melanoma. *Cancer Chemother Pharmacol*. 2004;53(4):329-336. doi:10.1007/S00280-003-0719-4

72. Sah E, Sah H. Recent Trends in Preparation of Poly(lactide-co-Glycolide) Nanoparticles by Mixing Polymeric Organic Solution With Antisolvent. *J Nanomater*. 2015;1. doi:10.1155/2015/794601

73. Zhang F, Elsabahy M, Zhang S, Lin LY, Zou J, Wooley KL. Shell crosslinked knedel-like nanoparticles for delivery of cisplatin: effects of crosslinking. *Nanoscale*. 2013;5 8:3220-3225.

74. Elsabahy M, Samarajeewa S, Raymond JE, Clark C, Wooley KL. Shell-crosslinked knedel-like nanoparticles induce lower immunotoxicity than their non-crosslinked analogs. *J Mater Chem B*. 2013;1 39.

75. Zhang K-X, Fang H, Wang Z, Li Z, Taylor J, Wooley KL. Structure-activity relationships of cationic shell-crosslinked knedel-like nanoparticles: shell composition and transfection efficiency/cytotoxicity. *Biomaterials*. 2010;31 7:1805-1813.

76. Shrestha R, Elsabahy M, Florez-Malaver S, Samarajeewa S, Wooley KL. Endosomal escape and siRNA delivery with cationic shell crosslinked knedel-like nanoparticles with tunable buffering capacities. *Biomaterials*. 2012;33 33:8557-8568.

77. Langhans SA. Using 3D in vitro cell culture models in anti-cancer drug discovery. *Expert Opin Drug Discov*. 2021;16(8):841-850. doi:10.1080/17460441.2021.1912731

78. Jensen C, Teng Y. Is It Time to Start Transitioning From 2D to 3D Cell Culture? *Front Mol Biosci*. 2020;7. doi:10.3389/fmolb.2020.00033

79. Bonnans C, Chou J, Werb Z. Remodelling the extracellular matrix in development and disease. *Nat Rev Mol Cell Biol*. 2014;15(12):786-801. doi:10.1038/nrm3904

80. Whitehead KA, Matthews JCF, Chang P, et al. In Vitro – In Vivo Translation of Lipid Nanoparticles for Hepatocellular siRNA Delivery. *ACS Nano*. 2012;6(8):6922-6929. doi:10.1021/nn301922x

81. Nam KT, Smith AST, Lone S, Kwon S, Kim DH. Biomimetic 3D Tissue Models for Advanced High-Throughput Drug Screening. *J Lab Autom*. 2015;June 3. doi:10.1177/2211068214557813

82. Truong WT, Su Y, Meijer JT, Thordarson P, Braet F. Self-Assembled Gels for Biomedical Applications. *Chem - An Asian J*. 2010;January 3. doi:10.1002/asia.201000592

83. Leong DT, Ng KW. Probing the Relevance of 3D Cancer Models in Nanomedicine Research. *Adv Drug Deliv Rev*. 2014;December 1. doi:10.1016/j.addr.2014.06.007

84. Low LA, Mummery C, Berridge BR, Austin CP, Tagle DA. Organs-on-chips: into the next decade. *Nat Rev Drug Discov 2020 205*. 2020;20(5):345-361. doi:10.1038/s41573-020-0079-3

85. Vauthier C, Bouchemal K. Processing and Scale-up of Polymeric Nanoparticles. In: *Processing and Scale-up of Polymeric Nanoparticles*. Springer, Dordrecht; 2011:433-456. doi:10.1007/978-94-007-1248-5_16

86. Yabu H, Higuchi T, Shimomura M. Unique Phase-Separation Structures of Block-Copolymer Nanoparticles. *Adv Mater*. 2005;17(17):2062-2065. doi:10.1002/adma.200500255

87. Patil Y, Toti US, Khdair A, Ma L, Panyam J. Single-Step Surface Functionalization of Polymeric Nanoparticles for Targeted Drug Delivery. *Biomaterials*. 2009;30(5):859-866. doi:10.1016/j.biomaterials.2008.09.056

88. Chen R, Wulff JE, Moffitt MG. Microfluidic Processing Approach to Controlling Drug Delivery Properties of Curcumin-Loaded Block Copolymer Nanoparticles. *Mol Pharm*. 2018;15(10):4517-4528. doi:10.1021/acs.molpharmaceut.8b00529

89. Zhang L, Yu K, Eisenberg A. Ion-Induced Morphological Changes in "Crew-Cut" Aggregates of Amphiphilic Block Copolymers. *Science (80-)*. 1996;272(5269):1777-1779. doi:10.1126/science.272.5269.1777

90. Zhang L, Eisenberg A. Multiple Morphologies of "Crew-Cut" Aggregates of Polystyrene-b-poly(acrylic acid) Block Copolymers. *Science (80-)*. 1995;268(5218):1728-1731. doi:10.1126/science.268.5218.1728

91. Zhang L, Pornpattananangkul D, Hu CMJ, Huang CM. Development of Nanoparticles for Antimicrobial Drug Delivery. *Curr Med Chem*. 2010;17(6):585-594. doi:10.2174/092986710790416290

92. Wang CW, Sinton D, Moffitt MG. Flow-directed block copolymer micelle morphologies via microfluidic self-assembly. *J Am Chem Soc*. 2011;133(46):18853-18864. doi:10.1021/ja2067252

93. Huang Y, Jazani AM, Howell EP, Reynolds LA, Oh JK, Moffitt MG. Microfluidic Shear Processing Control of Biological Reduction Stimuli-Responsive Polymer Nanoparticles for Drug Delivery. *ACS Biomater Sci Eng*. 2020;6(9):5069-5083. doi:10.1021/acsbiomaterials.0C00896

94. Bains A, Cao Y, Kly S, Wulff JE, Moffitt MG. Controlling Structure and Function of Polymeric Drug Delivery Nanoparticles Using Microfluidics. *Mol Pharm*. 2017;14(8):2595-2606. doi:10.1021/acs.molpharmaceut.7b00177

95. Shen H, B AE-TJ of PC, 1999 undefined. Morphological Phase Diagram for a Ternary System of Block Copolymer PS310-b-PAA52/Dioxane/H2O. *ACS Publ*. 1999;103(44):9473-9487. doi:10.1021/jp991365c

96. Schabas G, Wang CW, Oskooei A, Yusuf H, Moffitt MG, Sinton D. Formation and shear-induced processing of quantum dot colloidal assemblies in a multiphase microfluidic chip. *Langmuir*. 2008;24(19):10596-10603. doi:10.1021/la8022985

97. Chawla G, Chaudhary KK. A review of HPLC technique covering its pharmaceutical, environmental, forensic, clinical and other applications. *Int J Pharm Chem Anal*. 6(2):27. doi:10.18231/j.ijpca.2019.006

98. Santoso SB. High-performance liquid chromatography for analytical chemistry. *Innov Heal Soc*. 2021;1(2):33-34. doi:10.31603/ihs.6437

99. Peaston RT, Weinkove C. Measurement of catecholamines and their metabolites. *http://dx.doi.org/101258/000456304322664663*. 2004;41(1):17-38. doi:10.1258/000456304322664663

100. Chorilli M, Bonfilio R, Chicarelli R da S, Salgado HRN. Development and Validation of an Analytical Method by RP-HPLC for Quantification of Sibutramine Hydrochloride in Pharmaceutical Capsules. *Anal Methods*. 2011;3(4):985-990. doi:10.1039/c0ay00598c

101. Welch CJ. Microscale Chiral HPLC in Support of Pharmaceutical Process Research. *Chirality*. 2009;1. doi:10.1002/chir.20625

102. Byrro RMD, César IC, Cardoso FF de S e S, et al. A Rapid and Sensitive HPLC–APCI-MS/MS Method Determination of Fluticasone in Human Plasma: Application for a Bioequivalency Study in Nasal Spray Formulations. *J Pharm Biomed Anal*. 2012;61:38-43. doi:10.1016/j.jpba.2011.11.018

103. Burchard W. Dynamic Light Scattering. In: *Polysaccharide Hydrogels: Characterization and Biomedical Applications*. ; 2016:167-207. doi:10.4032/9789814613620

104. Wang CH, Zhang XQ. Quasielastic Light Scattering Investigation of Concentration Fluctuations and Coupling to Stress Relaxation in a Polymer Solution: Polystyrene in CCl4. *Macromolecules*. 1995;28(7):2288-2296. doi:10.1021/ma00111a024

105. Pine DJ, Weitz DA, Zhu J, Herbolzheimer E. Diffusing-Wave Spectroscopy: Dynamic Light Scattering in the Multiple Scattering Limit. *J Phys*. 1990;51(18):2101-2127. doi:10.1051/jphys:0199000510180210100

106. Franks K, Kestens V, Braun A, Roebben G, Linsinger TPJ. Non-Equivalence of Different Evaluation Algorithms to Derive Mean Particle Size From Dynamic Light Scattering Data. *J Nanoparticle Res*. 2019;21(9). doi:10.1007/s11051-019-4630-2

107. Dahmen U, Erni R, Radmilovic V, Ksielowski C, Rossell M-D, Denes P. Background, Status and Future of the Transmission Electron Aberration-Corrected Microscope Project. *Philos Trans R Soc a Math Phys Eng Sci*. 2009;367(1903):3795-3808. doi:10.1098/rsta.2009.0094

108. Koster AJ, Ziese U, Verkleij AJ, Janssen AH, Jong KP de. Three-Dimensional Transmission Electron Microscopy: a Novel Imaging and Characterization Technique With Nanometer Scale Resolution for Materials Science. *J Phys Chem B*. 2000;104(40):9368-9370. doi:10.1021/jp0015628

109. Alem N, Yazyev O V, Kisielowski C, et al. Probing the Out-of-Plane Distortion of Single Point Defects in Atomically Thin Hexagonal Boron Nitride at the Picometer Scale. *Phys Rev Lett*. 2011;106(12). doi:10.1103/physrevlett.106.126102

110. Chomsaeng N, Haruta M, Chairuangsri T, Kurata H, Isoda S, Shiojiri M. HRTEM and ADF-STEM of Precipitates at Peak-Ageing in Cast A356 Aluminium Alloy. *J Alloys Compd*. 2010;496(1-2):478-487. doi:10.1016/j.jallcom.2010.02.084

111. Carlo S De, Harris JR. Negative Staining and Cryo-Negative Staining of Macromolecules and Viruses for TEM. *Micron*. 2011;February. doi:10.1016/j.micron.2010.06.003

112. Jung MW, Mun JY. Sample Preparation and Imaging of Exosomes by Transmission Electron Microscopy. *J Vis Exp*. 2018;2018(131). doi:10.3791/56482

113. Liu LZ, Yu W, Seitsonen J, Lehto V-P, Lehto V-P. Correct Identification of the Core-Shell Structure of Cell Membrane-Coated Polymeric Nanoparticles. *Chem - A Eur J*. 2022;28(68). doi:10.1002/chem.202200947

114. Baxa U. Preparation of Liposomes for Negative Staining TEM. In: *Microscopy and Microanalysis*. ; 2020. doi:10.1017/s1431927620020401

115. Qi R, Shen M, Cao X, et al. Exploring the Dark Side of MTT Viability Assay of Cells Cultured Onto Electrospun PLGA-based Composite Nanofibrous Scaffolding Materials. *Analyst*. 2011;136(14):2897-2903. doi:10.1039/c0an01026j

116. Fuente-Herreruela D de la, Monnappa AK, Muñoz-Úbeda M, et al. Lipid–peptide Bioconjugation Through Pyridyl Disulfide Reaction Chemistry and Its Application in Cell Targeting and Drug Delivery. *J Nanobiotechnology*. 2019;17(1). doi:10.1186/s12951-019-0509-8

117. Bonnier F, Keating M, Wróbel T, Majzner K, Baranska M, Blanco, A BH. Cell Viability Assessment Using the Alamar Blue Assay: A Comparison of 2D and 3D Cell Culture Models. *Toxicol Vitr*. 2015;29(1):124-131. doi:10.1016/j.tiv.2014.09.014

118. Wang F, Wang Z, Gu X, Cui J. miR-940 Upregulation Suppresses Cell Proliferation and Induces Apoptosis by Targeting PKC- In Ovarian Cancer OVCAR3 Cells. *Oncol Res Featur Preclin Clin Cancer Ther*. 2017;25(1):107-114. doi:10.3727/096504016x14732772150145

119. Liu X, Huang J. Scoparone Inhibits the Growth of Liver Cancer Cells by Regulating MAPK Signaling Pathway. *Trop J Pharm Res*. 2022;21(10):2093-2098. doi:10.4314/tjpr.v21i10.8

120. Cao Y, Silverman L, Lu C, Hof R, Wulff JE, Moffitt MG. Microfluidic Manufacturing of SN-38-Loaded Polymer Nanoparticles with Shear Processing Control of Drug Delivery Properties. *Mol Pharm*. 2019;16(1):96-107. doi:10.1021/acs.molpharmaceut.8b00874

121. Huang Y, Moini Jazani A, Howell EP, Oh JK, Moffitt MG. Controlled Microfluidic Synthesis of Biological Stimuli-Responsive Polymer Nanoparticles. *ACS Appl Mater Interfaces*. 2020;12(1):177-190. doi:10.1021/acsami.9b17101

122. Xu Z, Lu C, Lindenberger C, Cao Y, Wulff JE, Moffitt MG. Synthesis, Self-Assembly, and Drug Delivery Characteristics of Poly(methyl caprolactone- *co* -caprolactone)- *b* -poly(ethylene oxide) Copolymers with Variable Compositions of Hydrophobic Blocks: Combining Chemistry and Microfluidic Processing for Polymeric Nanomedicines. *ACS Omega*. 2017;2(8):5289-5303. doi:10.1021/acsomega.7b00829

123. Aslantürk ÖS. In Vitro Cytotoxicity and Cell Viability Assays: Principles, Advantages, and Disadvantages. In: *Genotoxicity - A Predictable Risk to Our Actual World*. ; 2018. doi:10.5772/intechopen.71923

124. Matsumoto Y, Ibrahim OM. Application of in Vivo Confocal Microscopy in Dry Eye Disease. *Investig Opthalmology Vis Sci*. 2018;59(14 Special Issue):DES41-DES47. doi:10.1167/iovs.17-23602

125. Takeuchi K, Frank JA. Confocal Microscopy and Microbial Viability Detection for Food Research. *J Food Prot*. 2001;1. doi:10.4315/0362-028x-64.12.2088

126. Reihani SNS, Oddershede LB. Confocal Microscopy of Thick Specimens. *J Biomed Opt*. 2009;14(3):030513. doi:10.1117/1.3156813

127. Royall CP, Louis AA, Tanaka H. Measuring Colloidal Interactions With Confocal Microscopy. *J Chem Phys*. 2007;127(4). doi:10.1063/1.2755962

128. Thiberville L, Salaün M, Lachkar S, et al. Human in Vivo Fluorescence Microimaging of the Alveolar Ducts and Sacs During Bronchoscopy. *Eur Respir J*. 2009;33(5):974-985. doi:10.1183/09031936.00083708

129. Elliott AD. Confocal Microscopy: Principles and Modern Practices. *Curr Protoc Cytom*. 2019;92(1). doi:10.1002/cpcy.68

130. Garnier G, Chan DYC, Grieser F, Dagastine RR. Anomalous Stability of Carbon Dioxide in pH-Controlled Bubble Coalescence. *Angew Chemie*. 2011;123(15):3516-3518. doi:10.1002/ange.201006552

131. Tabor RF, Lockie H, Mair DD, et al. Combined AFM−Confocal Microscopy of Oil Droplets: Absolute Separations and Forces in Nanofilms. *J Phys Chem Lett*. 2011;2(9):961-965. doi:10.1021/jz2003606

132. Hell SW, Reiner G, Cremer C, Stelzer EHK. Aberrations in Confocal Fluorescence Microscopy Induced by Mismatches in Refractive Index. *J Microsc*. 1993;169(3):391-405. doi:10.1111/j.1365-2818.1993.tb03315.x

133. Vakarelski IU, Manica R, Tang X-S, et al. Dynamic Interactions Between Microbubbles in Water. *Proc Natl Acad Sci*. 2010;107(25):11177-11182. doi:10.1073/pnas.1005937107

134. Govindan S V., Cardillo TM, Rossi EA, et al. Improving the therapeutic index in cancer therapy by using antibody-drug conjugates designed with a moderately cytotoxic drug. *Mol Pharm*. 2015;12(6):1836-1847. doi:10.1021/MP5006195

135. Palakurthi S. Challenges in SN38 drug delivery: Current success and future directions. *Expert Opin Drug Deliv*. 2015;12(12):1911-1921. doi:10.1517/17425247.2015.1070142

136. Lee Costich T, Carie A, Edward Semple J, et al. IT-143, A Polymer Micelle Nanoparticle, Widens Therapeutic Window of Daunorubicin. *Pharm Nanotechnol*. 2016;4(1):3-15. doi:10.2174/2211738504666160310002348

137. Khurana A, Tekula S, Saifi MA, Venkatesh P, Godugu C. Therapeutic applications of selenium nanoparticles. *Biomed Pharmacother*. 2019;111:802-812. doi:10.1016/J.BIOPHA.2018.12.146

138. Banskota S, Saha S, Bhattacharya J, et al. Genetically Encoded Stealth Nanoparticles of a Zwitterionic Polypeptide-Paclitaxel Conjugate Have a Wider Therapeutic Window than Abraxane in Multiple Tumor Models. *Nano Lett*. 2020;20(4). doi:10.1021/ACS.NANOLETT.9B05094

139. Peikov V, Ugwu S, Parmar M, Zhang A, Ahmad I. pH-dependent association of SN-38 with lipid bilayers of a novel liposomal formulation. *Int J Pharm*. 2005;299(1-2):92-99. doi:10.1016/J.IJPHARM.2005.04.028

140. Sadat SMA, Vakili MR, Paiva IM, Weinfeld M, Lavasanifar A. Development of Self-Associating SN-38-Conjugated Poly(ethylene oxide)-Poly(ester) Micelles for Colorectal Cancer Therapy. *Pharmaceutics*. 2020;12(11):1033. doi:10.3390/pharmaceutics12111033

141. Dimchevska S, Geskovski N, Koliqi R, et al. Efficacy assessment of self-assembled PLGA-PEG-PLGA nanoparticles: Correlation of nano-bio interface interactions, biodistribution,

internalization and gene expression studies. *Int J Pharm*. 2017;533(2):389-401. doi:10.1016/j.ijpharm.2017.05.054

142. Ebrahimnejad P, Dinarvand R, Sajadi A, et al. Preparation and in vitro evaluation of actively targetable nanoparticles for SN-38 delivery against HT-29 cell lines. *Nanomedicine Nanotechnology, Biol Med*. 2010;6(3):478-485. doi:10.1016/j.nano.2009.10.003

143. Wang Y, Guo M, Lu Y, et al. Alpha-tocopheryl polyethylene glycol succinate-emulsified poly(lactic-co-glycolic acid) nanoparticles for reversal of multidrug resistance in vitro. *Nanotechnology*. 2012;23(49). doi:10.1088/0957-4484/23/49/495103

144. Carie A, Rios-Doria J, Costich T, et al. IT-141, a Polymer Micelle Encapsulating SN-38, Induces Tumor Regression in Multiple Colorectal Cancer Models. *J Drug Deliv*. 2011;2011:1-9. doi:10.1155/2011/869027

145. Sepehri N, Rouhani H, Tavassolian F, et al. SN38 polymeric nanoparticles: In vitro cytotoxicity and in vivo antitumor efficacy in xenograft balb/c model with breast cancer versus irinotecan. *Int J Pharm*. 2014;471(1-2):485-497. doi:10.1016/j.ijpharm.2014.05.046

146. Essa S, Daoud J, Lafleur M, Martel S, Tabrizian M. SN-38 active loading in poly(lactic-co-glycolic acid) nanoparticles and assessment of their anticancer properties on COLO-205 human colon adenocarcinoma cells. *J Microencapsul*. 2015;32(8):784-793. doi:10.3109/02652048.2015.1081416

147. Mehdizadeh M, Rouhani H, Sepehri N, et al. Biotin decorated PLGA nanoparticles containing SN-38 designed for cancer therapy. *Artif cells, nanomedicine, Biotechnol*. 2017;45(3):495-504. doi:10.1080/21691401.2016.1178130

148. Taghavi S, Abnous K, Babaei M, Taghdisi SM, Ramezani M, Alibolandi M. Synthesis of chimeric polymersomes based on PLA-b-PHPMA and PCL-b-PHPMA for nucleoline guided

delivery of SN38. *Nanomedicine Nanotechnology, Biol Med*. 2020;28:102227. doi:10.1016/j.nano.2020.102227

149. Lee M, Cho YW, Park JH, et al. Size control of self-assembled nanoparticles by an emulsion/solvent evaporation method. *Colloid Polym Sci*. 2006;284(5):506-512. doi:10.1007/s00396-005-1413-3

150. Elsabahy M, Wooley KL. Design of polymeric nanoparticles for biomedical delivery applications. *Chem Soc Rev*. 2012;41(7):2545-2561. doi:10.1039/C2CS15327K

151. Alferiev IS, Iyer R, Croucher JL, et al. Nanoparticle-mediated delivery of a rapidly activatable prodrug of SN-38 for neuroblastoma therapy. *Biomaterials*. 2015;51:22-29. doi:10.1016/j.biomaterials.2015.01.075

152. Sumitomo M, Koizumi F, Asano T, et al. Novel SN-38-incorporated polymeric micelle, NK012, strongly suppresses renal cancer progression. *Cancer Res*. 2008;68(6):1631-1635. doi:10.1158/0008-5472.CAN-07-6532

153. Matsumura Y. Preclinical and clinical studies of NK012, an SN-38-incorporating polymeric micelles, which is designed based on EPR effect. *Adv Drug Deliv Rev*. 2011;63(3):184-192. doi:10.1016/J.ADDR.2010.05.008

154. Fang X, Gao K, Huang J, et al. Molecular level precision and high molecular weight peptide dendrimers for drug-specific delivery. *J Mater Chem B*. 2021;9(41):8594-8603. doi:10.1039/D1TB01157J

155. Xiang J, Wu B, Zhou Z, et al. Synthesis and evaluation of a paclitaxel-binding polymeric micelle for efficient breast cancer therapy. *Sci China Life Sci*. 2018;61(4):436-447. doi:10.1007/S11427-017-9274-9

156. Capretto L, Carugo D, Mazzitelli S, Nastruzzi C, Zhang X. Microfluidic and lab-on-a-chip preparation routes for organic nanoparticles and vesicular systems for nanomedicine applications. *Adv Drug Deliv Rev*. 2013;65(11-12):1496-1532. doi:10.1016/J.ADDR.2013.08.002

157. Morikawa Y, Tagami T, Hoshikawa A, Ozeki T. The Use of an Efficient Microfluidic Mixing System for Generating Stabilized Polymeric Nanoparticles for Controlled Drug Release. *Biol Pharm Bull*. 2018;41(6):899-907. doi:10.1248/BPB.B17-01036

158. Abstiens K, Goepferich AM. Microfluidic manufacturing improves polydispersity of multicomponent polymeric nanoparticles. *J Drug Deliv Sci Technol*. 2019;49:433-439. doi:10.1016/J.JDDST.2018.12.009

159. Wang CW, Bains A, Sinton D, Moffitt MG. Flow-directed loading of block copolymer micelles with hydrophobic probes in a gas-liquid microreactor. *Langmuir*. 2013;29(26):8385-8394. doi:10.1021/LA400011N

160. Xu Z, Yan B, Riordon J, Zhao Y, Sinton D, Moffitt MG. Microfluidic Synthesis of Photoresponsive Spool-Like Block Copolymer Nanoparticles: Flow-Directed Formation and Light-Triggered Dissociation. *Chem Mater*. 2015;27(23):8094-8104. doi:10.1021/acs.chemmater.5B03800

161. Hu S, Lee E, Wang C, et al. Amphiphilic drugs as surfactants to fabricate excipient-free stable nanodispersions of hydrophobic drugs for cancer chemotherapy. *J Control Release*. 2015;220:175-179. doi:10.1016/j.jconrel.2015.10.031

162. Yang Q, Tan T, Zhao J, et al. A reversible decomposition approach for the formation of injectable, excipient-free, self-assembling nanocrystals. *Chem Commun*. 2019;55(21):3144-3147. doi:10.1039/C8CC10191D

163. Hu S, Dong C, Wang J, et al. Assemblies of indocyanine green and chemotherapeutic drug to cure established tumors by synergistic chemo-photo therapy. *J Control Release*. 2020;324:250-259. doi:10.1016/j.jconrel.2020.05.018

164. Martínez Rivas CJ, Tarhini M, Badri W, et al. Nanoprecipitation process: From encapsulation to drug delivery. *Int J Pharm*. 2017;532(1):66-81. doi:10.1016/j.ijpharm.2017.08.064

165. Zhang Y, Chan HF, Leong KW. Advanced materials and processing for drug delivery: The past and the future. *Adv Drug Deliv Rev*. 2013;65(1):104-120. doi:10.1016/j.addr.2012.10.003

166. Djurdjic B, Dimchevska S, Geskovski N, et al. Synthesis and self-assembly of amphiphilic poly(acrylicacid)-poly(ε)-poly(acrylicacid) block copolymer as novel carrier for 7-ethyl-10-hydroxy camptothecin. *J Biomater Appl*. 2015;29(6):867-881. doi:10.1177/0885328214549612

167. Dimchevska S, Geskovski N, Petruševski G, et al. SN-38 loading capacity of hydrophobic polymer blend nanoparticles: formulation, optimization and efficacy evaluation. *Drug Dev Ind Pharm*. 2017;43(3):502-510. doi:10.1080/03639045.2016.1268151

168. Dimchevska S, Geskovski N, Petruševski G, et al. SN-38 loading capacity of hydrophobic polymer blend nanoparticles: formulation, optimization and efficacy evaluation. *Drug Dev Ind Pharm*. 2017;43(3):502-510. doi:10.1080/03639045.2016.1268151

169. He X, Cao Z, Li N, et al. Preparation and evaluation of SN-38-loaded MMP-2-responsive polymer micelles. *J Drug Deliv Sci Technol*. 2021;66:102596. doi:10.1016/J.JDDST.2021.102596

170. Wan X, Beaudoin JJ, Vinod N, et al. Co-delivery of paclitaxel and cisplatin in poly(2-oxazoline) polymeric micelles: Implications for drug loading, release, pharmacokinetics and outcome of ovarian and breast cancer treatments. *Biomaterials*. 2019;192:1-14. doi:10.1016/j.biomaterials.2018.10.032

171. Hamzehzadeh L, Atkin SL, Majeed M, Butler AE, Sahebkar A. The versatile role of curcumin in cancer prevention and treatment: A focus on PI3K/AKT pathway. *J Cell Physiol*. 2018;233(10):6530-6537. doi:10.1002/jcp.26620

172. Li Y, Xiao P, Huang Z, et al. Evaluation of curcumin-mediated photodynamic therapy on the reverse of multidrug resistance in tumor cells. *RSC Adv*. 2019;10(1):298-306. doi:10.1039/c9ra09996d

173. Pajaniradje S, Mohankumar K, Radhakrishnan R, et al. Indole Curcumin Reverses Multidrug Resistance by Reducing the Expression of ABCB1 and COX2 in Induced Multidrug Resistant Human Lung Cancer Cells. *Lett Drug Des Discov*. 2020;17(9):1146-1154. doi:10.2174/1570180817666200402124503

174. Mignani S, Bryszewska M, Klajnert-Maculewicz B, Zablocka M, Majoral J-P. Advances in Combination Therapies Based on Nanoparticles for Efficacious Cancer Treatment: An Analytical Report. *Biomacromolecules*. 2015;16(1):1-27. doi:10.1021/bm501285t

175. Wong S, Zhao J, Cao C, et al. Just add sugar for carbohydrate induced self-assembly of curcumin. *Nat Commun*. 2019;10(1):1-9. doi:10.1038/s41467-019-08402-y

176. Lopes LMF, Garcia AR, Brogueira P, Ilharco LM. Interactions between DNA purines and ruthenium ammine complexes within nanostructured sol-gel silica matrixes. *J Phys Chem B*. 2010;114(11):3987-3998. doi:10.1021/JP9080542

177. Vitorino C, Almeida J, Gonçalves LM, Almeida AJ, Sousa JJ, Pais AACC. Co-encapsulating nanostructured lipid carriers for transdermal application: From experimental design to the molecular detail. *J Control Release*. 2013;167(3):301-314. doi:10.1016/J.JCONREL.2013.02.011

178. Tzeli D, Theodorakopoulos G, Petsalakis ID, Ajami D, Rebek J. Theoretical study of hydrogen bonding in homodimers and heterodimers of amide, boronic acid, and carboxylic acid, free and in encapsulation complexes. *J Am Chem Soc*. 2011;133(42):16977-16985. doi:10.1021/JA206555D

179. Guo Q, Shu X, Hu Y, et al. Formulated protein-polysaccharide-surfactant ternary complexes for co-encapsulation of curcumin and resveratrol: Characterization, stability and in vitro digestibility. *Food Hydrocoll*. 2021;111:106265. doi:10.1016/J.FOODHYD.2020.106265

180. Goel A, Jhurani S, Aggarwal BB. Multi-targeted therapy by curcumin: how spicy is it? *Mol Nutr Food Res*. 2008;52(9):1010-1030. doi:10.1002/MNFR.200700354

181. Shang L, Nienhaus K, Nienhaus GU. Engineered nanoparticles interacting with cells: size matters. *J Nanobiotechnology*. 2014;12(1). doi:10.1186/1477-3155-12-5

182. Danaei M, Dehghankhold M, Ataei S, et al. Impact of Particle Size and Polydispersity Index on the Clinical Applications of Lipidic Nanocarrier Systems. *Pharmaceutics*. 2018;10(2). doi:10.3390/pharmaceutics10020057

183. Jo DH, Kim JH, Lee TG, Kim JH. Size, surface charge, and shape determine therapeutic effects of nanoparticles on brain and retinal diseases. *Nanomedicine*. 2015;11(7):1603-1611. doi:10.1016/j.nano.2015.04.015

184. Zhao J, Stenzel MH. Entry of nanoparticles into cells: the importance of nanoparticle properties. *Polym Chem*. 2018;9(3):259-272. doi:10.1039/C7PY01603D

185. Sanità G, Carrese B, Lamberti A. Nanoparticle Surface Functionalization: How to Improve Biocompatibility and Cellular Internalization. *Front Mol Biosci*. 2020;7:587012. doi:10.3389/fmolb.2020.587012

186. Ahmad F, Salem-Bekhit MM, Khan F, et al. Unique Properties of Surface-Functionalized Nanoparticles for Bio-Application: Functionalization Mechanisms and Importance in Application. *Nanomaterials*. 2022;12(8). doi:10.3390/nano12081333

187. Upadhyay K, Tamrakar RK, Thomas S, Kumar M. Surface functionalized nanoparticles: A boon to biomedical science. *Chem Biol Interact*. 2023;380. doi:10.1016/j.cbi.2023.110537

188. Bruckman MA, Randolph LN, VanMeter A, et al. Biodistribution, Pharmacokinetics, and Blood Compatibility of Native and PEGylated Tobacco Mosaic Virus Nano-Rods and -Spheres in Mice. *Virology*. 2014;449:163-173. doi:10.1016/j.virol.2013.10.035

189. Maisha N, Naik N, Okesola M, et al. Engineering PEGylated Polyester Nanoparticles to Reduce Complement-Mediated Infusion Reaction. *Bioconjug Chem*. 2021;32(10):2154-2166. doi:10.1021/acs.bioconjchem.1c00339

190. Thiruppathi R, Mishra S, Ganapathy M, et al. Nanoparticle Functionalization and Its Potentials for Molecular Imaging. *Adv Sci*. 2017;4(3):1600279. doi:10.1002/advs.201600279

191. Samuelsson E, Shen H, Blanco E, Ferrari M, Wolfram J. Contribution of Kupffer Cells to Liposome Accumulation in the Liver. *Colloids Surfaces B Biointerfaces*. 2017;158:356-362. doi:10.1016/j.colsurfb.2017.07.014

192. Tian G, Pan R, Zhang B, et al. Liver-Targeted Combination Therapy Basing on Glycyrrhizic Acid-Modified DSPE-PEG-PEI Nanoparticles for Co-delivery of Doxorubicin and Bcl-2 siRNA. *Front Pharmacol*. 2019;9(JAN). doi:10.3389/fphar.2019.00004

193. Zhang Y, Wang Y, Xin Q, et al. Zwitterionic choline phosphate conjugated folate-poly (ethylene glycol): a general decoration of erythrocyte membrane-coated nanoparticles for enhanced tumor-targeting drug delivery. *J Mater Chem B*. 2022;10(14):2497-2503. doi:10.1039/d1tb02493k

194. Zhang L, Zhu S, Qian L, Pei Y, Qiu Y, Jiang Y. RGD-modified PEG-PAMAM-DOX conjugates: in vitro and in vivo studies for glioma. *Eur J Pharm Biopharm*. 2011;79(2):232-240. doi:10.1016/j.ejpb.2011.03.025

195. Latronico T, Valente G, Fanizza E, et al. Cytotoxicity Study on Luminescent Nanocrystals Containing Phospholipid Micelles in Primary Cultures of Rat Astrocytes. *PLoS One*. 2016;11(4). doi:10.1371/journal.pone.0153451

196. Ojea-Jiménez I, Puntes VF. Instability of Cationic Gold Nanoparticle Bioconjugates: The Role of Citrate Ions. *J Am Chem Soc*. 2009;131(37):13320-13327. doi:10.1021/ja902894s

197. Veiseh O, Sun C, Gunn J, et al. Optical and MRI Multifunctional Nanoprobe for Targeting Gliomas. *Nano Lett*. 2005;5(6):1003-1008. doi:10.1021/nl0502569

198. Gu H, Xu K, Xu C, Xu B. Biofunctional Magnetic Nanoparticles for Protein Separation and Pathogen Detection. *Chem Commun*. 2006;9(1):941. doi:10.1039/b514130c

199. Harvey S, Ng DYW, Szelwicka J, et al. Facile Synthesis of Ultrasmall Polydopamine-Polyethylene Glycol Nanoparticles for Cellular Delivery. *Biointerphases*. 2018;13(6). doi:10.1116/1.5042640

200. Kandel PK, Fernando LP, Ackroyd PC, Christensen KA. Incorporating Functionalized Polyethylene Glycol Lipids Into Reprecipitated Conjugated Polymernanoparticles for Bioconjugation and Targeted Labeling of Cells. *Nanoscale*. 2011;3(3):1037-1045. doi:10.1039/c0nr00746c

201. Yoshimoto K, Hirase T, Nemoto S, Hatta T, Nagasaki Y. Facile Construction of Sulfanyl-Terminated Poly(ethylene Glycol)-Brushed Layer on a Gold Surface for Protein Immobilization by the Combined Use of Sulfanyl-Ended Telechelic and Semitelechelic Poly(ethylene Glycol)s. *Langmuir*. 2008;24(17):9623-9629. doi:10.1021/la8012798

202. Otsuka H, Akiyama Y, Nagasaki Y, Kataoka K. Quantitative and Reversible Lectin-Induced Association of Gold Nanoparticles Modified With A-Lactosyl-Ω-Mercapto-Poly(ethylene Glycol). *J Am Chem Soc*. 2001;123(34):8226-8230. doi:10.1021/ja010437m

203. Otsuka H, Nagasaki Y, Kataoka K. Characterization of Aldehyde-Peg Tethered Surfaces: Influence of PEG Chain Length on the Specific Biorecognition. *Langmuir*. 2004;20(26):11285-11287. doi:10.1021/la0483414

204. Akiyama Y, Otsuka H, Nagasaki Y, Kato M, Kataoka K. Selective Synthesis of Heterobifunctional Poly(ethylene Glycol) Derivatives Containing Both Mercapto and Acetal Terminals. *Bioconjug Chem*. 2000;11(6):947-950. doi:10.1021/bc000034w

205. Jia F, Liu X, Li L, Mallapragada S, Narasimhan B, Wang Q. Multifunctional nanoparticles for targeted delivery of immune activating and cancer therapeutic agents. *J Control Release*. 2013;172(3):1020-1034. doi:10.1016/j.jconrel.2013.10.012

206. Carter T, Mulholland P, Chester K. Antibody-targeted nanoparticles for cancer treatment. *Immunotherapy*. 2016;8(8):941-958. doi:10.2217/imt.16.11

207. Samarajeewa S, Ibri\vcević A, Gunsten SP, et al. Degradable cationic shell cross-linked knedel-like nanoparticles: synthesis, degradation, nucleic acid binding, and in vitro evaluation. *Biomacromolecules*. 2013;14 4:1018-1027.

208. Chen R, Wulff JE, Moffitt MG. Microfluidic Processing Approach to Controlling Drug Delivery Properties of Curcumin-Loaded Block Copolymer Nanoparticles. *Mol Pharm*. 2018;15(10):4517-4528. doi:10.1021/acs.molpharmaceut.8b00529

209. Lin S, Feng S, Mo Y, et al. Dual-responsive crosslinked micelles of a multifunctional graft copolymer for drug delivery applications. *J Polym Sci Part A Polym Chem*. 2017;55(9):1536-1546. doi:10.1002/POLA.28520

210. Park J-W, Lee J, Park S-H, Kim K-S. Optimizing a Three-Dimensional Spheroid Clearing Method for the Imaging-Based Evaluation of Cardiotoxicity. *Organoid*. 2021;1:e7. doi:10.51335/organoid.2021.1.e7

211. Horning JL, Sahoo SK, Vijayaraghavalu S, et al. 3-D Tumor Model For In Vitro Evaluation of Anticancer Drugs. *Mol Pharm*. 2008;5(5):849-862. doi:10.1021/mp800047v

212. Hongisto V, Jernström S, Fey V, et al. High-Throughput 3D Screening Reveals Differences in Drug Sensitivities Between Culture Models of JIMT1 Breast Cancer Cells. *PLoS One*. 2013;8(10). doi:10.1371/journal.pone.0077232

213. Kloker LD, Yurttas C, Lauer UM. Three-Dimensional Tumor Cell Cultures Employed in Virotherapy Research. *Oncolytic Virotherapy*. 2018;7:79-93. doi:10.2147/ov.s165479

214. Mohandas S, Gayatri V, Kumaran K, Gopinath V, Paulmurugan R, Ramkumar KM. New Frontiers in Three-Dimensional Culture Platforms to Improve Diabetes Research. *Pharmaceutics*. 2023;March 1. doi:10.3390/pharmaceutics15030725

215. Oh E-T, Kim H-J, Choi M, et al. Multi-Layer Nanofibrous PCL Scaffold-Based Colon Cancer Cell Cultures to Mimic Hypoxic Tumor Microenvironment for Bioassay. *Cancers (Basel)*. 2021;13(14). doi:10.3390/cancers13143550

216. Seyfoori A, Samiei E, Jalili N, et al. Self-Filling Microwell Arrays (SFMAs) for Tumor Spheroid Formation. *Lab Chip*. 2018;18(22):3516-3528. doi:10.1039/C8LC00708J

217. Zuppinger C. 3D Cardiac Cell Culture: A Critical Review of Current Technologies and Applications. *Front Cardiovasc Med*. 2019;June 26. doi:10.3389/fcvm.2019.00087

218. Zeng W, Ning Y, Huang X. Advanced Technologies in Periodontal Tissue Regeneration Based on Stem Cells: Current Status and Future Perspectives. *J Dent Sci*. 2021;January 1. doi:10.1016/j.jds.2020.07.008

219. Koch J, Mönch D, Maaß A, et al. Three Dimensional Cultivation Increases Chemo- And Radioresistance of Colorectal Cancer Cell Lines. *PLoS One*. 2021;16(1). doi:10.1371/journal.pone.0244513

220. He J, Zhou CS, Xu X, et al. Scalable Formation of Highly Viable and Functional Hepatocellular Carcinoma Spheroids in an Oxygen-Permeable Microwell Device for Anti-Tumor Drug Evaluation. *Adv Healthc Mater*. 2022;11(18). doi:10.1002/adhm.202200863

221. Liu T, Chien C-C, Parkinson L, Thierry B. Advanced Micromachining of Concave Microwells for Long Term on-Chip Culture of Multicellular Tumor Spheroids. *ACS Appl Mater Interfaces*. 2014;6(11):8090-8097. doi:10.1021/am500367h

222. Paolillo M, Comincini S, Schinelli S. In Vitro Glioblastoma Models: A Journey Into the Third Dimension. *Cancers (Basel)*. 2021;13(10):2449. doi:10.3390/cancers13102449

223. Breslin S, O'Driscoll L. The Relevance of Using 3D Cell Cultures, in Addition to 2D Monolayer Cultures, When Evaluating Breast Cancer Drug Sensitivity and Resistance. *Oncotarget*. 2016;7(29):45745-45756. doi:10.18632/oncotarget.9935

224. Casey JF, Yue X, Nguyen TT, et al. 3D Hydrogel-Based Microwell Arrays as a Tumor Microenvironment Model to Study Breast Cancer Growth. *Biomed Mater*. 2017;12(2):025009. doi:10.1088/1748-605x/aa5d5c

225. Mirab F, Kang YJ, Majd S. Preparation and Characterization of Size-Controlled Glioma Spheroids Using Agarose Hydrogel Microwells. *PLoS One*. 2019;14(1). doi:10.1371/journal.pone.0211078

226. Mobasheri A, Navaei A, Mirani B, et al. Bioprinting Technologies for Disease Modeling. *Biotechnol Lett*. 2017;September. doi:10.1007/s10529-017-2360-z

227. Carr GJ, Gorelick NJ. Statistical Design and Analysis of Mutation Studies in Transgenic Mice. *Environ Mol Mutagen*. 1995;25(3):246-255. doi:10.1002/EM.2850250311

228. Daublain P, Feng KI, Altman MD, et al. Analyzing the Potential Root Causes of Variability of Pharmacokinetics in Preclinical Species. *Mol Pharm*. 2017;14(5):1634-1645. doi:10.1021/acs.molpharmaceut.6b01118

229. Ritz C, Baty F, Streibig JC, Gerhard D. Dose-Response Analysis Using R. *PLoS One*. 2015;10(12). doi:10.1371/JOURNAL.PONE.0146021

230. Barry J, Fritz M, Brender JR, Smith PES, Lee DH, Ramamoorthy A. Determining the Effects of Lipophilic Drugs on Membrane Structure by Solid-State NMR Spectroscopy: The Case of the Antioxidant Curcumin. *J Am Chem Soc*. 2009;131(12):4490-4498. doi:10.1021/ja809217u

231. Duda M, Cygan K, Wiśniewska-Becker A. Effects of Curcumin on Lipid Membranes: An EPR Spin-Label Study. *Cell Biochem Biophys*. 2020;78(2):139-147. doi:10.1007/s12013-020-00906-5

232. Ileri-Ercan N. Understanding Interactions of Curcumin With Lipid Bilayers: A Coarse-Grained Molecular Dynamics Study. *J Chem Inf Model*. 2019;59(10):4413-4426. doi:10.1021/acs.jcim.9b00650

233. Jin L, Xie N, Luo P, Gao W, Tu P, Jiang Y. Establishment and Large-Scale Validation of a Three-Dimensional Tumor Model on an Array Chip for Anticancer Drug Evaluation. *Front Pharmacol*. 2022;13. doi:10.3389/fphar.2022.1032975

234. Guo H, Liu D, Gao B, et al. Antiproliferative Activity and Cellular Uptake of Evodiamine and Rutaecarpine Based on 3D Tumor Models. *Molecules*. 2016;21(7). doi:10.3390/molecules21070954

235. Durbin KR, Nottoli MS, Jenkins GJ. Effects of Microtubule-Inhibiting Small Molecule and Antibody-Drug Conjugate Treatment on Differentially-Sized A431 Squamous Carcinoma Spheroids. *Sci Rep*. 2020;10(1). doi:10.1038/s41598-020-57789-y

236. Jäntti M, Talman V, Räsänen K, Tarvainen I, Koistinen H, Tuominen RK. Anticancer Activity of the Protein Kinase C Modulator HMI -1a3 in 2D and 3D Cell Culture Models of Androgen-responsive and Androgen-unresponsive Prostate Cancer. *FEBS Open Bio*. 2018;8(5):817-828. doi:10.1002/2211-5463.12419

237. Tong R, Chiang HH, Kohane DS. Photoswitchable Nanoparticles for in Vivo Cancer Chemotherapy. *Proc Natl Acad Sci*. 2013;110(47):19048-19053. doi:10.1073/pnas.1315336110

238. Patel J, Spiller S, Barker E. Drug Penetration in Pediatric Brain Tumors: Challenges and Opportunities. *Pediatr Blood Cancer*. 2021;June 1. doi:10.1002/pbc.28983

239. Curnis F, Sacchi A, Corti A. Improving Chemotherapeutic Drug Penetration in Tumors by Vascular Targeting and Barrier Alteration. *J Clin Invest*. 2002;110(4):475-482. doi:10.1172/jci15223

240. Teh S-Y, Lin R, Hung L-H, Lee AP. Droplet Microfluidics. *Lab Chip*. 2008;8(2):198. doi:10.1039/b715524g

241. Lin W, Wang Y, Wang S, Tseng H. Integrated Microfluidic Reactors. *Nano Today*. 2009;4(6):470-481. doi:10.1016/j.nantod.2009.10.007

242. Sadat SMA, Vakili MR, Paiva IM, Weinfeld M, Lavasanifar A. Development of self-associating sn-38-conjugated poly(Ethylene oxide)-poly(ester) micelles for colorectal cancer therapy. *Pharmaceutics*. 2020;12(11):1-22. doi:10.3390/pharmaceutics12111033

7 Appendix 1: Supplementary Information for Chapter 2

Supporting Information. Critical water content determination of copolymer; complete cytotoxicity data; table of actual flow rates.

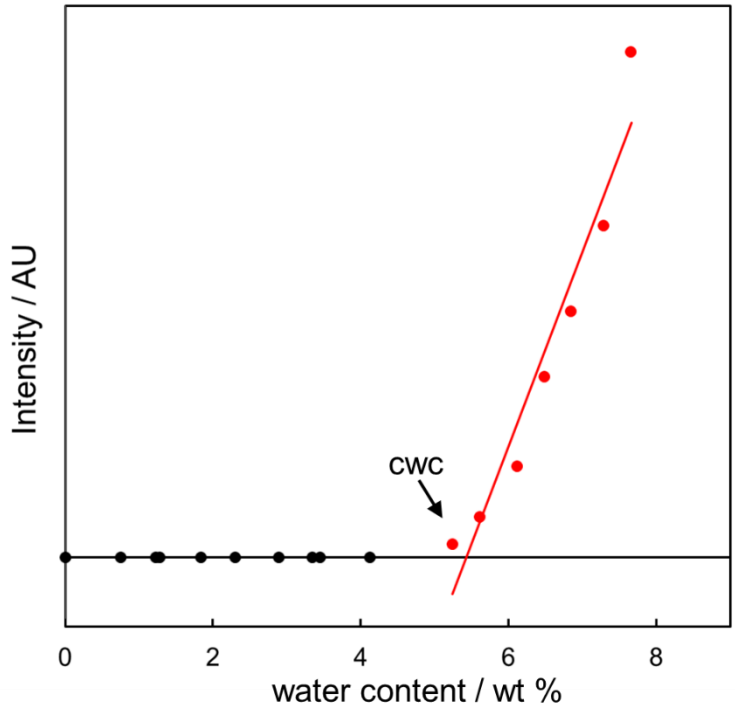

Figure 38: Sample light scattering titration curve for cwc determination of PCL-b-PEO (0.33 wt % in DMF)

Reproduced with permission.

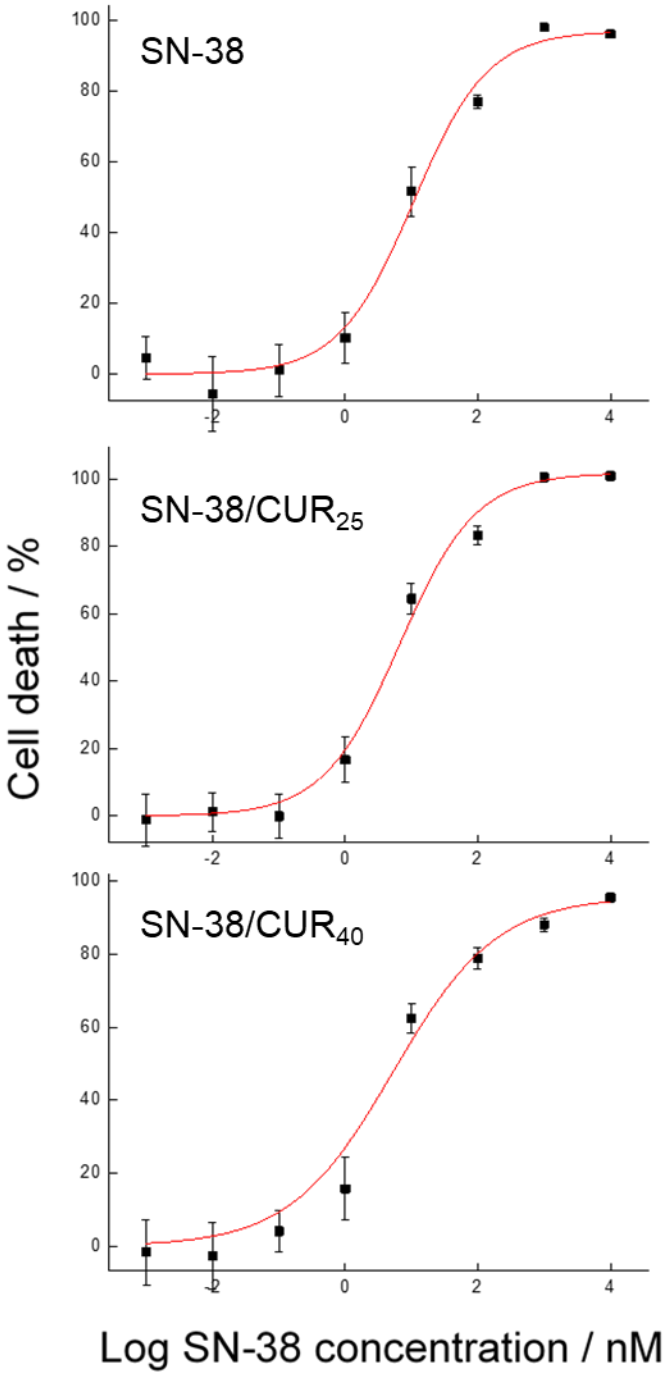

Figure 39: 72-h cell death plots including raw data and fits for free SN-38 and SN-38/CUR blends in A204 cells

Used to determine IC_{50} values for Figure 14 . Reproduced with permission.

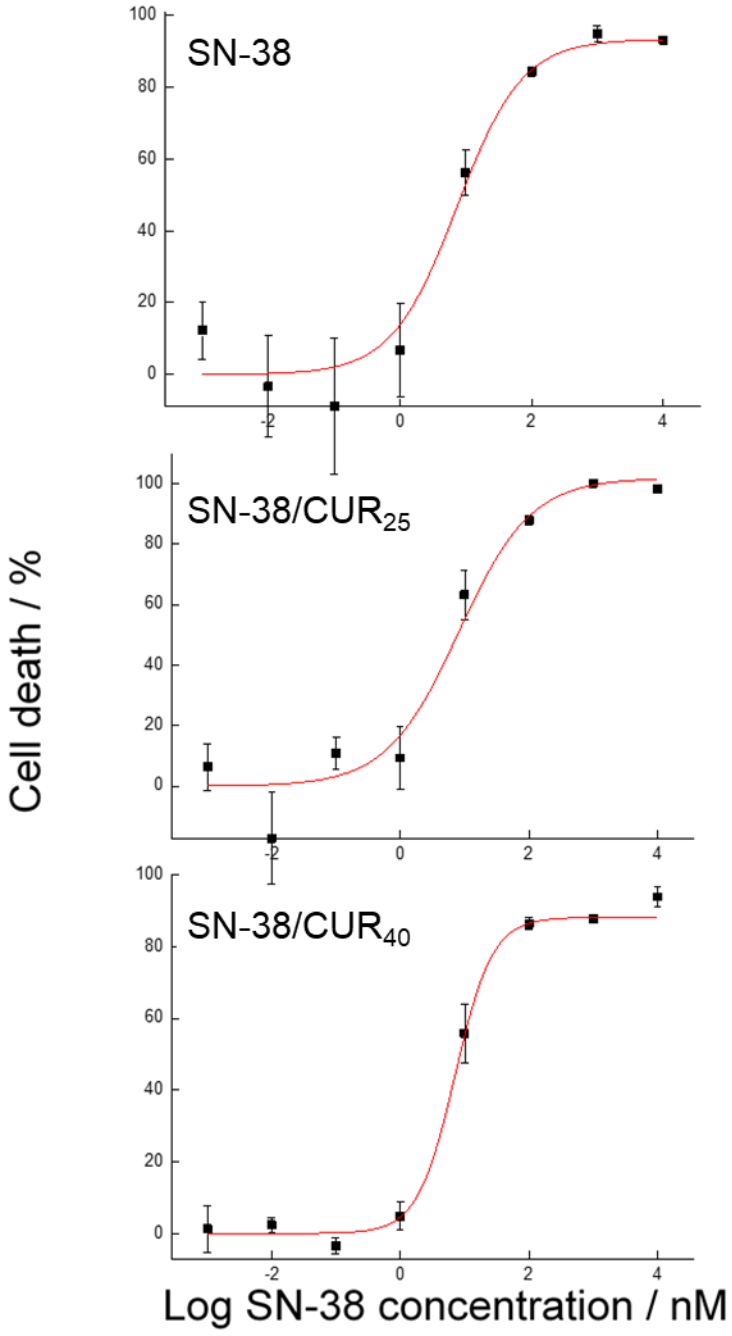

Figure 40: 96-h cell death plots including raw data and fits for free SN-38 and SN-38/CUR blends in A204 cells

Used to determine IC_{50} values for Figure 14. Reproduced with permission.

.

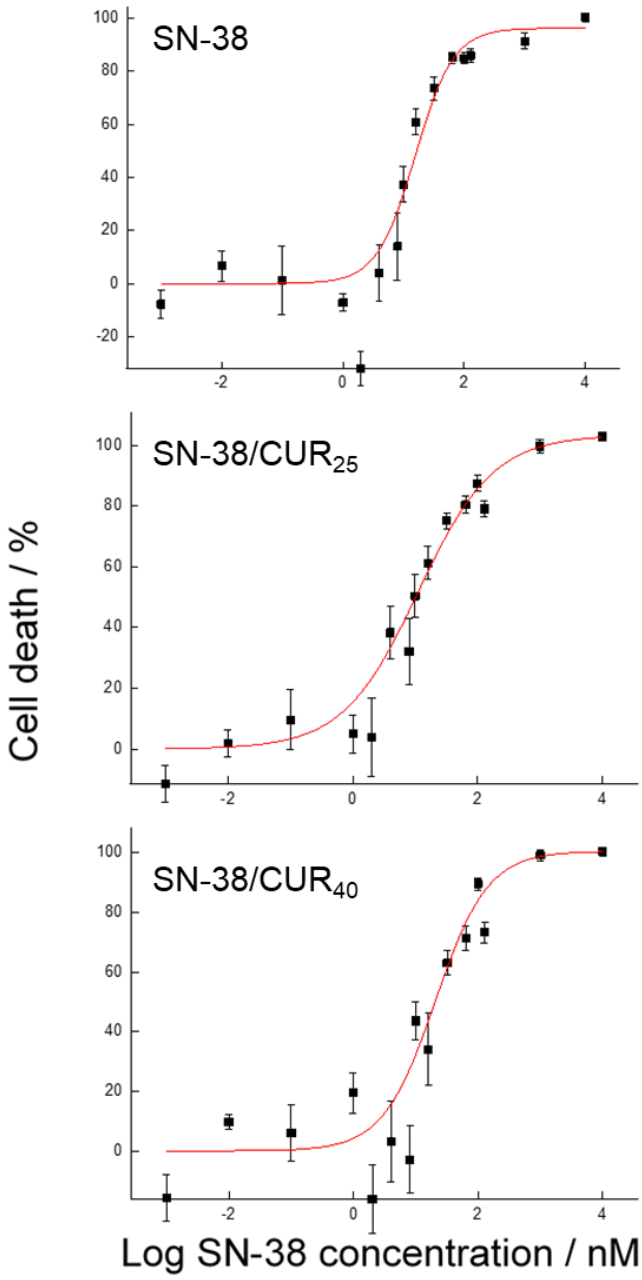

Figure 41: 72-h cell death plots including raw data and fits for free SN-38 and SN-38/CUR blends in U87 cells

Used to determine IC_{50} values for Figure 14. Reproduced with permission.

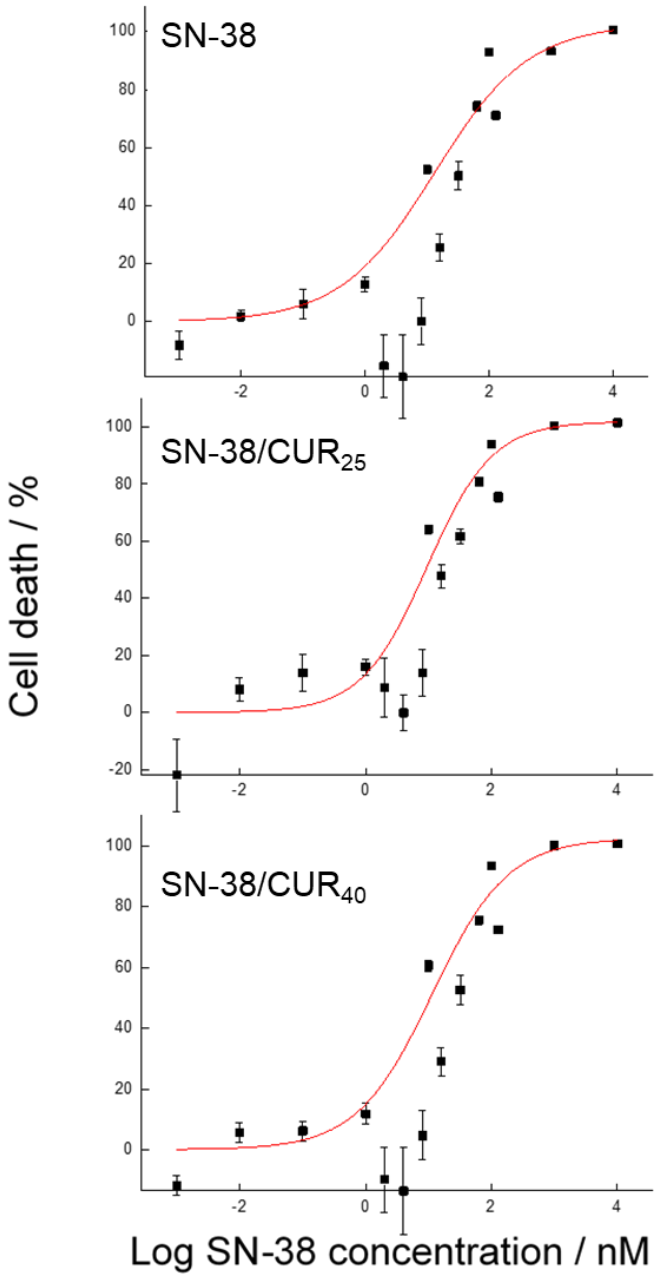

Figure 42: 96-h cell death plots including raw data and fits for free SN-38 and SN-38/CUR blends in U87 cells

Used to determine IC_{50} values for Figure 14. Reproduced with permission.

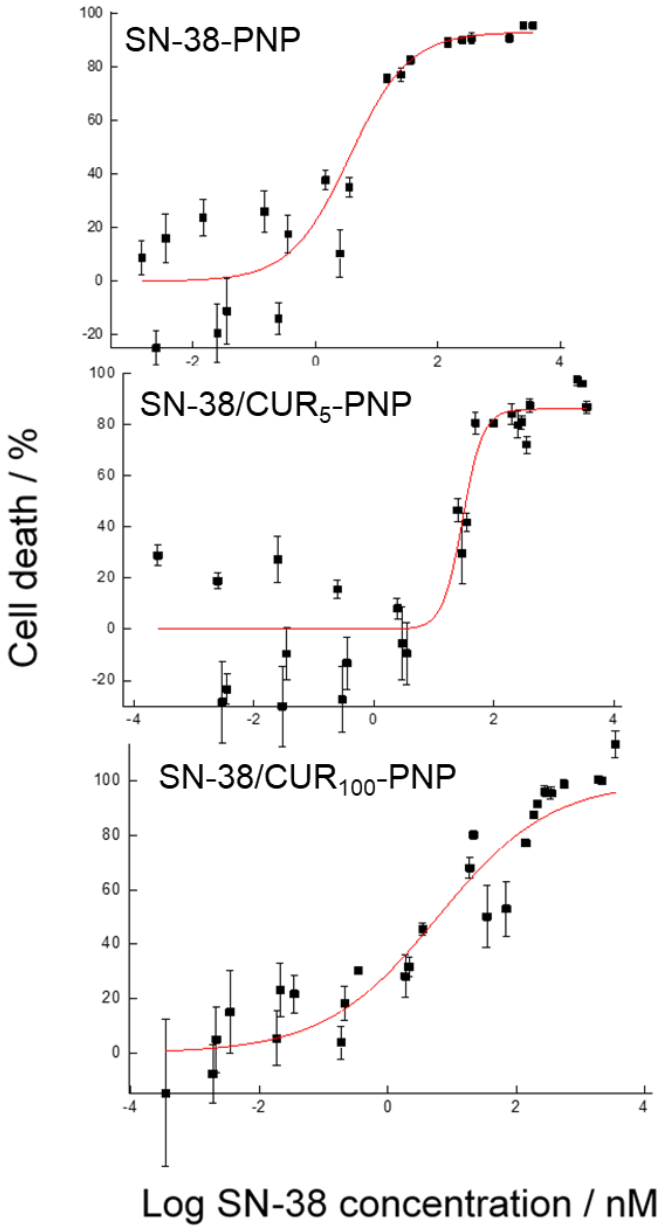

Figure 43: 72-h cell death plots including raw data and fits for PNP formulations described in Table 1 in A204 cells

Used to determine IC_{50} values for Figure 15. Reproduced with permission.

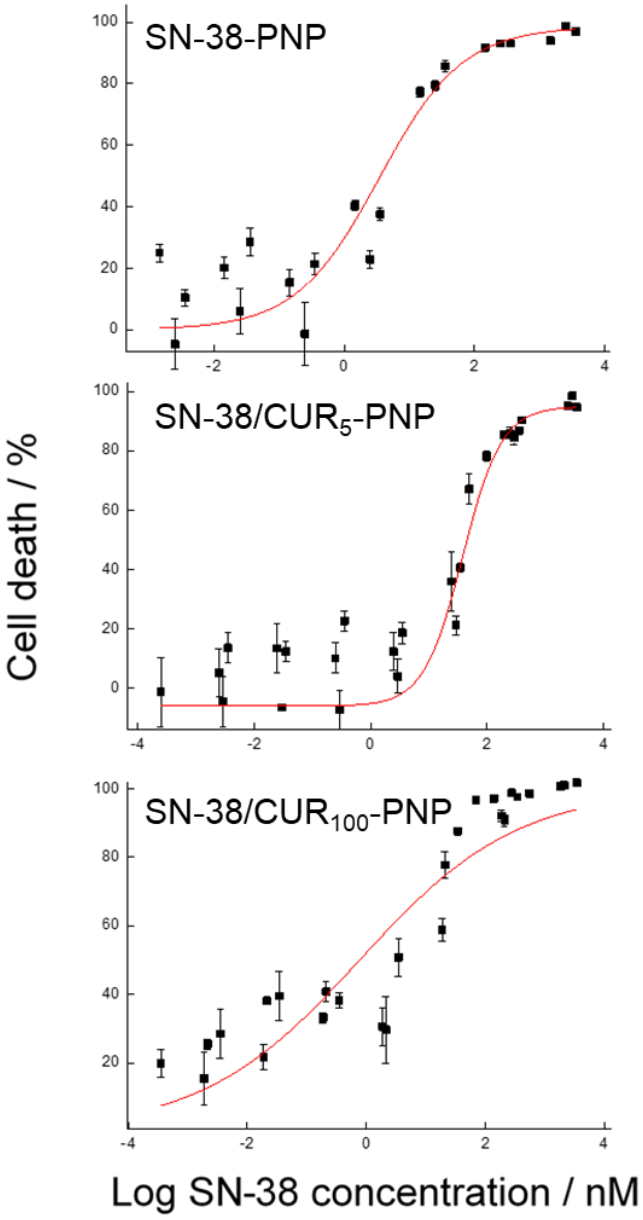

Figure 44: 96-h cell death plots including raw data and fits for PNP formulations described in Table 1 in A204 cells

Used to determine IC_{50} values for Figure 15. Reproduced with permission.

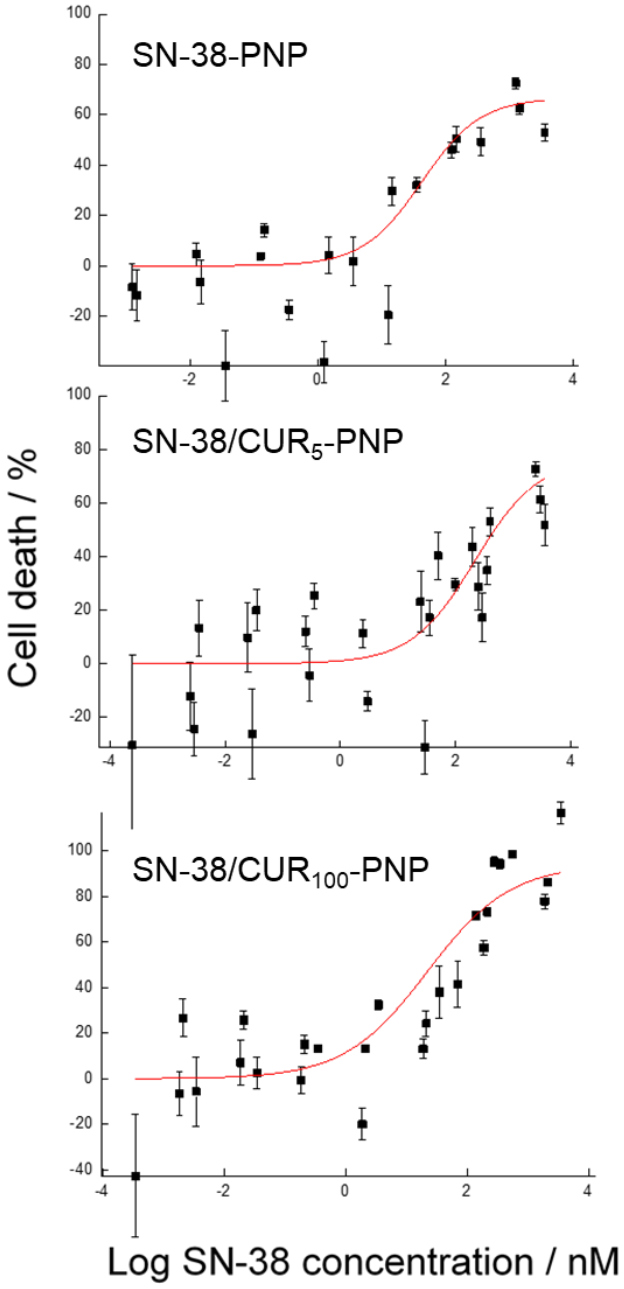

Figure 45:72-h cell death plots including raw data and fits for PNP formulations described in Table 1 in U87 cells

Used to determine IC_{50} values for Figure 15. Reproduced with permission.

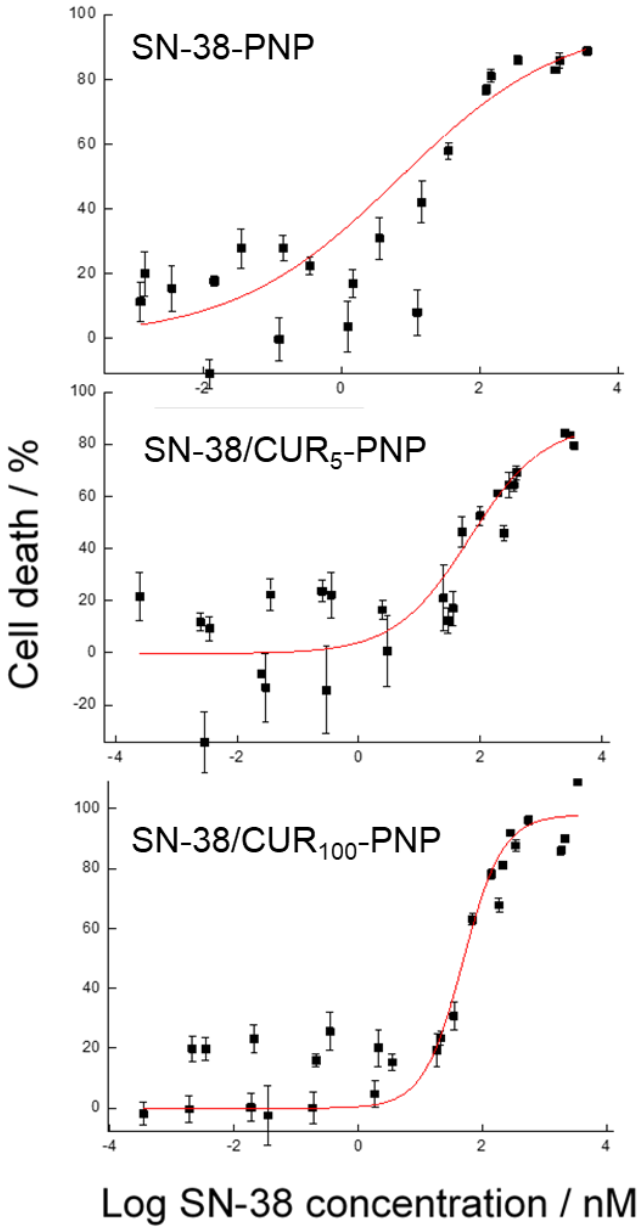

Figure 46: 96-h cell death plots including raw data and fits for PNP formulations described in Table 1 in U87 cells

Used to determine IC_{50} values for Figure 15. Reproduced with permission.

Table 2: Actual Flow Rates of Triplicate Microfluidic Preparations under Various Conditions

Actual Flow Rates of Triplicate Microfluidic Preparations under Various Conditions. Reproduced with permission.

r_{SN-38}	r_{CUR}	Nominal flow rate / µL min^{-1}	Actual flow rate #1 / µL min^{-1}	Actual flow rate #2 / µL min^{-1}	Actual flow rate #3 / µL min^{-1}
0.1	0	200	207	211	196
0.1	0.1	200	201	188	193
0.1	0.5	200	195	188	212
0.1	0.75	200	199	190	212
0.1	1	200	190	196	180
0.1	10	200	209	188	217
0.25	0.5	200	195	180	157
0.5	0.5	200	174	157	175
0.75	0.5	200	176	194	158
0.1	0.5	50	54	51	55
0.1	0.5	100	93	104	103
0.1	0.5	400	399	378	414

Table 3: EC50 values of Cytotoxicity Assays for Various Nanoparticle and Free Drug Formulations

Formulation	A204 Cells		U87 cells	
	72 h	96 h	72 h	96 h
SN-38-PNP	3.6 ± 0.8	3.5 ± 0.8	43 ± 20	7 ± 6
SN-38/CUR_5-PNP	30 ± 6	39 ± 5	217 ± 192	67 ± 18
SN-38/CUR_{100}-PNP	6 ± 2	0.8 ± 0.4	22 ± 10	49 ± 9
SN-38	11 ± 3	7 ± 2	16 ± 4	13 ± 5
SN-38/CUR_{25}	7 ± 2	8 ± 4	11 ± 2	9 ± 3
SN-38/CUR_{40}	5 ± 2	7 ± 2	21 ± 6	12 ± 6

8 Appendix 2: Table of critical water concentration

Table 4. Table of critical water concentration

PEG Terminal Endgroup	Critical Water Concentration	Standard Error
CH_2-CH_2-COO-CH_2-CH_2-SH	5.3%	0.07
NH_2	5.1%	0.5
COOH	5.3%	0.3
OCH_3	5.6%	0.1

9 Appendix 3: Actual Flow Rates for PEG Terminal End Group Experiments

Table 5. Actual flow rates for PEG Terminal End Group Experiments

PEG Terminal End Group	Flow Rate / µL min^{-1}	Actual Flow Rate #1/ µL min^{-1}	Error/ µL min^{-1}	Actual Flow Rate #1/ µL min^{-1}	Error/ µL min^{-1}	Actual Flow Rate #1/ µL min^{-1}	Error/ µL min^{-1}
R-COOH	200	181	2	180	3	185	2
R-NH_2		184	1	208	2	193	3
R-OCH_3		204	2	214	2	191	2
R-SH		188	2	207	2	187	4
R-C6		197	4	185	2	209	3

10 Appendix 4: EC50 curves for Chapter 4

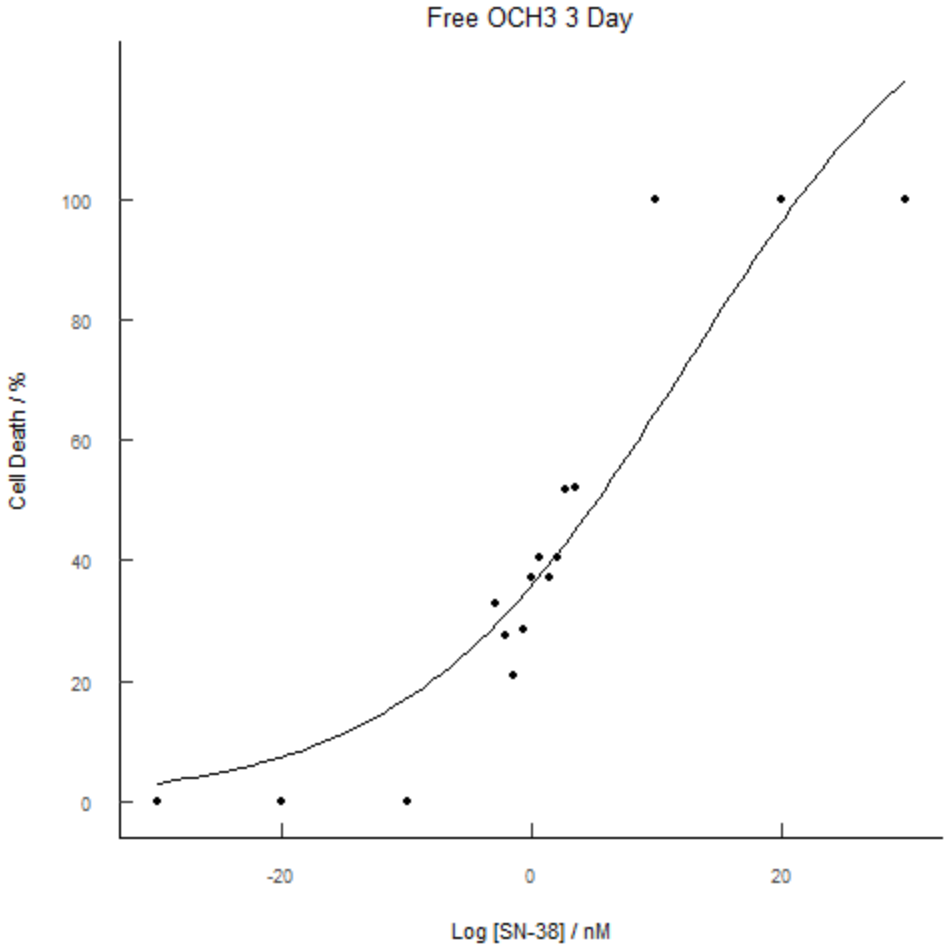

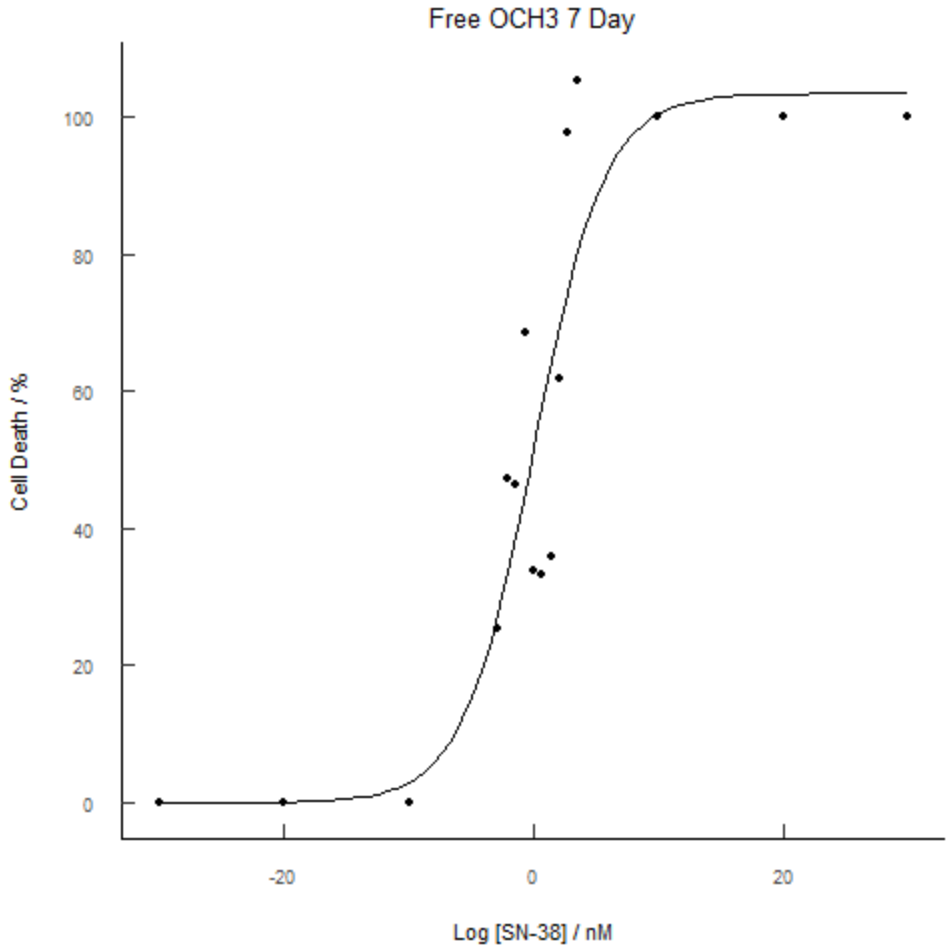
Free OCH3 7 Day
Cell Death / %
100
80
60
40
20
0
-20
0
20
Log [SN-38] / nM

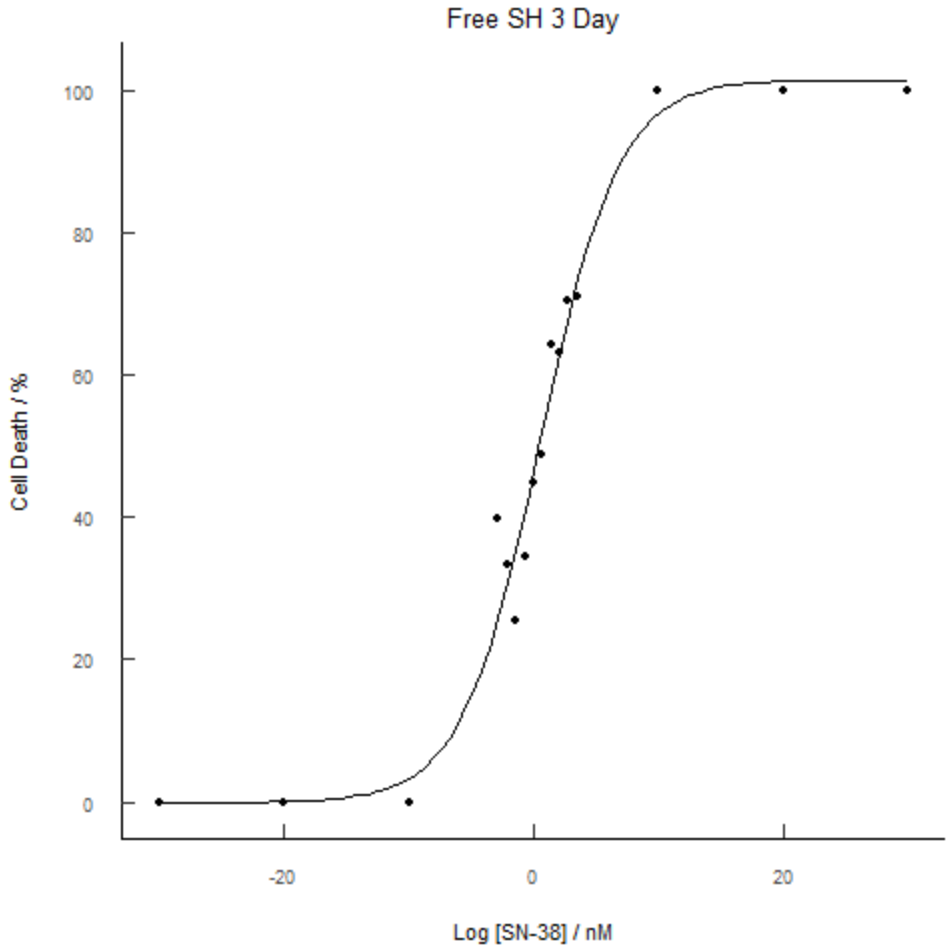
Free SH 3 Day
Cell Death / %
100
80
60
40
20
0
-20
0
20
Log [SN-38] / nM

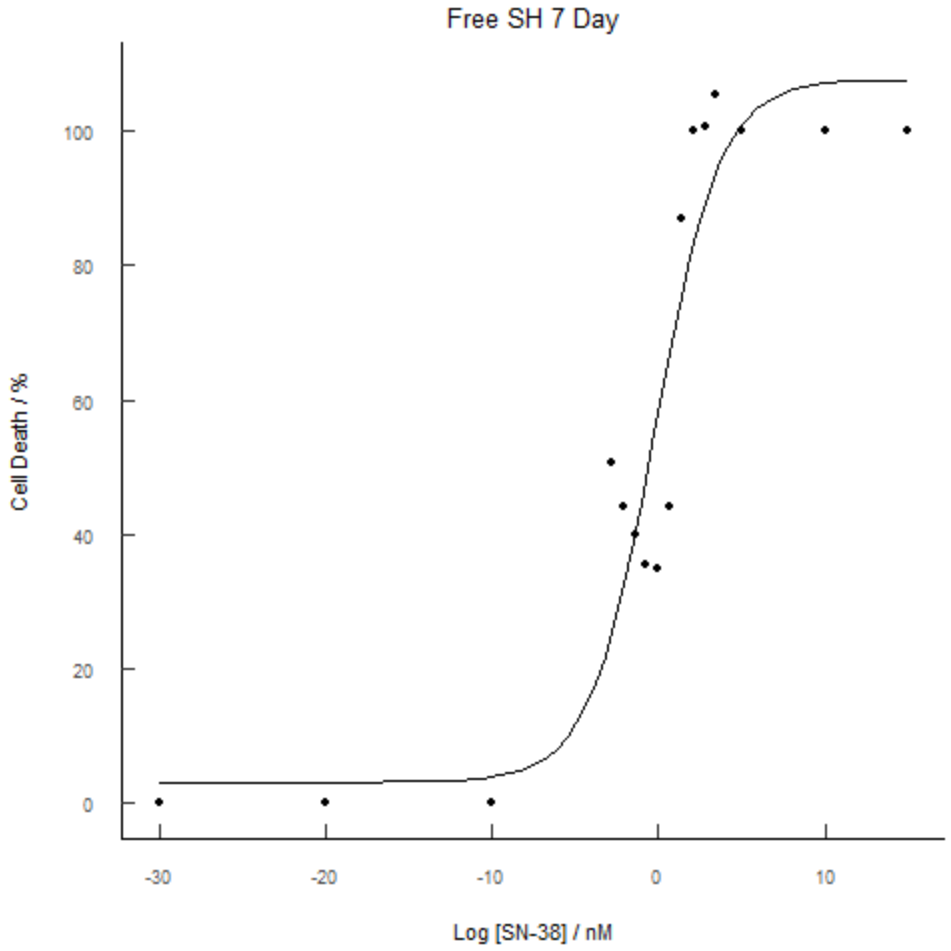
Free SH 7 Day
Cell Death / %
100
80
60
40
20
0
-30
-20
-10
0
10
Log [SN-38] / nM

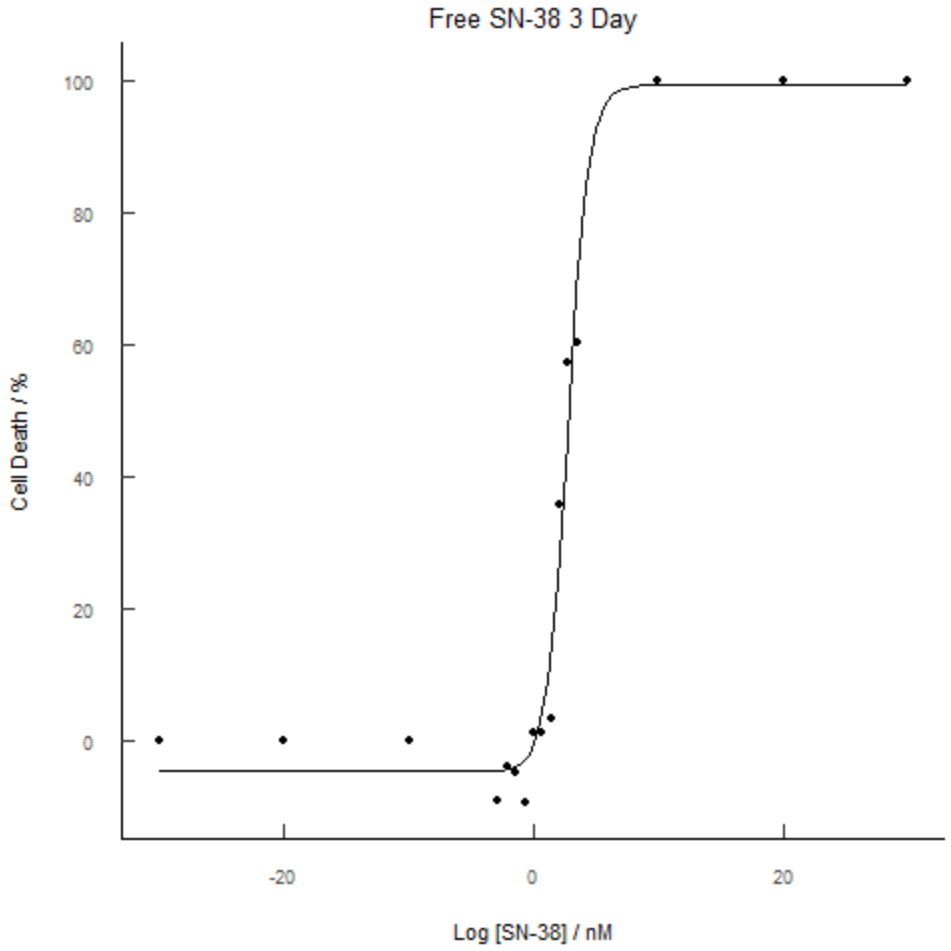
Free SN-38 3 Day
Cell Death / %
100
80
60
40
20
0
-20
0
20
Log [SN-38] / nM

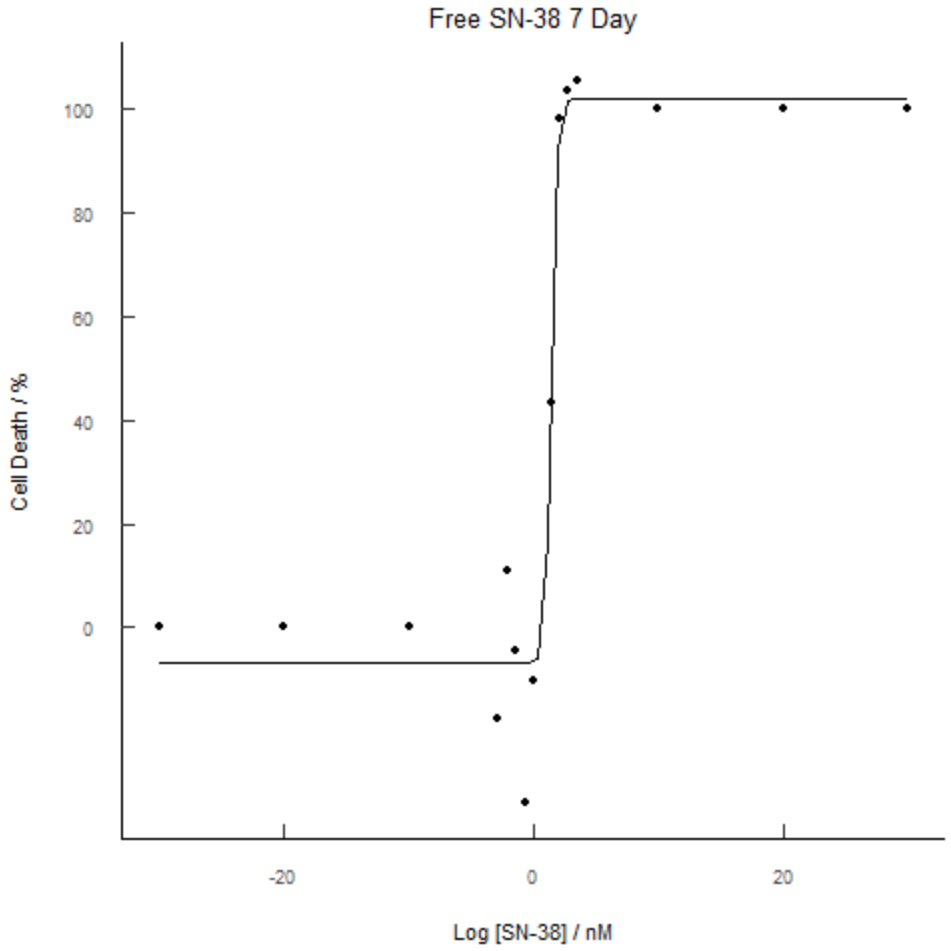
Free SN-38 7 Day
Cell Death / %
100
80
60
40
20
0
-20
0
20
Log [SN-38] / nM

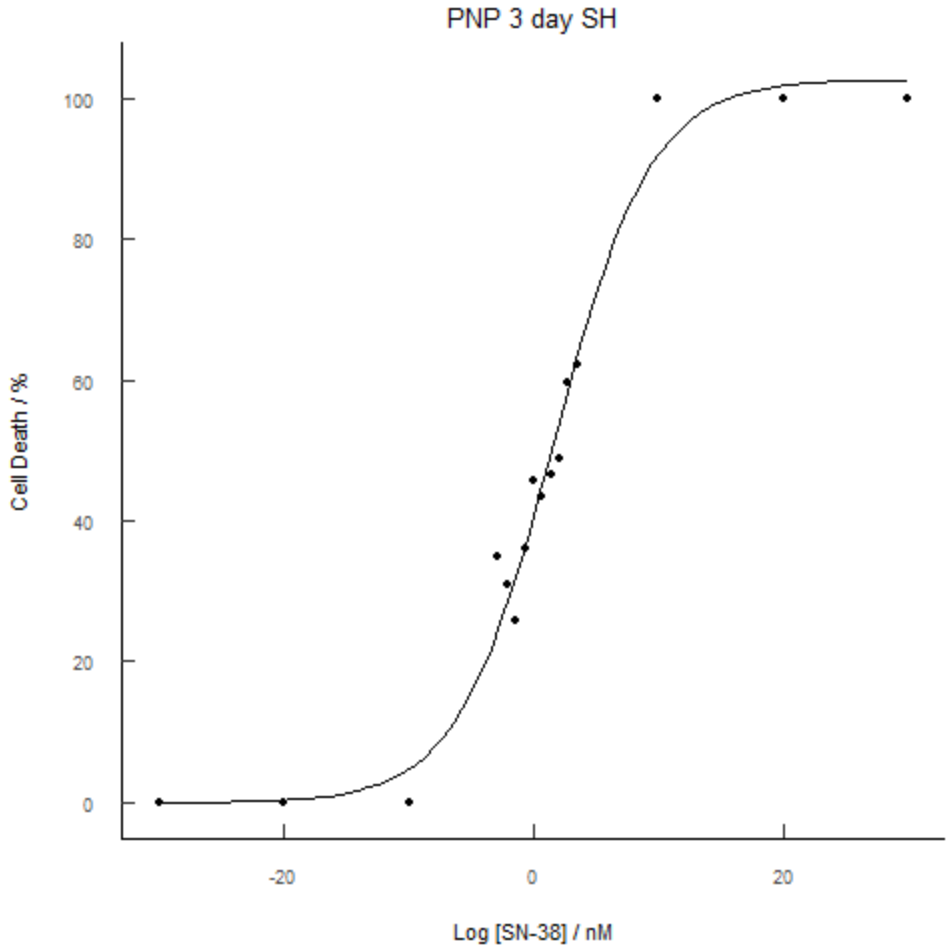
PNP 3 day SH
Cell Death / %
100
80
60
40
20
0
-20
0
20
Log [SN-38] / nM

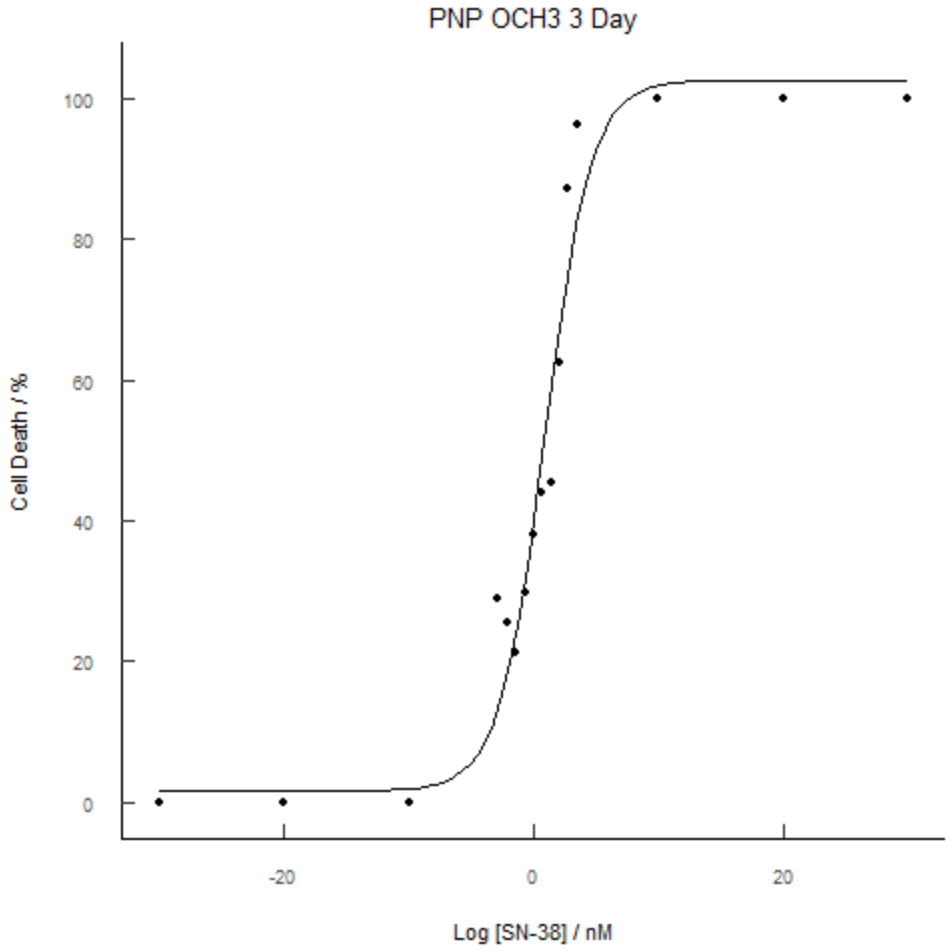
PNP OCH3 3 Day
Cell Death / %
100
80
60
40
20
0
-20
0
20
Log [SN-38] / nM

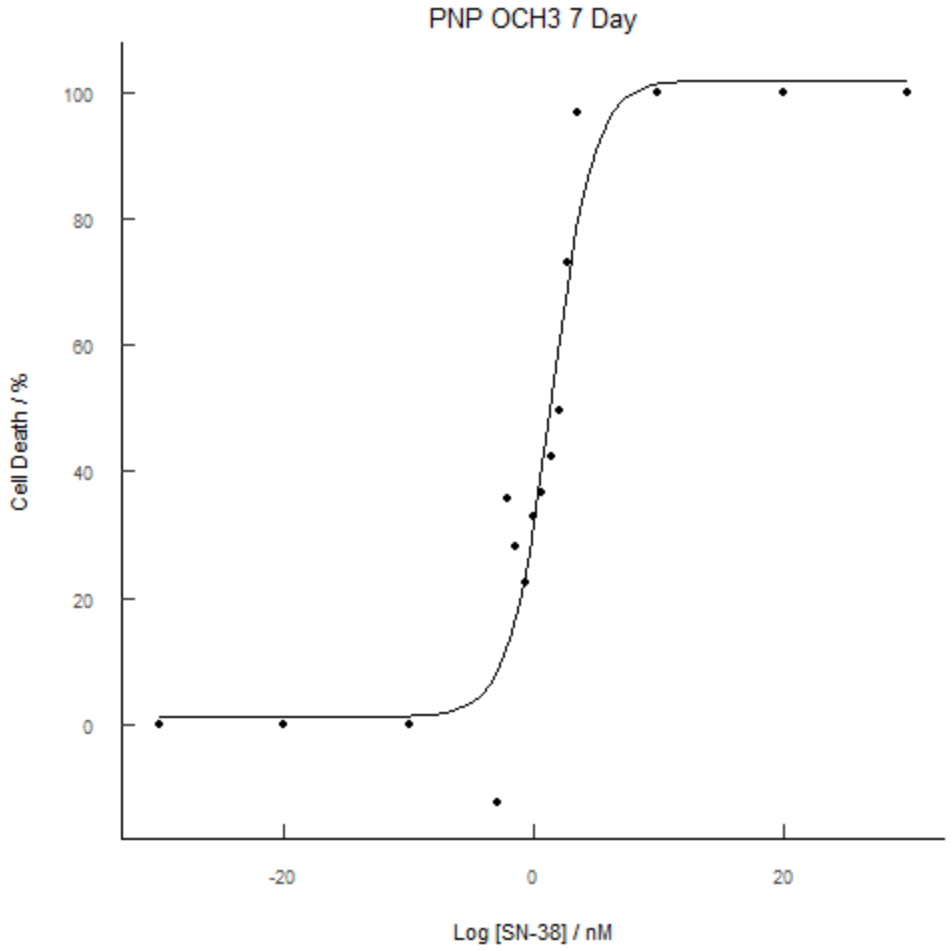
PNP OCH3 7 Day
Cell Death / %
100
80
60
40
20
0
-20
0
20
Log [SN-38] / nM

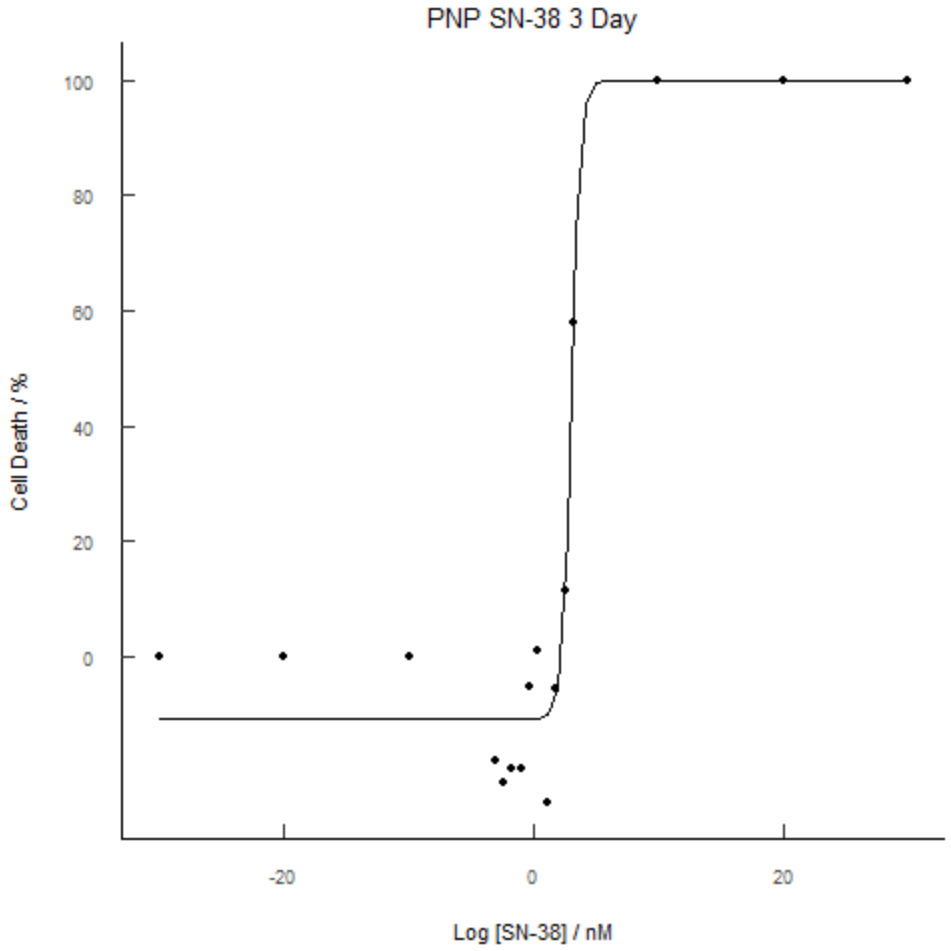
PNP SN-38 3 Day
Cell Death / %
100
80
60
40
20
0
-20
0
20
Log [SN-38] / nM

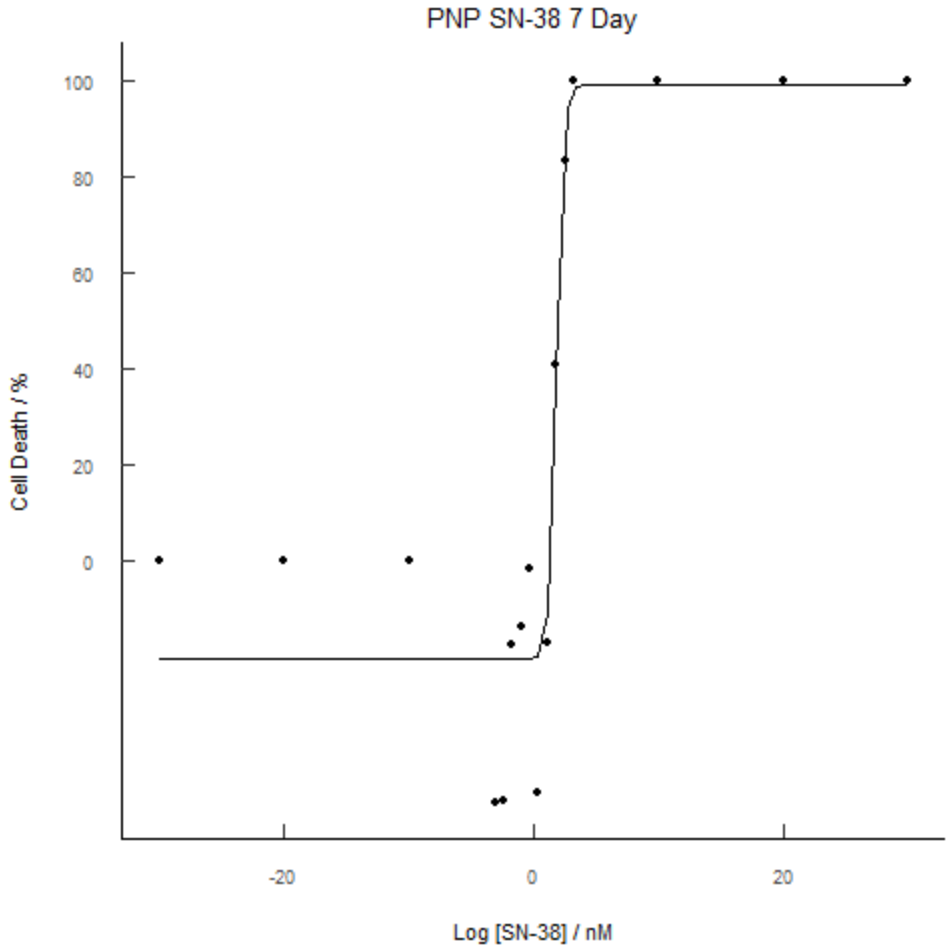
PNP SN-38 7 Day
Cell Death / %
100
80
60
40
20
0
-20
0
20
Log [SN-38] / nM

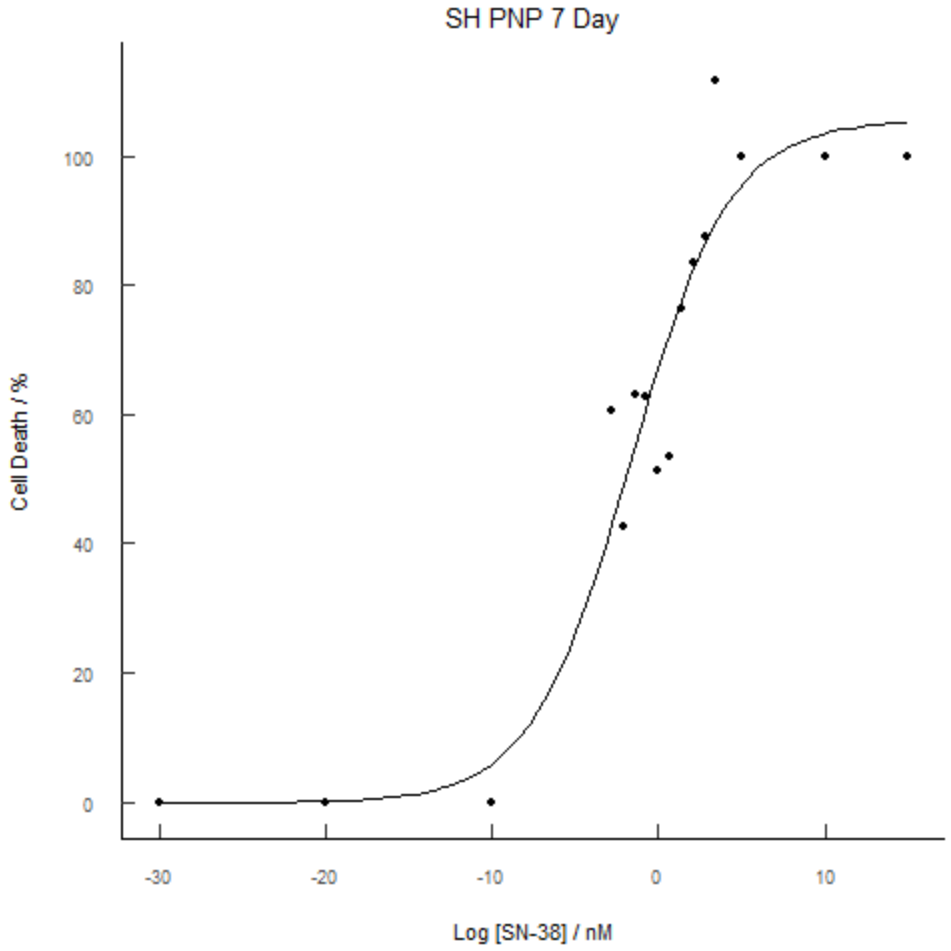
SH PNP 7 Day
Cell Death / %
100
80
60
40
20
0
-30
-20
-10
0
10
Log [SN-38] / nM